

# **Noble Metal Nanoparticles for Surface/Gas-phase Reactions**

by

**Chengcheng Rao**

A thesis submitted in partial fulfillment of the requirements for the degree of

**Doctor of Philosophy**

Department of Chemistry  
University of Alberta

© Chengcheng Rao, 2020

# Abstract

The climate crisis has rendered the utilization of clean and renewable solar energy for chemical transformations extremely important. Plasmonic nanostructures can provide tunable optical and electronic properties that can drive chemical reactions, realizing the conversion of light energy into chemical energy. The last decade has witnessed the development of a new research field emerging from the combination of plasmonics and surface chemistry. This thesis describes a straightforward method to fabricate plasmonic stamps that are harnessed to drive surface chemistry on silicon.

An introduction to the plasmonics and hydrosilylation on silicon surfaces is provided first, followed by an overview of the proposed mechanisms for plasmon-driven reactions and the recent advances of plasmon-driven reactivity for surface functionalization. Hydrosilylation triggered by metallic nanoparticles, such as Pd, Pt, and Au nanoparticles embedded in soft PDMS stamps, is reviewed in detail.

The plasmonic stamps were prepared by sputtering gold films on flexible PDMS, followed by thermal annealing to dewet the gold to form gold nanoparticles. By changing the film thickness of the sputtered gold, the approximate size and shape of these gold nanoparticles can be changed, leading to a shift in the optical absorbance maximum of the plasmonic stamp from 535 to 625 nm. By applying the plasmonic stamp to a Si(111)-H surface using a long-chain alkene as the ink, illumination with green light results in covalent attachment of linear alkyl groups to the surface. Of the dewetted gold films on PDMS used to make the plasmonic stamps, the thinnest three

(5.0, 7.0, and 9.2 nm) resulted in the most effective plasmonic stamps for hydrosilylation. Because the electric field generated by the LSPR would be very local, hydrosilylation on the silicon surface should take place within only close proximity of the gold particles on the plasmonic stamps. These results underline the central role played by the LSPR in driving the hydrosilylation on silicon surfaces, mediated with plasmonic stamps. By using these highly reproducible PDMS stamps, studies of the reaction kinetics for plasmon-induced hydrosilylation on silicon substrates were carried out. Through variation of the doping levels, critical insights were gleaned, and a relationship between reaction rates and built-in electrical fields of metal-insulator-semiconductor junctions was determined, along with a set of physical models and corresponding formulae. This work provides important insights into the reactivity of plasmonic structures in close proximity to a semiconductor, which is a common and important architecture used as a platform for photochemistry, light-promoted catalysis, and photonics in general. We reveal the intricate interplay between the electronics of the semiconductor proximal to the electric field induced by the localized surface plasmons, and how the resulting charge carriers can be used to drive chemical reactivity.

Additionally, results from a secondary project are reported in Chapter 4. Pd-Pt/ZrO<sub>2</sub> catalysts with three different nanostructures were designed, synthesized, and their catalytic performance and lifetimes were evaluated for wet methane combustion, which pointed to advantages and limitations of yolk-shell nanostructures. Finally, the thesis concludes with a summary of each chapter and directions for future studies.

# Preface

This thesis is composed of five chapters. Chapter 1 introduces plasmonics and hydrosilylation, with an emphasis on plasmon-driven hydrosilylation by PDMS stamps. Chapter 2 introduces the facile fabrication of plasmonic stamps by gold dewetting on PDMS and demonstrates the efficacy of this approach. Chapter 3 presents a mechanistic understanding of plasmon-driven hydrosilylation through kinetic studies on silicon wafers of variable doping levels. Chapter 4 examines the catalytic performance of three Pd-Pt/ZrO<sub>2</sub> catalysts for wet methane combustion by designing different nanostructures. Finally, Chapter 5 summarizes the thesis and provides several research directions for future work.

The work described in Chapter 2 has been published as: “Rao, C.; Lubner, E. J.; Olsen, B. C.; Buriak, J. M. Plasmonic Stamps Fabricated by Gold Dewetting on PDMS for Catalyzing Hydrosilylation on Silicon Surfaces. *ACS Appl. Nano Mater.*, **2019**, 2, 3238–3245. I designed the initial experimental plan with Dr. Erik J. Lubner, Brian C. Olsen, and Prof. Jillian M. Buriak, and conducted all the experiments, analyzed the data, prepared the figures, and wrote the initial manuscript. Tate C. Hauger designed the sample holder. My supervisor, Prof. Jillian M. Buriak, assisted with manuscript writing. All authors have given approval to the final version of the manuscript.

Chapter 3 is written as an article. Like most of the research in our group, it is the product of a collaborative effort. I designed the research plan with Dr. Erik J. Lubner, Brian C. Olsen, and Prof. Jillian M. Buriak, and I carried out the experiments, and analyzed the data, which took place both pre- and post-pandemic shutdown. Dr. Erik J.

Luber, interpreted the experimental results, derived the formulae, and further honed the mechanism explanation. Prof. Jillian M. Buriak assisted with writing the article.

The work in Chapter 4 is part of an NSERC Strategic Partnership Grant, collaborating with the group of Prof. Natalia Semagina in the Department of Chemical and Material Engineering. Prof. Natalia Semagina proposed the initial ideas, and I performed the experiments, analyzed the data, and wrote the reports. Dr. Jing Shen performed the methane combustion catalysis tests. Prof. Jillian M. Buriak, my supervisor, coordinated the collaboration and assisted in writing the reports.

# Acknowledgments

I would like to express my deep appreciation to everyone who helped me during my Ph.D. studies. First and foremost, I would like to express my sincere gratitude to my supervisor, Dr. Jillian M. Buriak, for her continuous encouragement, enthusiasm and mentorship, allowing me to grow up as a scientist. Her passion and knowledge for science have helped me to overcome the challenges in my research over the past five years. I am also grateful for her support for various conferences and collaborations, where I met many great researchers all over the world and widened my horizons.

I would like to thank my supervisory committee members, Dr. Jed Harrison, Dr. Michael J. Serpe, and Dr. Julianne M. Gibbs, for their valuable advice and support during my studies. Thanks to my examination committee members, Dr. Hongbo Zeng and Dr. Hyun-Joong Chung, for their thoughtful examination and suggestions. In addition, I am grateful to Dr. Mita Dasog from Dalhousie University for agreeing to be the external examiner for my Ph.D. defense. Thanks to Dr. Robert Jordan for chairing my exams.

My deep thanks to the team members in the Buriak research group for providing such a cooperative and fun atmosphere, useful suggestions, and discussions on my research projects. Special thanks to Dr. Fenglin Liu for his pioneer work and tireless support. I would like to thank Dr. Erik Lubber and Brian Olsen for their guidance and inspiration in my research, as well as Tate Hauger for sharing his versatile technical skills with me and his kind help. Thanks to Dr. Bing Cao, Dr. Cong Jin, Dr. Chris Fetterly, Dr. Minjia Hu, Dr. Hezhen Xie, Dr. Dan Yang, and Mahmoud Almadhoun for

their encouragement and sharing of their experience. Thanks to Dr. Peter Kalisvaart, Dr. Sayed Youssef Sayed, Kelli Luber, Jennifer Ozdoba, Dr. Binbin Yu, Dr. Youngdong Song, Hao Wang, Gayashani Ginige, Jasper Woodard, Aaron Kirkey, Adrian Velazquez Osorio and Miriam Fenniri for their assistance and inspiration.

Thanks to my collaborators, Dr. Natalia Semagina, and Dr. Jing Shen from the Department of Chemical and Materials Engineering, for their support and sharing of their expertise. I am also grateful to the staff in the Department of Chemistry, NRC-NINT, the nanoFAB, and the Alberta Cross Cancer Institute for their support for my studies and research. Thank you, Anita Weiler, Paul Concepcion, Dr. Anqiang He, Dr. Shihong Xu, Dr. Nancy Zhang, Aditi Ganji, Peng Li, Dr. Xuejun Sun, and Pinzhang Gao. A very big thank you to Dr. Anna Jordan for excellent thesis editing with delightful insight into my work.

And of course, thank you to all my family members for their unconditional love and endless support. Without you, I would never have made it this far.

# Table of Contents

<b>Abstract.....</b>	<b>ii</b>
<b>Preface.....</b>	<b>iv</b>
<b>Acknowledgments .....</b>	<b>vi</b>
<b>Table of Contents .....</b>	<b>viii</b>
<b>List of Tables .....</b>	<b>xi</b>
<b>List of Figures.....</b>	<b>xii</b>
<b>List of Abbreviations .....</b>	<b>xxv</b>
<b>Chapter 1 Introduction.....</b>	<b>1</b>
<b>1.1 Overview .....</b>	<b>1</b>
<b>1.2 Plasmonics .....</b>	<b>2</b>
1.2.1 Overview of Plasmons .....	2
1.2.2 Plasmonic Metal Nanostructures .....	3
<b>1.3 Plasmon-driven Reactions.....</b>	<b>6</b>
1.3.1 Plasmon Field-driven Catalysis .....	7
1.3.2 Hot Carrier-driven Catalysis .....	8
1.3.3 Plasmonic Thermal Catalysis.....	9
<b>1.4 Plasmon-driven Catalysis for Functionalization of Surfaces.....</b>	<b>10</b>
1.4.1 Overview.....	10
1.4.2 Plasmon-driven Surface Grafting of Molecules .....	11
1.4.3 Plasmon-driven Surface Polymerization.....	12
1.4.4 Plasmon-driven Surface Chemistry for Site-selective Grafting of Nanoparticles .....	13
<b>1.5 Hydrosilylation on Si Surfaces.....</b>	<b>15</b>
1.5.1 Overview.....	15
1.5.2 Pd/Pt Catalyzed Hydrosilylation on Si Surface .....	16
1.5.3 Au Plasmon-induced Hydrosilylation on Si surface .....	19
<b>1.6 Scope of the Thesis .....</b>	<b>21</b>

<b>Chapter 2 Fabricating Plasmonic Stamps by Gold Dewetting for Catalyzing Hydrosilylation on Silicon Surfaces .....</b>	<b>23</b>
<b>2.1 Introduction.....</b>	<b>23</b>
<b>2.2 Results and Discussion.....</b>	<b>25</b>
<b>2.3 Conclusions.....</b>	<b>38</b>
<b>2.4 Experimental Section.....</b>	<b>38</b>
2.4.1 Materials .....	38
2.4.2 Characterization .....	39
2.4.3 Blank PDMS Stamp Preparation .....	40
2.4.4 Preparation of Plasmonic Stamps .....	40
2.4.5 Silicon Wafer Cleaning and Preparation.....	41
2.4.6 Plasmonic Stamping on Hydride-Terminated Silicon Surfaces.....	41
2.4.7 Gold Deposition on Silicon via Galvanic Displacement .....	42
<b>Chapter 3 Mechanistic Investigation of Plasmon-induced Hydrosilylation on Si Surfaces by Kinetic Studies.....</b>	<b>43</b>
<b>3.1 Introduction.....</b>	<b>43</b>
<b>3.2 Kinetic Studies of Plasmon-induced Hydrosilylation on Si Surfaces.....</b>	<b>47</b>
<b>3.3 Mechanistic Understanding of Plasmon-induced Hydrosilylation on Si Surfaces.....</b>	<b>54</b>
3.3.1 Reaction Rate Calculations .....	54
3.3.2 Mechanistic Discussion .....	56
<b>3.4 Conclusions.....</b>	<b>62</b>
<b>3.5 Experimental Section.....</b>	<b>63</b>
3.5.1 Materials .....	63
3.5.2 Characterization .....	64
3.5.3 Blank PDMS Stamp Preparation .....	64
3.5.4 Silicon Wafer Cleaning and Preparation.....	65
3.5.5 Gold Dewetting on Si wafers or PDMS.....	65
3.5.6 Plasmonic Stamping on Hydride-Terminated Silicon Surfaces.....	65
<b>Chapter 4 Pd-Pt@void@ZrO<sub>2</sub> Yolk-Shell Nanoparticles for Wet Methane Combustion.....</b>	<b>67</b>

<b>4.1 Introduction.....</b>	<b>67</b>
<b>4.2 Results and Discussion.....</b>	<b>73</b>
4.2.1 Synthesis of Pd-Pt@void@ZrO <sub>2</sub> Yolk-Shell Nanoparticles.....	73
4.2.2 Testing of Pd-Pt on ZrO <sub>2</sub> for Wet Methane Combustion .....	79
<b>4.3 Conclusions.....</b>	<b>89</b>
<b>4.4 Experimental Section.....</b>	<b>89</b>
4.4.1 Materials .....	89
4.4.2 Characterization .....	90
4.4.3 Synthesis of Pd-Pt Bimetallic Nanoparticles .....	90
4.4.4 Synthesis of Pd-Pt@SiO <sub>2</sub> Nanoparticles.....	91
4.4.5 Synthesis of Pd-Pt@void@ZrO <sub>2</sub> Nanoparticles .....	91
4.4.6 Synthesis of Pd-Pt@ZrO <sub>2</sub> Catalyst .....	91
4.4.7 Synthesis of Pd-Pt/ZrO <sub>2</sub> Impregnated Catalyst.....	92
4.4.8 Test for Wet Methane Combustion.....	92
<b>Chapter 5 Thesis Summary and Outlook.....</b>	<b>94</b>
<b>5.1 Summary.....</b>	<b>94</b>
5.1.1 Chapter 1 .....	94
5.1.2 Chapter 2.....	94
5.1.3 Chapter 3.....	95
5.1.4 Chapter 4.....	95
<b>5.2 Future Works .....</b>	<b>96</b>
5.2.1 Expanding the Menu for Metal Dewetting on PDMS .....	96
5.2.2 Variation of Shapes for Plasmonic Nanoparticles on PDMS .....	98
5.2.3 Synthesis Pd-Pt@SiO <sub>2</sub> Nanoparticles via Magnesiothermic Reduction..	100
<b>References.....</b>	<b>102</b>

## List of Tables

Table 1.1 Summary of the Shapes, LSPR Absorption Peaks for Silver Nanoparticles. Reproduced with Permission From Reference 19. Copyright 2011 American Chemical Society.....	5
Table 2.1 Deposition Parameters and Optical characteristics of Sputter-deposited Au films on PDMS. ....	28
Table 2.2 Summary of Static Water Contact Angle. ....	33
Table 3.1 Resistivity, Rate Constants for Plasmon-induced Hydrosilylation for Five Kinds of Silicon Wafers.....	56
Table 3.2 Important Parameters of Schottky Junction Between Au and Silicon of Various Doping Types and Levels. Nd: doping density; EF: Fermi level; Vbi: built-in electrical field; W: depletion width; $1/\alpha_{526}$ : illumination length.....	58
Table 4.1 Pd, Pt Contents, Pd/Pt Molar Ratio, Size of Pd-Pt Nanoparticles, BET Surface Area and BJH Pore Size from Three As-prepared Catalysts. ....	81
Table 4.2 SiO <sub>2</sub> , ZrO <sub>2</sub> Contents of Yolk-shell Nanoparticles for Different NaOH Etching Times.....	87

# List of Figures

Figure 1.1 (a) Schematic of a simple system containing a plasmonic antenna coupled through localized near-field enhancements to a catalytic reactor metal nanoparticle for organic molecular transformations. (b) Schematic of the reaction system for Au NP-photocatalyzed CO<sub>2</sub> conversion to hydrocarbons under plasmonic excitation. (c) Simplified representation of plasmon-mediated electrocatalysis to convert feedstocks into fuels. (d) Schematic illustration of the metal photo-staining method, wherein photogenerated carriers drive the deposition of Pt on semiconductor nanostructures in the presence of a plasmonic antenna. Reproduced with permission from reference 6, 7, 8. Copyright 2018 American Chemical Society. .... 1

Figure 1.2 Schematic illustration of two forms of surface plasmons excited by the electric field ( $E_0$ ) of incident light with wavevector ( $k$ ). (a) The metal/dielectric interface has one dimension much larger than the wavelength of light. In this case, a propagating surface plasmon can travel along the surface of the metal. (b) The nanosphere is smaller than the wavelength of light, and the free electrons can be displaced from the lattice of positive ions and oscillate collectively in resonance with the light. This process is named localized surface plasmon resonance (LSPR). Reproduced with permission from reference 19. Copyright 2011 American Chemical Society..... 3

Figure 1.3 Gold colloid microscope slide that Faraday used in his lecture to illustrate his work on gold colloids in 1857; it is stored in the Whipple Museum of the history of science, University of Cambridge. The inscription is “Faraday’s gold given to me himself after his lecture at the RI”. Reproduced with permission from reference 17. Copyright 2011 American Chemical Society. .... 4

Figure 1.4 Overview of surface plasmon properties of plasmonic metal nanoparticles. SPR peaks vary with different types of composition (a), shapes (b), and sizes (c). The intensity of the solar radiation curve (black) also is shown in (a). Reproduced with permission from reference 24. Copyright 2015 Nature Publishing Group. .... 6

Figure 1.5 Sketches of the photoexcitation and subsequent relaxation processes of the LSPR. Reproduced with permission from reference 36. Copyright 2019 American Chemical Society. ....	7
Figure 1.6 (a) TEM image of the cross-section of a TiO <sub>2</sub> film on Ag@SiO <sub>2</sub> core-shell on a SiO <sub>2</sub> substrate, (b) optical absorption spectra of TiO <sub>2</sub> thin film (black), Ag nanoparticles embedded in TiO <sub>2</sub> (orange), and Ag nanoparticles covered with SiO <sub>2</sub> layer embedded in TiO <sub>2</sub> (blue), and (c) decomposition rates of methylene blue (MB) on TiO <sub>2</sub> surfaces under near-UV irradiation. Reproduced with permission from reference 40. Copyright 2008 American Chemical Society. ....	8
Figure 1.7 Hot electron driven chemical reactions of 4-nitrobenzenethiol revealed by HV-TERS. Reproduced with permission from reference 41. Copyright 2012 Nature Publishing Group. ....	9
Figure 1.8 Catalytic ammonia decomposition. (a) Schematic of the structure consisting of a Cu nanoparticle antenna with a Cu-Ru surface alloy, where the Ru provides the reactor sites. This catalyst was used to quantify the contributions of hot carriers and the photothermal effect. (b) H <sub>2</sub> formation rate in photo- and thermally catalyzed reactions. Reproduced with permission from reference 1. Copyright 2018 American Association for the Advancement of Science. ....	10
Figure 1.9 (a) SEM image of Au triangles after 4 min of irradiation with visible light in the presence of bithienylbenzene diazonium salt aqueous solution. (b) Polarization-dependent plasmon-induced grafting from the diazonium solution. SEM images of Au triangles after 2 min irradiation with near-IR light. Inset is the calculated field enhancement with polarized light along the two different primary symmetry axes; the red arrows show the maximum of the electrical field. Reproduced with permission from reference 61. Copyright 2017 American Chemical Society. ....	12
Figure 1.10 (a) The strategy for plasmon-induced surface polymerization by growing PNIPAM/PVBA brushes onto alkoxyamine initiator-grafted gold grating. (b) The surface-modified gratings with a covalently attached copolymer were used for SERS	

detection of glycoproteins, and the intensity of characteristic peaks increased up to 2.5-fold. Reproduced with permission from reference 64. Copyright 2019 Royal Society of Chemistry..... 13

Figure 1.11 (a) Strategy to realize near-field guided chemical nanopatterning, followed by regioselective gold nanoparticle assembly. (b) SEM image of a gold crescent after this strategy, showing higher particle densities at the regions with the strongest near-field enhancement that agree well with the theoretical calculation of the intensity distribution of the field enhancement surrounding a gold nano-crescent. Reproduced with permission from reference 65. Copyright 2012 American Chemical Society.... 14

Figure 1.12 Examples of hydrosilylation of unsaturated molecules. (a) Hydrosilylation of an aldehyde, an alkene, and an alkyne with trisubstituted molecular silanes. (b) Hydrosilylation of an aldehyde, an alkene, and an alkyne on a representative silicon surface, Si(111)-H. Reproduced with permission from reference 71. Copyright 2014 American Chemical Society. .... 15

Figure 1.13 (a) Scheme of the typical process of catalytic stamp lithography. (b) AFM height image of a parent Pd catalytic stamp. The diameter of Pd nanoparticle is 40 nm, and the center-to-center spacing is 110 nm. (c) 1-Octadecyne stamped Si(111)-H surface height image; inset image is the height profile along the dashed line and corresponding phase image (d) Reproduced with permission from reference 82. Copyright 2008 American Chemical Society. .... 17

Figure 1.14 AFM height and phase images of H-terminated Si surfaces stamped with eight kinds of molecular inks: (a) Si(111)-H stamped with 1-dodecene; (b) Si(111)-H stamped with 4-vinylpyridine; (c) Si(100)-Hx stamped with 1H,1H,2H-perfluoro-1-decene; (d) Si(111)-H stamped with phenylacetylene; (e) Si(100)-Hx stamped with 10-undecynoic acid; (f) Si(111)-H stamped with undecanal; (g) Si(111)-H stamped with benzaldehyde; (h) Si(111)-H stamped with dodecane. Reproduced with permission from reference 78. Copyright 2009 American Chemical Society..... 18

Figure 1.15 Covalent immobilization of Au nanoparticles onto a Si surface by illumination with visible light. (a) 11-Mercaptoundecene (MUD) modified Au nanoparticle. (b) Visible-light spectrum and irradiation set-up. (c) Mechanistic scheme of Si–H with MUD on Au NP. Reproduced with permission from reference 84. Copyright 2013 American Chemical Society. .... 19

Figure 1.16 (a) Scheme of plasmon-induced hydrosilylation on a flat silicon Si(111)–H surface. White light was filtered by a green bandpass filter, then passed through the transparent PDMS stamp, allowing LSPR excitation of Au nanopatterns. After plasmonic stamping, localized hydrosilylation of alkenes or alkynes patterns occurs on Si surfaces. (b) Scheme of pattern visualization by thiol–ene coupling and electroless gold deposition. (c) SEM micrographs of the resulting gold nanopatterns. Reproduced with permission from reference 86. Copyright 2016 American Chemical Society.... 20

Figure 2.1 (a) Preparation of the plasmonic stamp: a thin gold film was sputtered on top of a PDMS slab, followed by dewetting of the gold with thermal treatment. (b) Plasmonic stamping and hydrosilylation: A thin layer of 1-dodecene was layered on a flat Si(111)–H surface, and the plasmonic stamp was pressed down onto the surface. Light (400–580 nm) was shone through the plasmonic stamp for 60 minutes. .... 25

Figure 2.2 (a) In order to measure the gold film thickness, gold films were sputtered onto a Si wafer cleaned by a standard RCA procedure, and then a cotton swab was used to scratch a line in the gold film. AFM was used to measure the thickness of the gold. (b) Plot of film thickness vs sputtering time, the error bar for the gold film thickness is from one sample with multiple measurements. AFM height images of films with different sputtering times: (c) 10 s, (d) 20 s, (e) 30 s, (f) 40 s, (g) 60 s. All the scale bars are 1  $\mu\text{m}$ . .... 26

Figure 2.3 Photographs of PDMS stamps with varying initial thickness of gold: 5.0 nm (a), 7.0 nm (b), 9.2 nm (c), 11.1 nm (d), 13.1 nm (e), before (black border) and after (red border) thermal dewetting of the gold film. Corresponding UV-vis spectra are shown on the right; black plot before dewetting, and red plot post-dewetting. The green band in the UV-vis plots indicates the spectral window of light used to drive the

plasmonic stamping. All the scale bars are 0.5 cm. Thickness measurements of the sputtered gold films were carried out on a native oxide-capped silicon wafer, as shown in Figure 2.2. .... 27

Figure 2.4 Optical microscope images (1000× magnification) of gold films on PDMS surfaces, (a) before and (b) after gold dewetting. From left to right, initial gold film thickness increased from 5.0 nm to 13.1 nm. All scale bars are 10 μm. (c) AFM height images of dewetted gold films on PDMS, with different initial thicknesses of gold. All scale bars are 200 nm. .... 29

Figure 2.5 (a) - (e) AFM images of plasmonic stamps fabricated from dewetted Au films on PDMS with as-deposited thicknesses ranging from 5.0 to 13.1 nm. All scale bars are 1 μm. .... 29

Figure 2.6 Blank PDMS, heated at 150 °C for 20 h. (a) Optical microscope images (1000× magnification) to show the morphology of the PDMS; scale bar = 10 μm. (b) Corresponding AFM height image. No wrinkles are observed with heating only; scale bar = 500 nm. .... 30

Figure 2.7 As-sputtered 5.0 nm-thick gold on PDMS before heating. (a) Optical microscope images (1000× magnification) to show the morphology of the PDMS; scale bar = 10 μm. (b) Corresponding AFM height image. No wrinkles are observed with gold sputtering only; scale bar = 500 nm. .... 30

Figure 2.8 Mechanism for plasmonic stamp-induced hydrosilylation on a flat Si(111)-H surface. The built-in electric field of the LSPR results in electron-hole pair formation in the silicon, triggering the mechanism for hydrosilylation.  $R = -(CH_2)_9CH_3$ . .... 32

Figure 2.9 Summary of the measured values of static water contact angles of Si(111)-H surfaces under various conditions, including control experiments. Detailed statistics and errors are found in Table 2.2. .... 32

Figure 2.10 AFM height maps and static water contact angles of Si(111)-H surfaces reacted with 1-dodecene under illumination with light (400–580 nm) using plasmonic

stamps with different thicknesses of as-sputtered gold films: 0 nm (a), 5.0 nm (b), 7.1 nm (c) and 9.2 nm (d). All scale bars are 200 nm..... 35

Figure 2.11 Hydrosilylation visualization using gold nanoparticle deposition. (a) Schematic outline of galvanic displacement with aqueous  $\text{KAuCl}_4$  and HF: hydrosilylated regions prevent galvanic displacement of metallic gold, thus enabling their visualization as dark, unreacted regions. (b-d) Silicon surfaces that have been hydrosilylated with plasmonic stamps of different initial thickness of gold films (5.0 nm, 7.0 nm and 9.2 nm). All the scale bars are 200 nm. .... 36

Figure 2.12 AFM image of the Si(111)-H sample after (i) hydrosilylation using a plasmonic stamp with a sputtered gold film thickness of 9.2 nm, and (ii) galvanic displacement with the aqueous  $\text{KAuCl}_4$  and HF solution indicated in Figure S9; scale bar = 200 nm. .... 37

Figure 2.13 Method for visualization of hydrosilylation using gold nanoparticle fiducials. (a) Schematic outline of gold deposition via galvanic displacement. (b+c) SEM micrograph of two different silicon surfaces: (b) The Si(111)-H surface was functionalized with a monolayer of 1-dodecene by thermal-induced hydrosilylation (150 °C, 24 h), followed by exposure to an aqueous 1 mM  $\text{KAuCl}_4$  and 1% HF mixture for 5 min at room temperature in air. The SEM image shows no gold deposited onto the Si wafer (image with red border). (c) Immersing a freshly etched sample of Si(111)-H into the same aqueous  $\text{KAuCl}_4$  and HF mixture solution directly resulted in gold deposition via galvanic displacement on the silicon surface (image with blue border). (d) XPS spectra of Au(4f) of the Si(111)-H treated wafer upon galvanic displacement confirms the presence of Au(0); SEM scale bar = 200 nm..... 37

Figure 2.14 Transmission spectrum of the band-pass filter used for plasmonic stamping (CW 526 nm, fwhm: 180 nm, Edmund Optics Inc.)..... 39

Figure 2.15 Photograph of a customized experimental setup for plasmonic stamping: a silicon wafer was stamped with a plasmonic stamp and sandwiched between a quartz

coverslip and a customized reaction holder, which was made of polytetrafluoroethylene (PTFE). Two clips were applied on both sides of the sandwich structure..... 42

Figure 3.1 (a) Scheme of azo-dimerization reactions of PATP and PNTP molecules, monitored by high-vacuum TERS. (b) Raman peak intensity ratio of  $I_{C-N}/I_{C-S}$  on Ag surfaces, which were oxidized for different time durations in air, varying from 0.5 to 60 h. The ratio increased with the oxidation time, indicating that more PATP molecules converted into DMAB molecules on the Ag surface. Reproduced with permission from reference 151. Copyright 2020 American Chemical Society. .... 44

Figure 3.2 Water contact angle of the surface of Si(111)-H coated with neat hexadecene and 0.25 M PhCl in hexadecene and irradiated with 254 nm light. Reproduced with permission from reference 155. Copyright 2012 American Chemical Society. .... 45

Figure 3.3 Four additional methods tested for the fabrication of plasmonic stamps. (a) Preparation of gold hexagonal patterns on silicon wafers via block copolymer metallization followed by transfer of the gold nanoparticles to PDMS. (b) Gold nanorods with tunable aspect ratios were synthesized and then deposited onto blank PDMS. Wet chemistry needs multiple synthetic and purification steps, and surface ligands on gold nanorods could be an obstacle for the following reaction. (c) Deposition of polystyrene (PS) nanospheres on PDMS directly, followed by gold deposition. This approach was complicated by residual PS spheres. (d) Preparation of gold nanorods of various sizes by electron-beam lithography (EBL) on silicon wafers, followed by transfer to PDMS. The gold nanorods could not be removed by the PDMS..... 46

Figure 3.4 SEM images of the as-sputtered 5.0 and 10.0 nm thickness gold film on Si wafers with different sputtering rate, (a) 0.16 nm/s, (b) 0.22 nm/s. .... 48

Figure 3.5 SEM images of the as-sputtered gold film on Si wafers with the same sputtering rate (0.22 nm/s), but different thickness (2.5 nm, 5.0 nm, 7.5 nm, 10.0 nm), before (top row) and after (bottom row) dewetting via thermal treatment at 150 °C for 20 h..... 48

Figure 3.6 Gold films were sputtered onto Si wafers, and AFM height graphs were used to measure the thickness of the gold film. The thickness of gold films are (a)  $2.5 \pm 0.3$  nm, (b)  $5.0 \pm 0.3$  nm, (c)  $7.5 \pm 0.2$  nm, (d)  $10.0 \pm 0.2$  nm, which agree well with the designed thickness, confirming the thickness accuracy and reproducibility of this method..... 49

Figure 3.7 (a) Schematic representation of gold dewetting on PDMS process. (b) AFM height images of plasmonic stamps fabricated from dewetted Au films on PDMS. (c) UV-vis spectra for ten plasmonic stamps; the inset photograph is the plasmonic stamp. .... 50

Figure 3.8 Scheme of plasmonic stamp-assisted hydrosilylation on a Si(111)-H surface. Green light shines through the optically transparent, PDMS-based plasmonic stamp with gold nanoparticle on the surface. Hydrosilylation occurs in a spatially defined fashion on the Si(111)-H surface, resulting in the increment of water contact angle from  $\sim 83^\circ$  to  $\sim 105^\circ$ . .... 51

Figure 3.9 Kinetic profile of plasmonic stamp-assisted hydrosilylation on a hydrogen-terminated Si(111) surface of various doping densities and types. Data is fitted to the pseudo-first-order kinetics (equation 3.4). Each black dot represents a unique sample that had been reacted for the indicated reaction time. The error bars represent the standard deviation of five measurements..... 52

Figure 3.10 High-resolution X-ray photoelectron spectroscopy (XPS) of each sample was taken of the F(1s) and Si(2p) regions. The hydrosilylation of 1H,1H,2H-perfluoro-1-decene on Si(111)-H occurred on different silicon wafers through plasmonic stamps for 1 h. (a) n-type silicon, (b) p-type silicon, (c) n<sup>++</sup>-type silicon, (d) p<sup>++</sup>-type silicon, and (e) intrinsic silicon..... 53

Figure 3.11 Theoretical band diagrams of the gold-organic-silicon junction for different doping levels and types of Si substrates. All band diagrams are shown to a distance of 800 nm from the interface and were calculated using the Mott-Schottky

rule. Reproduced with permission from reference 86. Copyright 2016 American Chemical Society. .... 57

Figure 4.1 (a) Schematic of Pd-Ni bimetallic catalyst preparation via colloidal techniques (PdNi<sub>12</sub>-COL). (b) TEM images of the PdNi<sub>12</sub>-COL catalyst: nanoparticles before deposition on the support (“fresh”); (c) after deposition and calcination for 16 h at 550 °C (“calcined”), and after hydrothermal aging (methane combustion) for 40 h (“aged”). Reproduced with permission from reference 190. Copyright 2015 American Chemical Society. .... 68

Figure 4.2 Catalytic oxidation reactions by yolk-shell nanoparticles. (a) Au@void@ZrO<sub>2</sub> nanoparticles were synthesized and tested for CO oxidation. (b) Pd yolk-shell nanoparticles with an outer shell based on periodic mesoporous organosilica were synthesized for the selective oxidation of various alcohol substrates. Reproduced with permission from reference 219 and 220. Copyright 2006, 2012 Wiley-VCH.... 70

Figure 4.3 Catalytic reduction reactions by yolk-shell nanoparticles (a) The Au@SiO<sub>2</sub> yolk-shell nanostructure was synthesized by selective etching of the gold cores in Au@SiO<sub>2</sub> core-shell particles. This nanoreactor system was used to catalyze the reduction of *p*-nitrophenol. (b) The gold cores of Au@SiO<sub>2</sub> yolk-shell catalysts were functionalized selectively by the addition of 3-MPA, which generated carboxylate anions on the surface. It was a very effective means of increasing the reaction rates of 2-nitroaniline reduction. (c) Au@carbon yolk-shell nanoparticles were synthesized as the catalyst for hydrophobic nitrobenzene reduction. Reproduced with permission from reference 221, 222, and 223. Copyright 2008 Wiley-VCH, Copyright 2008 American Chemical Society, and Copyright 2013 Royal Society of Chemistry, respectively. .. 71

Figure 4.4 (a) S/TEM images of the cubic Pd-Pt nanoparticles. (b) EDX images for Pd-Pt nanoparticles, and corresponding EDX spectrum (c) for Pd, Pt element quantification. .... 74

Figure 4.5 From left to right, schematic figures, TEM images, 10× enlarged TEM images and size distribution histograms for (a) Pd-Pt nanoparticles; (b) Pd-Pt

nanoparticles@SiO<sub>2</sub>; (c) Pd-Pt nanoparticles@SiO<sub>2</sub>@ZrO<sub>2</sub>; (d) Pd-Pt nanoparticles@void@ZrO<sub>2</sub>. Notably, for the size distribution histograms, from top to bottom, is the diameter of (a) Pd-Pt nanoparticles; (b) Pd-Pt nanoparticles@SiO<sub>2</sub>; (c) Pd-Pt nanoparticles@SiO<sub>2</sub>@ZrO<sub>2</sub>; and ZrO<sub>2</sub> shell thickness of (d) Pd-Pt nanoparticles@void@ZrO<sub>2</sub>..... 75

Figure 4.6 TEM images for TEOS/Pd-Pt ratio control experiments, Pd-Pt@SiO<sub>2</sub> core-shell nanoparticles synthesized under lower amounts of TEOS (TEOS volume, X < 60 μL): the silica shell contained multiple Pt particles; higher (TEOS volume, X > 80 μL) amounts of TEOS: a mixture of Pd-Pt@SiO<sub>2</sub> and silica particles without cores; compared to the Pd-Pt@SiO<sub>2</sub> nanoparticles synthesized under the optimum TEOS amounts ( X = 70 μL) shown in Figure 4.5b, where each Pt particle is encaged within a silica shell. Reaction conditions: 10 mL PVP-stabilized Pd-Pt dispersed in EtOH, 0.5 mL NH<sub>4</sub>OH, 0.9 mL water, X μL TEOS, continued by stirring at room temperature for 24 h. No centrifugation or other purification. .... 76

Figure 4.7 Before ZrO<sub>2</sub> encapsulation, as-prepared Pd-Pt@SiO<sub>2</sub> nanoparticles need to be washed with water and absolute ethanol, respectively. If only washed with water, ZrO<sub>2</sub> will not be encapsulated onto the SiO<sub>2</sub> surface as shown in the TEM image.... 77

Figure 4.8 When using a lower amount of zirconium butoxide than the optimized amount, the shell of ZrO<sub>2</sub> is very thin, and some Pd-Pt nanoparticles are released from the yolk-shell nanostructures (highlighted in the white circle)..... 78

Figure 4.9 Observed fracturing of the Pd-Pt@void@ZrO<sub>2</sub> yolk-shell nanoparticles upon sonication for 5 min in a water solution..... 79

Figure 4.10 (a) TEM images and EDX mapping images for Pd/Co/Al<sub>2</sub>O<sub>3</sub> catalyst, synthesized by galvanic displacement. By comparing catalytic activity of methane combustion with Pd/Co/Al<sub>2</sub>O<sub>3</sub> impregnated catalyst, methane combustion over Pd/Co/Al<sub>2</sub>O<sub>3</sub>-GD (galvanic displacement) proceeded at a temperature about 50 °C lower than that over impregnated catalyst. Reproduced with permission from reference 45 (Copyright 2016 Royal Society of Chemistry). (b) TEM images and EDX mapping

images of Al<sub>2</sub>O<sub>3</sub>/Pd/SiO<sub>2</sub> catalyst, prepared by an atomic layer deposition method. Ignition–extinction curves show the catalyst delivered full methane conversion at 400 °C and maintained its activity during the five cycles. Reproduced with permission from reference 250. Copyright 2019 Wiley-VCH. .... 80

Figure 4.11 Nitrogen adsorption (red) and desorption (blue) isotherms for (a) Pd-Pt@void@ZrO<sub>2</sub> yolk-shell nanoparticles, (b) Pd-Pt@ZrO<sub>2</sub> directly, (c) Pd-Pt/ZrO<sub>2</sub> impregnated catalyst. .... 81

Figure 4.12 TEM images of Pd-Pt@ZrO<sub>2</sub> core-shell nanoparticles. (a) Pd-Pt nanoparticles reacted with zirconium butoxide, Lutensol XP50, water, and ethanol. The Pd-Pt nanoparticles were synthesized using the same protocols as that of Pd-Pt@void@ZrO<sub>2</sub>, hence, Pd-Pt nanoparticles are of cubic shape, and the side length is ~8 nm in solution; (b) after calcination at 600 °C for 6 h, the shape of Pd-Pt nanoparticles changes from cube to sphere, size is still comparable, although some become bigger because of the thermal aggregation; (c) after 42 h hydrothermal ageing (methane combustion), Pd-Pt nanoparticles can be seen through the ZrO<sub>2</sub> shell. As the Pd-Pt nanoparticles are immobilized by the ZrO<sub>2</sub> shell, the size is still comparable, although some become bigger due to aggregation..... 82

Figure 4.13 TEM images (a), (b) and EDX mapping images (c) for prepared Pd-Pt/ZrO<sub>2</sub> impregnated catalysts. The size of Pd-Pt nanoparticles is  $7.7 \pm 5.0$  nm. The Pd and Pt elements are distributed all over the surface as there is no washing step for the conventional impregnation method, i.e., just calcination of the mix solution of palladium chloride, hexachloroplatinic acid with ZrO<sub>2</sub> powder. However, we can see Pd-Pt nanoparticles on the surface (white arrow), especially compared to the Zr element map. (d) TEM image for the used Pd-Pt/ZrO<sub>2</sub> impregnated catalyst after 42 h hydrothermal ageing (methane combustion). The average size of Pd-Pt nanoparticles is  $29.8 \pm 11.3$  nm. .... 83

Figure 4.14 Ignition (solid circle) and extinction (hollow circle) curves on the left side and hydrothermal tests on the right side for three different Pd-Pt on ZrO<sub>2</sub> catalysts (a) Pd-Pt@void@ZrO<sub>2</sub> yolk-shell nanoparticles, (b) Pd-Pt@ZrO<sub>2</sub> directly, (c) Pd-Pt

impregnated on ZrO<sub>2</sub>. For the ignition–extinction curves, the catalyst was tested at 300, 350, 400, 450, 500, 550, 600, and 650 °C during ignition, and then tested at 650, 600, 550, 500, 450, 400, 350, 300 °C during extinction, for 30 min at each temperature. For the hydrothermal tests, they were done after the ignition–extinction test, so we know the estimated 100% conversion (~650 °C) and 50% conversion temperature (~475 °C). Thus, the temperature was cycling between 650 and 475 °C for 1 h at each temperature; in total, eight cycles in about 22 h. Then, reactor temperature was held at 475 °C for another 20 h..... 85

Figure 4.15 TEM image of the Pd-Pt@void@ZrO<sub>2</sub> yolk-shell nanoparticles after the hydrothermal aging test for 42 h. All yolk-shell particles are not sintered, and the hollow structures are still intact when compared to Figure 4.5d. .... 86

Figure 4.16 (a) Increasing the metal loading by decreasing the void volume of the nanostructures, so that we get smaller yolk-shell nanoparticles, from 204 ± 44 nm to 100 ± 21 nm and Pd metal loading from 0.57 % to 1.23 %. (b) The corresponding ignition (solid circle) and extinction (open circle) curves for yolk-shell nanoparticles with higher metal loading and longer etching time. .... 88

Figure 5.1 Aluminum as a plasmonic material. (a) Plasmon tuning ranges of the most common plasmonic materials, Au and Ag, compared with Al. (b) Calculated spectra for a 35-nm thick, 50 nm diameter Al nanodisk: (i) a pure, isolated Al nanodisk (black); (ii) an isolated Al nanodisk with a 3 nm surface oxide (green); and (iii) the same Al nanodisk on an infinite SiO<sub>2</sub> substrate (orange). Reproduced with permission from reference 256. Copyright 2014 American Chemical Society. .... 97

Figure 5.2 Scheme of nanofabrication for Au-Ag nanoparticles by using successive thin film deposition and thermal dewetting. The individual and total film thicknesses of Au and Ag determine the Au/Ag fractions and the average diameter of nanoparticles. High-angle annular dark-field (HAADF) and energy-dispersive X-ray (EDX) mapping of Au and Ag elements. Reproduced with permission from reference 259. Copyright 2017 American Chemical Society. .... 98

Figure 5.3 Left: SEM images of gold nanoparticles with different sizes and shapes (sphere, rod, square, and triangle) fabricated by EBL. Right: zoom in SEM of gold nanotriangles and nanorods..... 99

Figure 5.4 Scheme of two different fabrication ways used to embed metallic patterns into soft PDMS. TFOS: tridecafluoro-1,1,2,2-tetrahydro-octyl-1-trichlorosilane; PR: photoresist; MPT: 3-mercaptopropyl trimethoxysilane. Reproduced with permission from reference 267. Copyright 2005 Wiley-VCH. .... 100

Figure 5.5 Schematic representation of synthesizes Pd-Pt@porous SiO<sub>2</sub> via magnesiothermic reduction. .... 101

# List of Abbreviations

LSPs	Localized Surface Plasmons
LSPR	Localized Surface Plasmon Resonance
NP	Nanoparticles
PDMS	Polydimethylsiloxane
HV	High Vacuum
TERS	Tip Enhanced Raman Spectroscopy
PS- <i>b</i> -P2VP	Polystyrene-block-poly-2-vinylpyridine
AFM	Atomic Force Microscopy
XPS	X-ray Photoelectron Spectroscopy
MIS	Metal-insulator-semiconductor
SEM	Scanning Electron Microscopy
FWHM	Full Width at Half Maximum
PTFE	Polytetrafluoroethylene
SERS	Surface Enhanced Raman Spectroscopy
MIS	Metal-hole Pair
EHP	Electron-insulator-semiconductor
CW	Continuous Wave
TEM	Transmission Electron Microscopy
HRTEM	High Resolution Transmission Electron Microscopy
EDX	Energy Dispersive X-ray Spectroscopy
TEOS	Tetraethylorthosilicate
BET	Brunauer-Emmett-Teller
BJH	Barrett-Joyner-Halenda
ICP-MS	Inductively Coupled Plasma Mass Spectroscopy
EBL	Electron Beam Lithography

# Chapter 1 Introduction

## 1.1 Overview

Plasmonic nanostructures exhibit special unique properties arising when localized surface plasmons (LSPs), free electrons at the boundary of a conductor and a dielectric, are illuminated. Irradiation of these LSPs at their frequency of absorption is called resonance and is termed localized surface plasmon resonance (LSPR).<sup>1-4</sup> In addition to the intense absorption of LSPRs, they also are accompanied by intense proximal and localized electrical fields that can be harnessed to drive chemical reactions, such as organic molecular transformations, CO<sub>2</sub> reduction, and conversion of different carbon feedstocks into gas or liquid fuels,<sup>5-8</sup> shown in Figure 1.1.

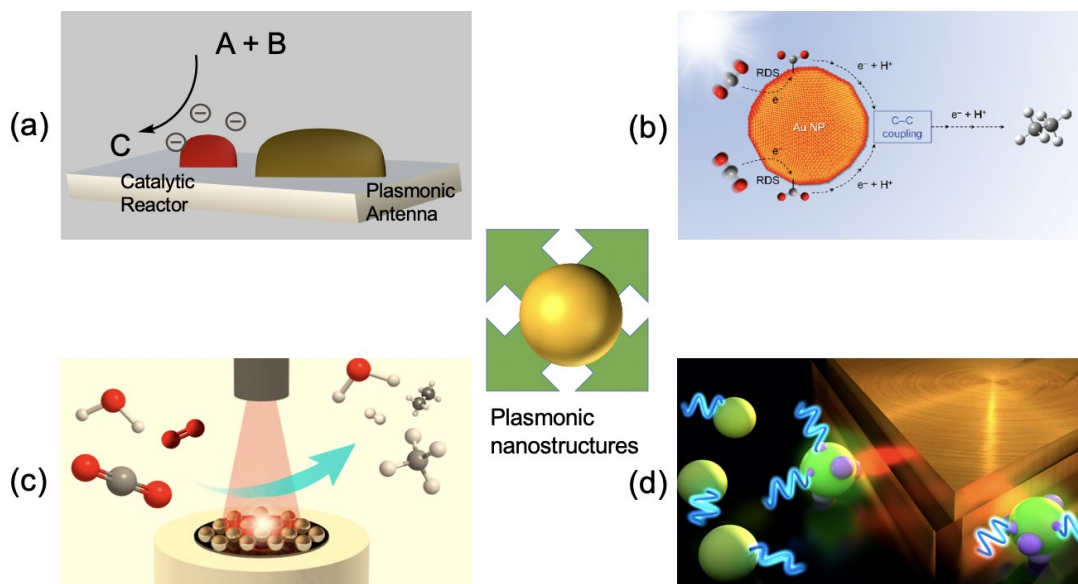


**Figure 1.1** (a) Schematic of a simple system containing a plasmonic antenna coupled through localized near-field enhancements to a catalytic reactor metal nanoparticle for organic molecular transformations. (b) Schematic of the reaction system for Au NP-photocatalyzed CO<sub>2</sub> conversion to hydrocarbons under plasmonic excitation. (c) Simplified representation of plasmon-mediated electrocatalysis to convert feedstocks into fuels. (d) Schematic illustration of the metal photo-staining method, wherein photogenerated carriers drive the deposition of Pt on semiconductor nanostructures in the presence of a plasmonic antenna. Reproduced with permission from reference 6, 7, 8. Copyright 2018 American Chemical Society.

When in close proximity to a semiconductor (a few nanometers or less), metallic nanoparticles with LSPRs can generate charge carriers (electrons and holes), which then can be harnessed to drive the chemistry on the semiconductor surface.<sup>9, 10</sup> This thesis focuses upon such a reaction, plasmon-driven hydrosilylation reaction, which enables the functionalization of silicon surfaces with a wide range of hydrocarbons. As will be shown here, plasmon-driven hydrosilylation is triggered using gold nanoparticle-on-PDMS stamps, termed plasmonic stamps, to perform Si–C bond formation on hydrogen-terminated silicon surfaces in a fast and clean manner. The Si–C bond forming reaction is based upon the hydrosilylation of alkenes and is a practical approach to functionalize the surface of this semiconductor through stable Si–C bonds.

As a general introduction, this chapter will consist of a brief overview of the two main fields, plasmonics and hydrosilylation. Specifically, this chapter will commence with a discussion of the concept of plasmonics and known plasmon-driven reactions, with an overview of their proposed mechanisms, including confined plasmonic fields, hot carrier excitation, and local heat generation. After briefly summarizing the recent advances of plasmon-driven reactions for surface functionalization with molecular entities, polymers, and nanomaterials, an introduction regarding surface functionalization on silicon surfaces via hydrosilylation will be provided. Finally, hydrosilylation triggered by metallic nanoparticles comprising Pd, Pt, and Au nanoparticles embedded in soft PDMS stamps will be described in detail.

## **1.2 Plasmonics**

### **1.2.1 Overview of Plasmons**

Plasmons are the collective oscillation of free charges in a conducting material.<sup>11, 12</sup> The surface plasmons (SP) are oscillations confined to the surfaces of conducting materials and interact strongly with light.<sup>13–16</sup> Specifically, a surface plasmon refers to the collective oscillation of electrons at the interface of a metal and dielectrics, resulting in surface plasmon polarization at the interface when a certain frequency of photons matches the inherent frequency of the electrons.<sup>17, 18</sup> There are two forms of surface plasmons. When the surface plasmons propagate along the metal/dielectric

interface, this phenomenon is called propagating surface plasmons. When surface plasmons are trapped at the metal/dielectric interface, which results in high-intensity electric-fields (or hot spots), this phenomenon is called localized surface plasmon (LSP),<sup>19</sup> as illustrated in Figure 1.2.

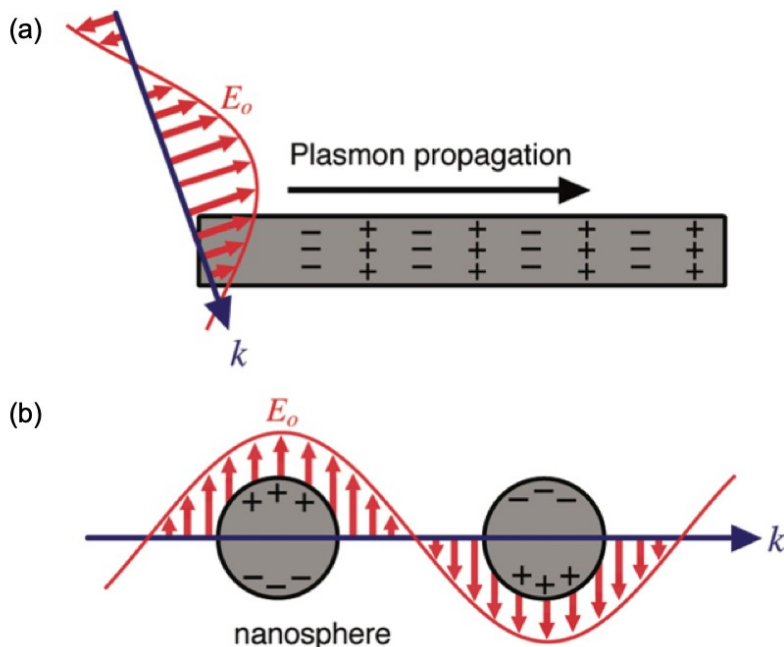


**Figure 1.2** Schematic illustration of two forms of surface plasmons excited by the electric field ( $E_o$ ) of incident light with wavevector ( $k$ ). (a) The metal/dielectric interface has one dimension much larger than the wavelength of light. In this case, a propagating surface plasmon can travel along the surface of the metal. (b) The nanosphere is smaller than the wavelength of light, and the free electrons can be displaced from the lattice of positive ions and oscillate collectively in resonance with the light. This process is named localized surface plasmon resonance (LSPR). Reproduced with permission from reference 19. Copyright 2011 American Chemical Society.

### 1.2.2 Plasmonic Metal Nanostructures

In 1857, Michael Faraday was the first to describe the unusual optical properties of gold colloid solutions systematically.<sup>20</sup> This solution was called “a beautiful ruby fluid”, as shown in Figure 1.3. Faraday’s ideas inspired Mie’s later theoretical work; in 1908, Guastav Mie was first to point out the surface plasmon resonance.<sup>21</sup> For a spherical metal nanoparticle with a size much smaller than the wavelength of the incident light,

the surface oscillation is determined mainly by the particle volume, dielectric function of the metal, and surrounding medium.<sup>22, 23</sup>

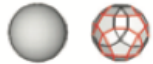
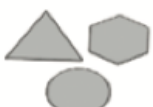
The most attractive plasmonic metal nanostructures for optical applications are composed of gold (Au), silver (Ag), and copper (Cu),<sup>24-26</sup> as they exhibit resonance when interacting with ultraviolet (UV) to visible (vis) light (Figure 1.4a). The SPR frequency depends not only on the composition but also on the size and shape of the nanoparticles. For example, the plasmon resonance of silver nanoparticles can be shifted from the UV to the visible range by maximizing the nanocube size or changing the shape of nanoparticles (Figure 1.4b, c).

Theoretically speaking, it is possible to design plasmonic nanostructures that interact with the whole solar spectrum by manipulating precisely the composition, size, and shape.<sup>27-29</sup> For example, Table 1.1 lists silver nanoparticles with different shapes and the corresponding LSPR peaks that can be tuned from 320 nm to 1000 nm.



**Figure 1.3 Gold colloid microscope slide that Faraday used in his lecture to illustrate his work on gold colloids in 1857; it is stored in the Whipple Museum of the history of science, University of Cambridge. The inscription is “Faraday’s gold given to me himself after his lecture at the RI”. Reproduced with permission from reference 17. Copyright 2011 American Chemical Society.**

**Table 1.1 Summary of the Shapes, LSPR Absorption Peaks for Silver Nanoparticles. Reproduced with Permission From Reference 19. Copyright 2011 American Chemical Society.**

Shape	Illustration	LSPR <sup>a</sup>
Sphere and quasi-sphere		320–450
Cube and truncated cube		400–480
Tetrahedron and truncated tetrahedron		350–450
Octahedron and truncated octahedron		400–500
Bar		350–900
Spheroid		350–900
Right bipyramid		500–700
Beam		—
Decahedron		350–450
Wire and rod		380–460
Polygonal plates and disc		350–1000
Branched structures		400–1100
Hollow structures		380–800

<sup>a</sup> The main absorption peak (nm).

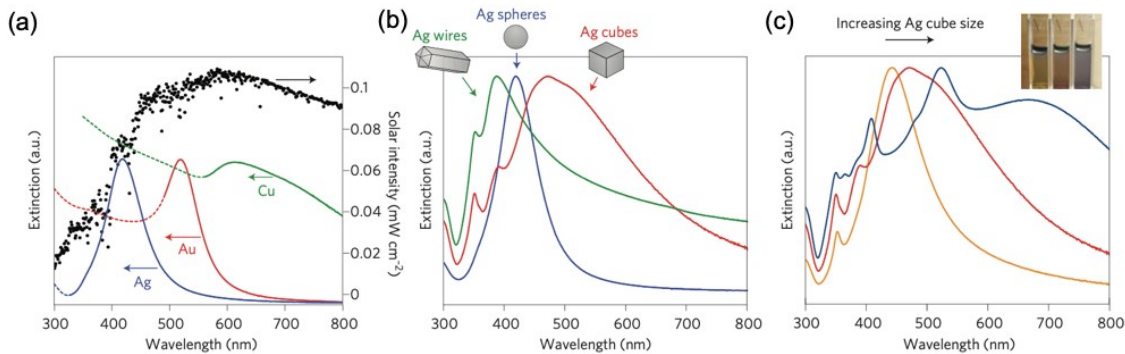


**Figure 1.4 Overview of surface plasmon properties of plasmonic metal nanoparticles. SPR peaks vary with different types of composition (a), shapes (b), and sizes (c). The intensity of the solar radiation curve (black) also is shown in (a). Reproduced with permission from reference 24. Copyright 2015 Nature Publishing Group.**

### 1.3 Plasmon-driven Reactions

Plasmonic metal nanoparticles are light-harvesting materials, which interact with visible light by the excitation of localized surface plasmon resonance, termed LSPR.<sup>30</sup> In this physical process, plasmonic metal nanoparticles absorb the energy from the light, and concentrate it near the surface of the nanoparticles. When these nanoparticles are used to drive a chemical reaction, the light energy ultimately can be converted to chemical energy.<sup>31–33</sup> Recently, plasmon-driven oxidation/reduction processes without any other additional catalysts, have drawn tremendous attention. Plasmon excitation and decay provide ways to manipulate light within a sub-femtosecond on the nanoscale, enabling precision chemistry.<sup>34, 35</sup> Sketches of the photoexcitation and relaxation processes are illustrated in Figure 1.5. First, the photophysics start with plasmon excitation of the nanoparticle, resulting in a highly elevated plasmonic field at the nanoparticle surface. Next, the oscillation of free electrons decays rapidly via excitation of hot carriers. Through electron–electron scattering, these excited electrons thermalize quickly, followed by a heat distribution cooling by coupling of phonons and “hot electrons”, leading to thermal dissipation to surroundings.<sup>36</sup> By taking advantage of the plasmon excitation, hot carrier generation, and carrier thermalization processes, chemical reactions can be driven via three possible mechanisms: i) reactions enabled

by a confined plasmonic field, ii) hot carrier generation, and iii) generation of localized heat.<sup>34-39</sup>

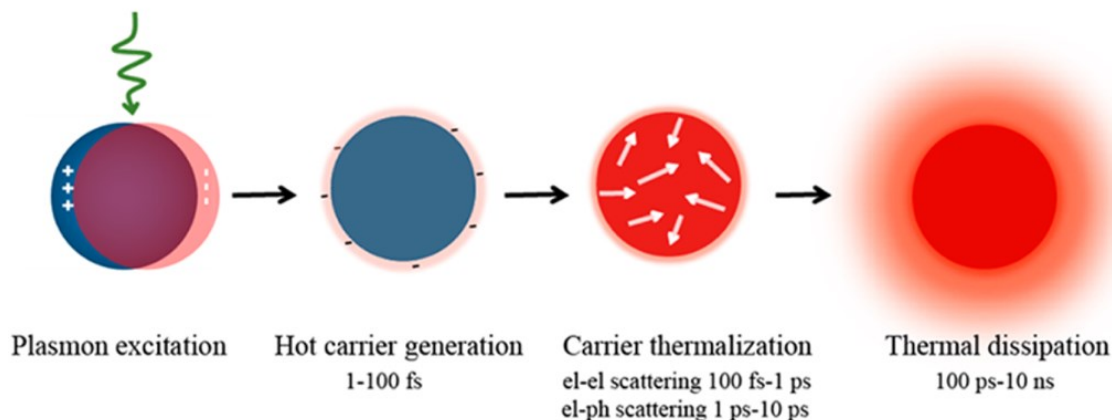


**Figure 1.5** Sketches of the photoexcitation and subsequent relaxation processes of the LSPR. Reproduced with permission from reference 36. Copyright 2019 American Chemical Society.

### 1.3.1 Plasmon Field-driven Catalysis

LSPR excitation of surface plasmon resonance in metal nanoparticles leads to the confinement of the light energy and forms a highly enhanced plasmonic field on the surface of the metal nanoparticles. One example of chemistry that is assisted by the enhanced plasmonic field is the decomposition of methylene blue, whose rate is enhanced seven times, as shown in Figure 1.6.<sup>40</sup> The LSPR effect of Ag nanoparticles causes a tremendous increase of the near-field amplitude at well-defined wavelengths in the UV region, which overlaps with the bandgap of TiO<sub>2</sub>. Therefore, more electron-hole pairs are excited in TiO<sub>2</sub>, and the photocatalytic activity of TiO<sub>2</sub> is improved.

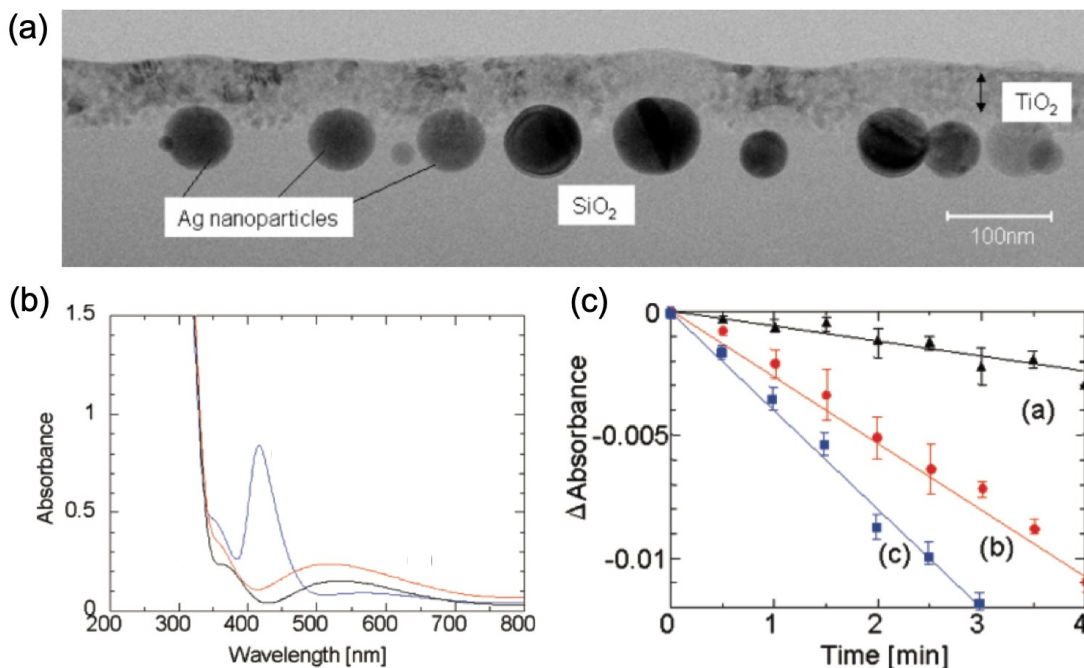


Figure 1.6 (a) TEM image of the cross-section of a TiO<sub>2</sub> film on Ag@SiO<sub>2</sub> core-shell on a SiO<sub>2</sub> substrate, (b) optical absorption spectra of TiO<sub>2</sub> thin film (black), Ag nanoparticles embedded in TiO<sub>2</sub> (orange), and Ag nanoparticles covered with SiO<sub>2</sub> layer embedded in TiO<sub>2</sub> (blue), and (c) decomposition rates of methylene blue (MB) on TiO<sub>2</sub> surfaces under near-UV irradiation. Reproduced with permission from reference 40. Copyright 2008 American Chemical Society.

### 1.3.2 Hot Carrier-driven Catalysis

The energy stored in the plasmonic field can induce hot carriers in the metal, and these plasmon-mediated hot carriers can be transferred to molecules through a transient electronic exchange between the metal and the molecules.<sup>35</sup> Thus, molecules with the addition of high-energy electrons are created with the electronic exchange, which is sufficient to induce a chemical reaction. Sun et al. designed a home-built high vacuum tip-enhanced Raman spectroscopy (HV-TERS) that can be used for plasmon-driven chemical reactions of 4-nitrobenzenethiol dimerizing to dimercaptoazobenzene.<sup>41</sup> Because of the “hot spot” from the tip, the high density of hot electrons arising from strong plasmon resonances could be transferred to the 4-nitrobenzenethiol near the metal surface to induce its dimerization, as shown in Figure 1.7.

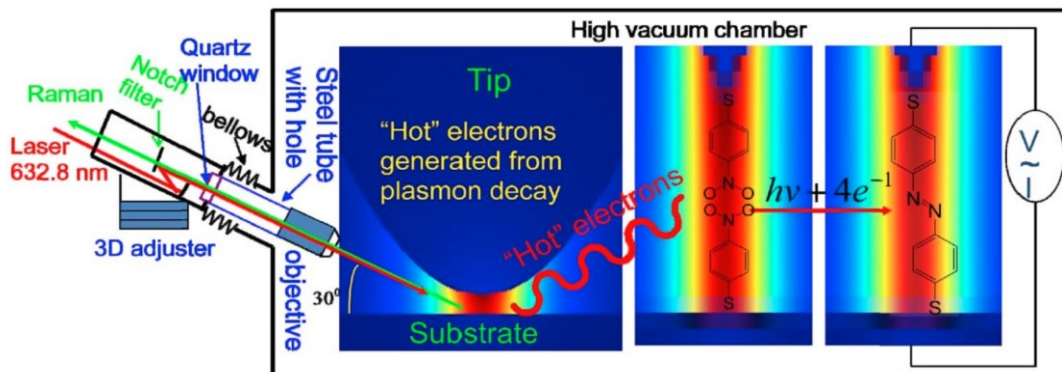
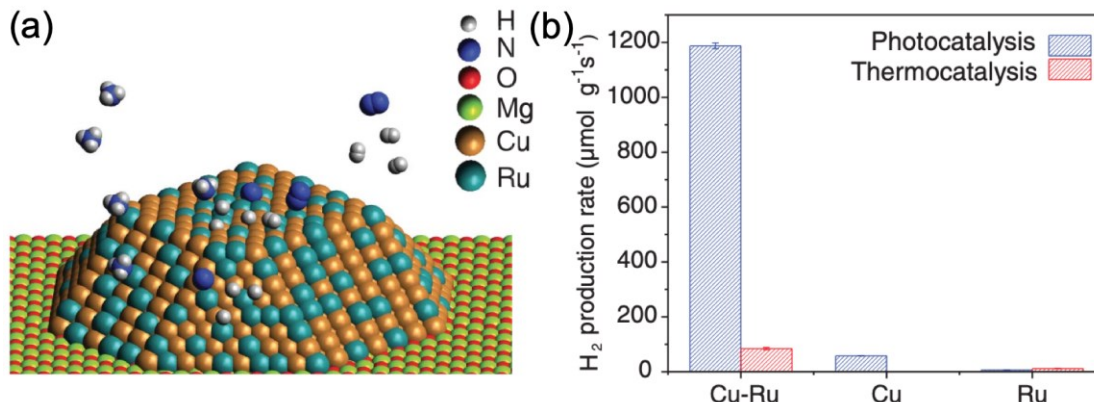


Figure 1.7 Hot electron driven chemical reactions of 4-nitrobenzenethiol revealed by HV-TERS. Reproduced with permission from reference 41. Copyright 2012 Nature Publishing Group.

### 1.3.3 Plasmonic Thermal Catalysis

The hot electron–hole pairs ultimately dissipate by coupling to phonon modes of the metal nanoparticles, resulting in a higher lattice temperature. The thermal energy can be used to overcome the reaction barrier, which also is a promising approach to facilitate plasmon-mediated chemical reactions. Notably, the contribution of the thermal effect among other characteristics of the plasmon in the plasmonic-based catalytic reaction is hard to distinguish. One of the widely accepted ideas is that the excitation of hot electrons played the main role in plasmonic catalysis, rather than the thermal effect itself.<sup>42–44</sup> The concept of a light-dependent activation barrier, which was introduced by Prof. Halas in 2018, was used to distinguish thermal from nonthermal effects in the process of plasmonic catalysis (Figure 1.8).<sup>1</sup> Cu-Ru metal catalysts were measured with a thermal imaging camera to account for the photothermal effect at different illumination wavelengths and intensities. It was demonstrated that the reaction barrier of ammonia decomposition on a plasmonic photocatalyst has an electronic origin. The hot electrons can induce multiple vibrational transitions of the reactant molecule, and, as the vibrational energy stored in the bond increases, the activation energy is reduced. More recently, a review paper summarizes the simple experimental procedures that can help researchers detect and, in some cases, quantify photo-thermal effects in plasmon-assisted chemical reactions, including varying the illumination power, light beam diameter, infrared and thermocouple measurements, minding time

scales, calibrating with bubble formation, and comparing the effects of two polarizations and several wavelengths.<sup>45</sup>



**Figure 1.8 Catalytic ammonia decomposition.** (a) Schematic of the structure consisting of a Cu nanoparticle antenna with a Cu-Ru surface alloy, where the Ru provides the reactor sites. This catalyst was used to quantify the contributions of hot carriers and the photothermal effect. (b) H<sub>2</sub> formation rate in photo- and thermally catalyzed reactions. Reproduced with permission from reference 1. Copyright 2018 American Association for the Advancement of Science.

## 1.4 Plasmon-driven Catalysis for Functionalization of Surfaces

### 1.4.1 Overview

Wolfgang Ernst Pauli, one of the pioneers of quantum physics and recipient of the Nobel Prize in Physics in 1945, once said, “God made the bulk; the surface was invented by the devil.” Pauli explained that the diabolical properties of surfaces were due to the simple fact that surface atoms do not have an isotropic environment. They interact with three different types of atoms, those in the bulk below, other atoms from the same surface, and atoms in the adjacent phase.<sup>46</sup> In other words, bulk materials can provide intrinsic properties, but the surfaces offer more possibilities.

When combining plasmonics with surface chemistry, one arrives at a newly developed research field in the last decade. Because of the confined plasmonic field, hot carrier excitation, and local heat generation, plasmonic nanoparticles have been used to activate bond formation and/or dissociation and induce the chemical reactions

with spatial control on the nanoscale. Although different kinds of techniques, such as dip-pen lithography,<sup>47–49</sup> inkjet printing,<sup>50–52</sup> and direct laser patterning,<sup>53–55</sup> have been reported to control surface functionalities spatially, these methods are expensive, time-consuming, and cannot achieve sub-50 nm resolution easily. Plasmon-driven surface chemistry, however, offers a very fast, cost-effective, and scalable approach. The site-selective surface functionalization can occur by placing molecules or nanostructures at specific reactive spots by using the localized plasmon from the surrounding nanostructure.<sup>56–58</sup> As the proposed mechanisms of plasmon-driven surface functionalization are related to the strong electric field, hot carrier release, and heat dissipation, which we already discussed, and as surface properties are directly related to the grafting molecules, so the various plasmon-driven surface functionalization strategies will be divided into three main sections, namely, molecular entities, polymers, and nanoparticles.<sup>59</sup>

#### **1.4.2 Plasmon-driven Surface Grafting of Molecules**

There are many examples of functionalization strategies to modify surfaces with molecules. To date, only a few examples of spatial or patterned control of surface-grafted molecules by LSPR excitation have been reported. One example is a plasmon-mediated approach that was used as an effective means to modify the surfaces of gold coated optical fibers by iodonium salts under mild reaction conditions. The plasmon is excited by the coupling of the Au-covered optical fiber with the laser light source, with a wavelength corresponding to the plasmon absorption band.<sup>60</sup> Typically, surface modification of optical fibers of silica by iodonium salts requires aggressive agents and strong bases, such as alkali metals. Another example is shown in Figure 1.9a without using any reducing agent. The plasmon-induced grafting of aryl layers on a gold surface derived from bithienylbenzene diazonium salts on Au nanotriangles was performed under visible-light illumination in a few minutes.<sup>61</sup> The grafting process was enhanced significantly on the apex of the Au triangles and between Au nanoparticles, which is where the electric field “hot spots” (the concentrated electric fields) are located. Moreover, by controlling the polarization of incident light, the localization and anisotropic growth orientation of the deposited polyaryl layer on the nanotriangle

surface was tuned (Figure 1.9b). These results clearly demonstrate plasmon enhancement and confirm that localized surface plasmon resonance can induce localized reactions on a nanoscale.

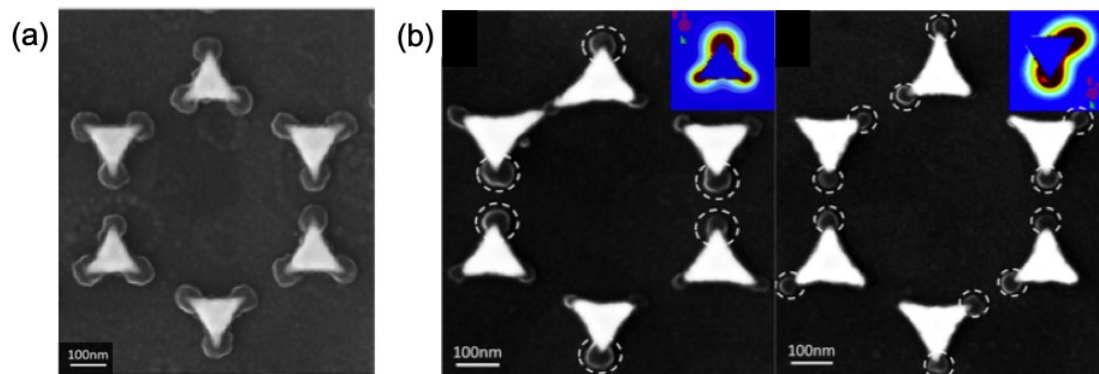


**Figure 1.9 (a) SEM image of Au triangles after 4 min of irradiation with visible light in the presence of bisthiénylbenzene diazonium salt aqueous solution. (b) Polarization-dependent plasmon-induced grafting from the diazonium solution. SEM images of Au triangles after 2 min irradiation with near-IR light. Inset is the calculated field enhancement with polarized light along the two different primary symmetry axes; the red arrows show the maximum of the electrical field. Reproduced with permission from reference 61. Copyright 2017 American Chemical Society.**

### 1.4.3 Plasmon-driven Surface Polymerization

Plasmonic nanoparticles with surface-grafted polymers have shown potential applications in many studies, from biosensor devices to drug delivery systems and environmental decontamination.<sup>62, 63</sup> As plasmon-induced surface polymerization techniques allow control of the site-selectivity and polymer growth orientation, the toolbox for polymerization and nanofabrication is expanded. For example, nitroxide-mediated polymerization (NMP) is a reversible deactivation polymerization technique (Figure 1.10). There are two requirements for this reaction: firstly, a nitroxide initiator is needed as a control reagent to generate monodisperse macromolecular architectures; secondly, the reaction occurs above 100 °C, which constitutes the main limitation of this technique. To overcome these difficulties, plasmon-mediated homolysis of alkoxyamines was proposed as an alternative by Gusel'nikova et al.<sup>64</sup> The alkoxyamine groups were attached first via Au–C bonds to gold graftings. The parameters for gold graftings (periodicity, 0.55 μm; amplitude, 27 nm; and metal thickness, 25 nm.)

provide the excitation and propagation of surface plasmon-polariton waves under illumination at 785 nm. Then, plasmon-induced homolysis and initiation of NMP were triggered by irradiation of the gold gratings with light at room temperature, and poly(*N*-isopropylacrylamide)-co-4-vinylboronic acid block copolymers (PVBA-PNIPAM) were formed (Figure 1.10). The obtained polymer-coated gold grating platforms were used as smart SERS-sensors for the detection of biologically relevant glycoprotein with high intensity.

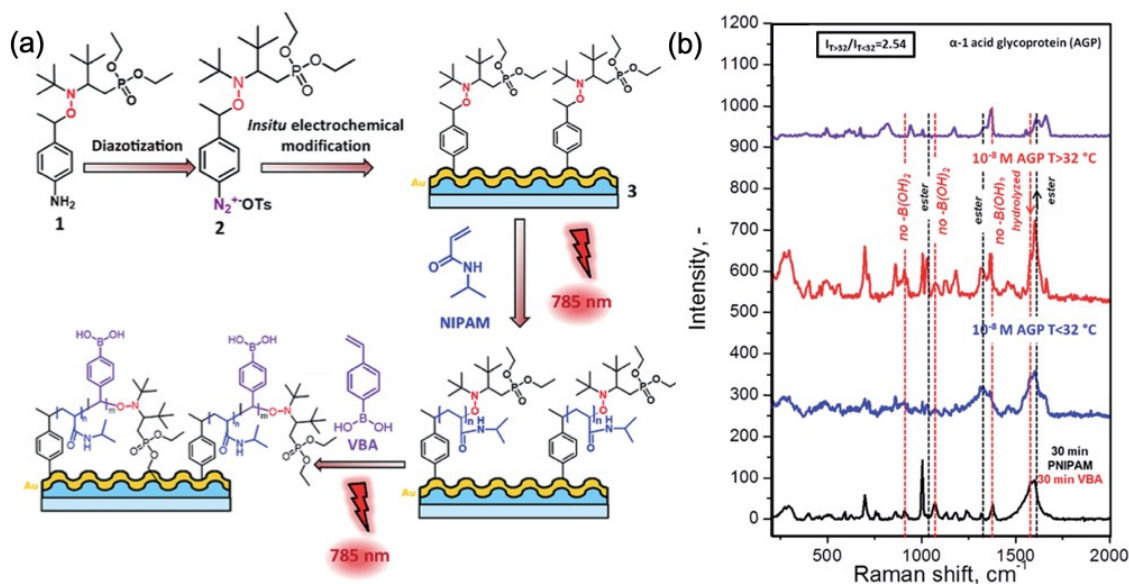


Figure 1.10 (a) The strategy for plasmon-induced surface polymerization by growing PNIPAM/PVBA brushes onto alkoxyamine initiator-grafted gold grating. (b) The surface-modified gratings with a covalently attached copolymer were used for SERS detection of glycoproteins, and the intensity of characteristic peaks increased up to 2.5-fold. Reproduced with permission from reference 64. Copyright 2019 Royal Society of Chemistry.

#### 1.4.4 Plasmon-driven Surface Chemistry for Site-selective Grafting of Nanoparticles

Nanomaterials, including gold nanoparticles<sup>65</sup> and quantum dots,<sup>66</sup> can be put into design locations with high lateral resolution. Such surface functionalization is expected to occur exclusively on highly reactive or high electromagnetic field regions (“hot spots”), while leaving the other area unmodified. In 2012, Dostert et al. reported site-selective immobilization of gold nanoparticles by plasmon-mediated surface

functionalization on a glass substrate.<sup>65</sup> The glass surface was functionalized first by a photosensitive organosilane. The field enhancement of the gold nanocrescents triggered the photocleavage of the cage, leaving free amine groups surrounding the gold nanostructures on the glass surface, which act as the binding sites for small gold nanoparticles. The scheme of this multi-step strategy is illustrated in Figure 1.11a. The resulting near-field-driven chemical nanopatterns were used to control the assembly of gold colloids, and a clear concentration of gold colloids at the tips and central back region of the gold crescent was observed that matches perfectly the near-field pattern predicted by numerical simulations based on the finite difference time domain method, as shown in the SEM image in Figure 1.11b.

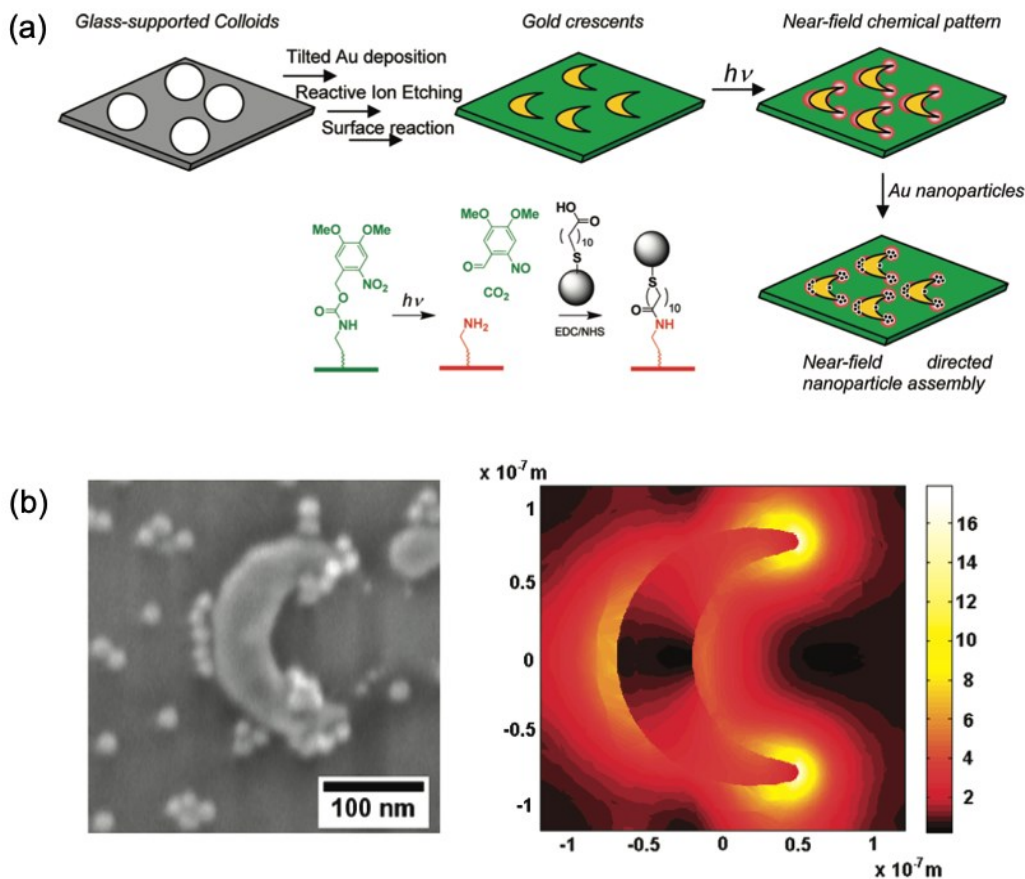
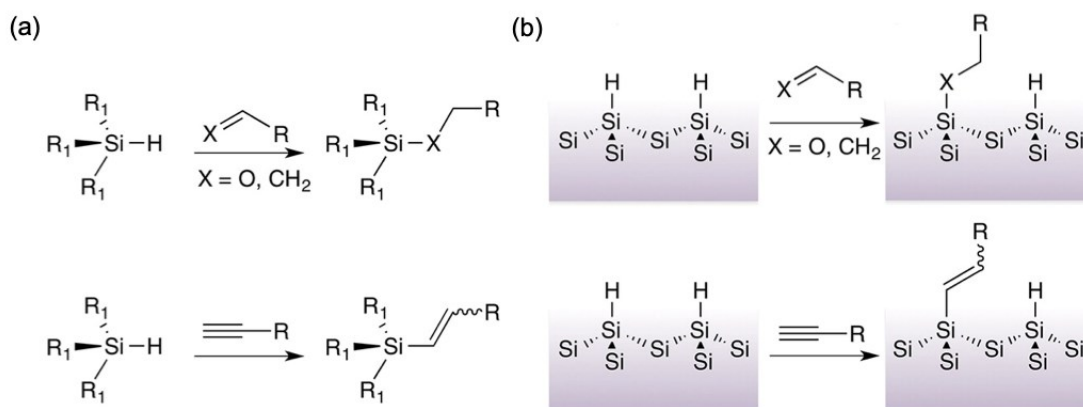


Figure 1.11 (a) Strategy to realize near-field guided chemical nanopatterning, followed by regioselective gold nanoparticle assembly. (b) SEM image of a gold crescent after this strategy, showing higher particle densities at the regions with the strongest near-field enhancement that agree well with the theoretical calculation of the intensity distribution of the field enhancement surrounding a gold nano-crescent. Reproduced with permission from reference 65. Copyright 2012 American Chemical Society.

## 1.5 Hydrosilylation on Si Surfaces

### 1.5.1 Overview

Surface functionalization with organic monolayers is used widely to stabilize the silicon surface, and the properties of silicon can be tailored precisely to endow the material with particular characteristics. Currently, there are two ways to conjugate organic monolayers onto Si surfaces: one is monolayers on native or thin silicon oxide surfaces through silane chemistry, the other is monolayers on oxide-free Si, prepared mostly via Si–C chemistry.<sup>67,68</sup> Notably, the oxide layer is not desirable because it acts as an additional insulating barrier between the organic layer and the bulk silicon. Unless grown under carefully controlled conditions, the interface between silicon and silicon oxide has a high density of electronic defects, thus limiting its property for devices.<sup>69,70</sup> For the oxide-free interfaces, H-terminated Si surfaces commonly are used as a reactive surface precursor. An H-terminated surface provides passivation of the silicon surfaces but exhibits limited chemical stability. Hydrosilylation, the addition of Si–H bonds across unsaturated bonds, has been one of the most widely studied chemistry on silicon surface modification. This reaction can be viewed as either an insertion reaction of an unsaturated bond into the Si–H bond or cleavage of the Si–H bond across the unsaturated group; examples are shown in Figure 1.12.<sup>71</sup>



**Figure 1.12** Examples of hydrosilylation of unsaturated molecules. (a) Hydrosilylation of an aldehyde, an alkene, and an alkyne with trisubstituted molecular silanes. (b) Hydrosilylation of an aldehyde, an alkene, and an alkyne on a representative silicon surface, Si(111)–H. Reproduced with permission from reference 71. Copyright 2014 American Chemical Society.

Inspired by a vast body of knowledge in analogous silicon compound reactions in solutions, Linford and Chidsey reported a Si–C bond alkyl chain on non-oxide Si(111)–H surfaces in 1993 for the first time.<sup>72, 73</sup> Since then, hydrosilylation on Si surfaces has been expanded via various pathways, including thermally induced reactions, catalyst-aided reactions, photochemically induced reactions, and electrochemically-driven reactions.<sup>68, 74–77</sup> As transition metal nanoparticles are extremely effective catalysts in the case of molecular hydrosilylation, their use in surface hydrosilylation also has been investigated. So, in the following section, I will introduce surface hydrosilylation driven by metal nanoparticles, including Pd, Pt, and Au.

### 1.5.2 Pd/Pt Catalyzed Hydrosilylation on Si Surface

In 2008, Mizuno from our group, designed a soft polydimethylsiloxane (PDMS) stamp with embedded Pd nanoparticles to catalyze hydrosilylation on H-terminated Si surfaces.<sup>78</sup> Firstly, pseudo-hexagonal close-packed Pd nanoparticle arrays were assembled on oxide-capped silicon substrates via the use of self-assembled block copolymer (polystyrene-block-poly-2-vinylpyridine; PS-*b*-P2VP) templates. Then, these nanopatterns were transferred onto PDMS via a simple peel-off procedure. Finally, the Pd catalytic stamp was inked with diluted alkenes/alkynes for 1 min and then applied to freshly prepared flat H-terminated Si(100) or Si(111) for 20 min under continuous pressure, resulting in a duplication of the original pattern of Pd nanoparticles on the silicon surface with arrays, as shown in Figure 1.13.

By modulating the molecular weight of the PS and/or P2VP blocks, nanopatterns of various metals can be synthesized with center-to-center spacings of, for instance, 50–180 nm and nanoparticle diameters of 10–70 nm.<sup>79, 80, 81</sup>

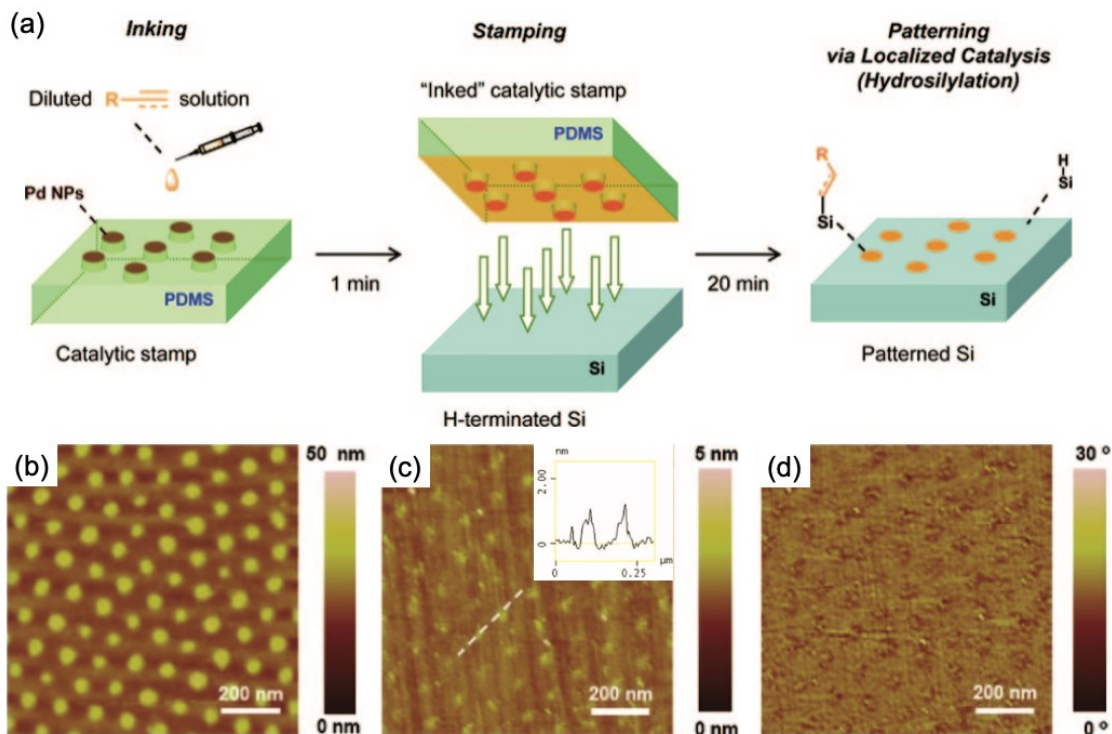


**Figure 1.13** (a) Scheme of the typical process of catalytic stamp lithography. (b) AFM height image of a parent Pd catalytic stamp. The diameter of Pd nanoparticle is 40 nm, and the center-to-center spacing is 110 nm. (c) 1-Octadecyne stamped Si(111)-H surface height image; inset image is the height profile along the dashed line and corresponding phase image (d) Reproduced with permission from reference 82. Copyright 2008 American Chemical Society.

Thereafter, by using the same fabrication strategy, PDMS stamps with hexagonally or linearly arranged Pt nanostructures were fabricated.<sup>78, 83</sup> These hybrid materials, which act as catalytic stamps, have been examined with different hydrosilylation reactions with eight kinds of molecular inks to produce the hydrosilylated alkyl, alkenyl, or alkoxy groups on H-terminated Si surfaces (Figure 1.14).

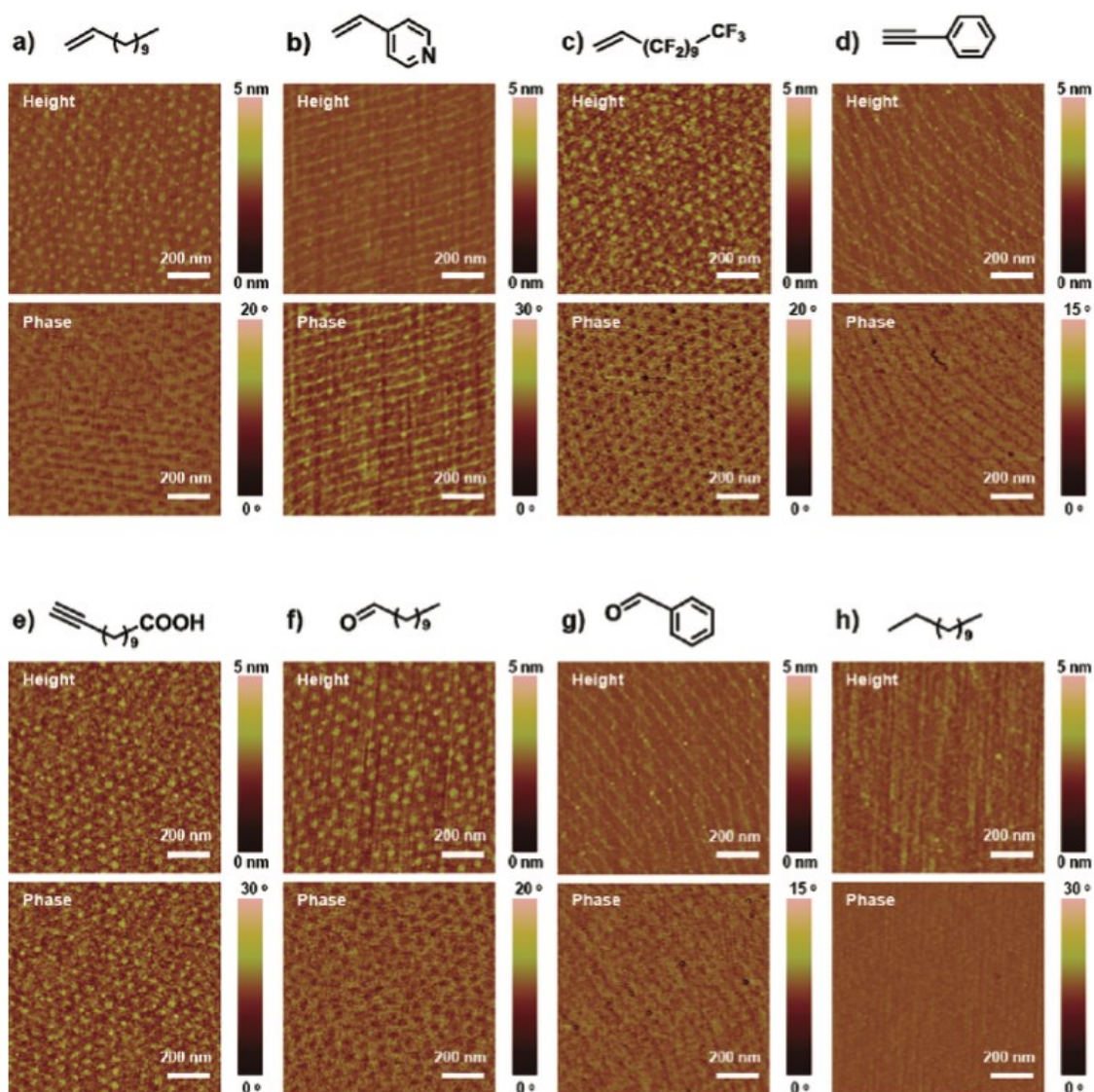


Figure 1.14 AFM height and phase images of H-terminated Si surfaces stamped with eight kinds of molecular inks: (a) Si(111)-H stamped with 1-dodecene; (b) Si(111)-H stamped with 4-vinylpyridine; (c) Si(100)-Hx stamped with 1H,1H,2H-perfluoro-1-decene; (d) Si(111)-H stamped with phenylacetylene; (e) Si(100)-Hx stamped with 10-undecynoic acid; (f) Si(111)-H stamped with undecanal; (g) Si(111)-H stamped with benzaldehyde; (h) Si(111)-H stamped with dodecane. Reproduced with permission from reference 78. Copyright 2009 American Chemical Society.

### 1.5.3 Au Plasmon-induced Hydrosilylation on Si surface

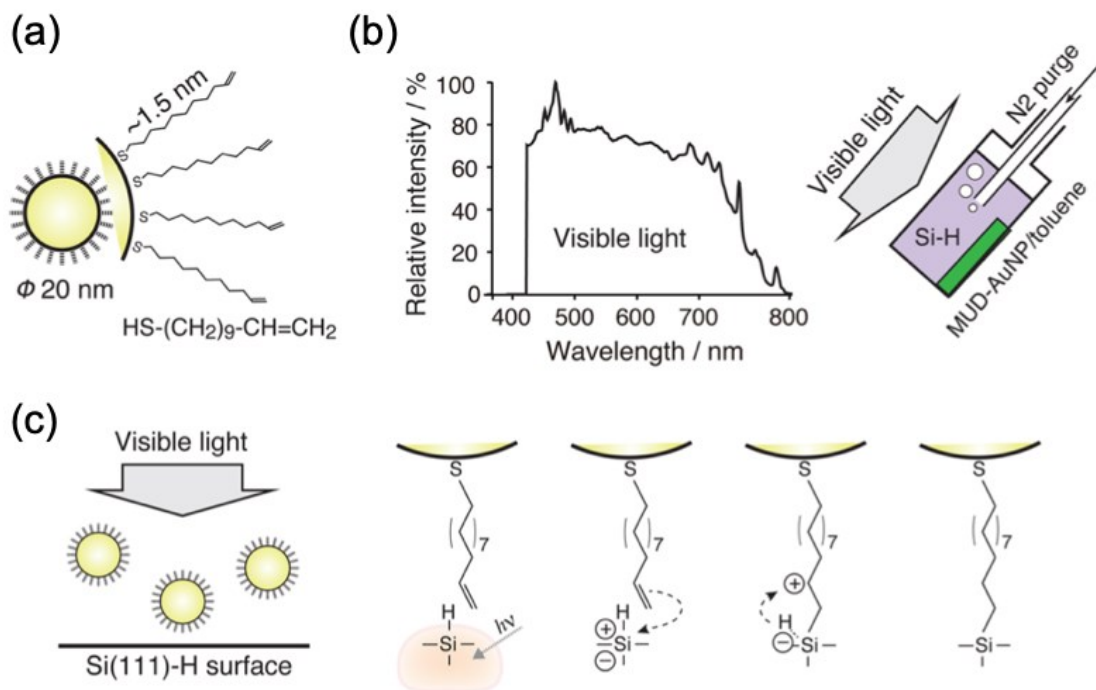


Figure 1.15 Covalent immobilization of Au nanoparticles onto a Si surface by illumination with visible light. (a) 11-Mercaptoundecene (MUD) modified Au nanoparticle. (b) Visible-light spectrum and irradiation set-up. (c) Mechanistic scheme of Si-H with MUD on Au NP. Reproduced with permission from reference 84. Copyright 2013 American Chemical Society.

In 2013, the Sugimura group reported that alkene-terminated thiols modified gold nanoparticles showed higher levels of incorporation on a flat hydride-terminated silicon surface when illuminated with light that overlapped with the absorption maximum of the gold nanoparticles.<sup>84</sup> The authors proposed that the gold nanoparticles act as “photon collectors” to transport the energy from the incident illumination to the Si surface, as suggested in Figure 1.15. The proposed “photon collector” role of the gold nanoparticles could come from either scattering of gold nanoparticles and/or the surface plasmon absorption.

Inspired by this work, Liu et al. from our group prepared gold plasmonic stamps via a similar approach to that described by Mizuno and co-workers.<sup>85, 86</sup> The plasmonic stamps were made of embedded gold nanopatterns, also produced via block copolymer self-assembly. The stamps could trigger the localized hydrosilylation of alkenes or

alkynes on a hydrogen-terminated silicon surface by illumination with visible light (Figure 1.16a). The hydrosilylation reaction was expected to proceed via the generation of a proximal electric field upon plasmon excitation in the Si surface. After plasmonic stamping, hexagonal arrays of alkyl and alkenyl patches formed on the silicon surface, mirroring the topographic features of the parent gold nanopatterns. Subsequent thiol-ene coupling with 1,6-hexanedithiol on the free terminal alkene groups, followed by electroless deposition of gold from aqueous  $\text{HAuCl}_4$  solution and ascorbic acid, allowed the clear visualization of nanopatterns (Figure 1.16b, c).

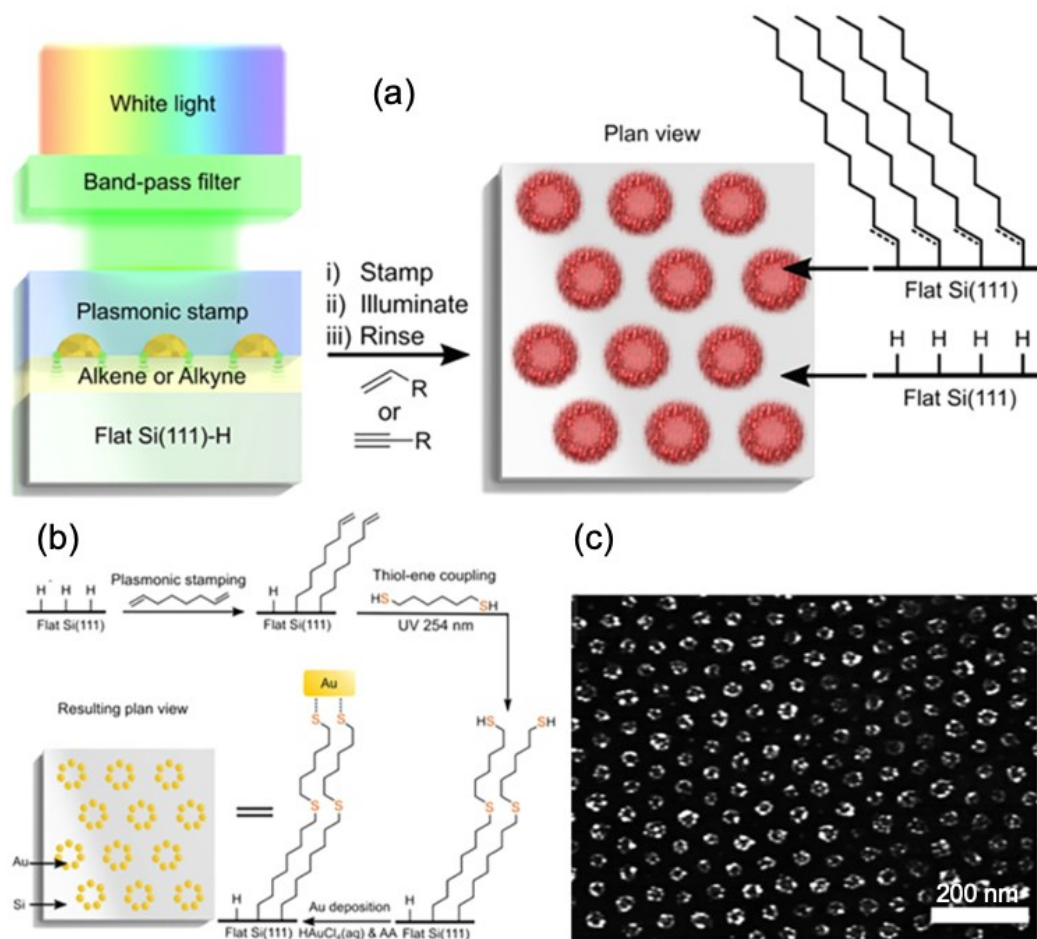


Figure 1.16 (a) Scheme of plasmon-induced hydrosilylation on a flat silicon Si(111)-H surface. White light was filtered by a green bandpass filter, then passed through the transparent PDMS stamp, allowing LSPR excitation of Au nanopatterns. After plasmonic stamping, localized hydrosilylation of alkenes or alkynes patterns occurs on Si surfaces. (b) Scheme of pattern visualization by thiol-ene coupling and electroless gold deposition. (c) SEM micrographs of the resulting gold nanopatterns. Reproduced with permission from reference 86. Copyright 2016 American Chemical Society.

The PDMS stamps with embedded nanopatterned gold hemispheroids is an alternative to photolithography of semiconductor surfaces with sub-100 nm pattern resolution. However, multiple steps are needed to make one stamp successfully, including block copolymer self-assembling, PDMS preparation, and gold pattern transfer; thus, fabricating these stamps could be challenging and time-consuming. Alternatively, solid-state dewetting of metal thin films has distinctive advantages for producing metal nanoisland arrays over a large area. The average size and separation of metal nanoislands can be moderately controlled with the initial thickness of a thin metal film. Solid films are usually metastable or unstable in the as-deposited state, and they will dewet or agglomerate to form islands when heated to sufficiently high temperatures. This process is driven by surface energy minimization and can occur via surface diffusion well below a film's melting temperature, especially when the film is very thin.<sup>110, 111</sup>

## 1.6 Scope of the Thesis

While >80% of the work described in this thesis revolves around plasmon-driven chemistry, there are, in fact, two research projects that will be covered in this thesis. The primary one is the preparation of plasmonic stamps for hydrosilylation on silicon surfaces, and it makes up the majority of the thesis, representing Chapters 2 and 3. I will discuss the topic of the surface plasmon assisted hydrosilylation, from fabricating plasmonic stamps via metal dewetting to mechanistic understanding via reaction kinetic studies. I will, however, also discuss the focus of 20% of the remaining work that was performed on the design and synthesis of Pd-Pt catalysts for wet methane combustion, which appears in Chapter 4. This chapter stands apart from Chapters 2 and 3, and thus was not introduced here in Chapter 1. It will receive its own introduction in Chapter 4.

In **Chapter 2**, a straightforward and facile method to fabricate optically transparent flexible PDMS stamps using gold dewetting is introduced. By changing the film thickness of the sputtered gold film, the size and shape of gold nanoparticles on PDMS were changed, resulting in tunable plasmonic properties. The gold nanoparticles

on plasmonic stamps can be used further to initiate hydrosilylation on a silicon surface spatially. To complement AFM imaging of the hydrosilylated silicon surfaces, galvanic displacement of gold(III) salts on the silicon was performed. The domains of hydrosilylated alkyl chains would be expected to block the deposition of gold nanoparticles.

**Chapter 3** will describe the optimization of the fabricating plasmonic stamps by tuning the sputtering rate and film thickness, leading to a more scalable and reliable method via gold dewetting on PDMS. Therefore, by using these highly reproducible PDMS stamps, systematic mechanistic studies were done. We carried out reaction kinetic studies for plasmon-induced hydrosilylation on five kinds of silicon substrates with different doping levels. As doping levels of the silicon substrates were tuned, the relationship between reaction rates and built-in electrical field of metal-insulator-semiconductor junctions were investigated.

**Chapter 4** summarizes the results of a project that provided direct support during my time here. This project was part of an NSERC Strategic Partnership Grant to support a collaboration with the group of Prof. Natalia Semagina in the Department of Chemical and Material Engineering. The project looked at the synthesis of nanoscale catalysts for methane combustion. Chapter 4 stands apart from Chapters 2 and 3 in that Pd-Pt/ZrO<sub>2</sub> catalysts were designed and synthesized for wet methane combustion.

**Chapter 5** of the thesis presents the conclusions of these two projects, along with potential research directions and perspectives for future work.

# Chapter 2 \* Fabricating Plasmonic Stamps by Gold Dewetting for Catalyzing Hydrosilylation on Silicon Surfaces

## 2.1 Introduction

Metallic gold and silver nanostructures exhibit unique optical properties resulting from the excitation of LSPR upon illumination with light. LSPR results in intense absorption bands in the optical regime and an associated enhancement of local electrical fields in close proximity to the metal surface.<sup>2,3</sup> In addition to their interesting optical properties, plasmonic nanomaterials also can accelerate reactions and phase changes of proximal reagents. For instance, illuminated silver nanoparticles yield energetic electrons that can drive the oxidation of small gaseous reagents.<sup>4</sup> Gold and other plasmonically active materials promote efficient photothermal water heating and generation of steam in bulk as well as hyperthermia in vivo.<sup>87-89</sup> Irradiation of copper surfaces during propylene epoxidation reactions can reduce inactive copper oxide surfaces back to active Cu(0) due to photoexcitation of LSPRs in the copper metal.<sup>90</sup> Hot carriers in metals also can be used to promote ammonia decomposition,<sup>1</sup> CO<sub>2</sub> reduction,<sup>6,91</sup> and other feedstocks for fuels.<sup>92,8</sup> These and a host of other reactions driven by photoexcitation of LSPRs in metallic nanomaterials point to the utility of using them as catalysts for small molecule conversion reactions.

In 2013, Sugimura and co-workers demonstrated that the LSPRs of gold nanoparticles also could be harnessed to functionalize hydride-terminated silicon surfaces. Gold nanoparticles of ~20 nm diameter, functionalized with terminal alkene groups, preferentially underwent hydrosilylation and concomitant attachment to a

---

\* The contents of this chapter have been reproduced and/or adapted from the following publication: Rao, C.; Luber, E. J.; Olsen, B. C.; Buriak, J. M. Plasmonic Stamps Fabricated by Gold Dewetting on PDMS for Catalyzing Hydrosilylation on Silicon Surfaces. *ACS Appl. Nano Mater.*, **2019**, 2, 3238–3245.

silicon surface when illuminated with light that matched the absorption maximum of the LSPR of the gold.<sup>84</sup> They proposed a mechanism that invoked a direct transfer of the energy of the photon absorbed by the LSPR to drive the hydrosilylation reaction. The wavelengths of green light centered around 520 nm normally would be of insufficient energy to promote hydrosilylation on a flat silicon surface,<sup>71</sup> pointing to the necessity of the LSPR of the nearby gold nanoparticle. In previous work, we introduced the concept of a plasmonic stamp, comprised of gold particles that had been prepared via block copolymer self-assembly, embedded within a flexible and optically transparent polydimethylsiloxane (PDMS) slab, to explore this plasmon-driven chemistry further.<sup>85, 86</sup> Using catalytic plasmonic stamps, the local electric field generated by the embedded plasmonic gold nanostructures upon illumination drives the hydrosilylation reaction on a silicon surface, leading to patterned alkyl and alkenyl termination. It was proposed that the reaction proceeded by the generation of charge carriers within the silicon, specifically, holes that accumulated at the surface. These holes were susceptible to nucleophilic attack by the alkene or alkyne, leading to the formation of Si–C bonds and alkyl/alkenyl-terminated regions on the silicon surface. Many questions regarding the mechanism remain, and to further these experiments into verifying and understanding the nuances of the plasmon-driven catalytic surface chemistry, a more practical and general approach to preparing plasmonic stamps was needed.

PDMS, coated with a metal nanostructured film, is an ideal substrate as the platform for a catalytic plasmonic stamp due to its flexibility and transparency to optical wavelengths.<sup>93–103</sup> In this work, the dewetting of gold on PDMS was examined as a facile and scalable way for producing plasmonically active gold nanostructures on the stamp. Metal dewetting has been studied well on hard inorganic substrates, such as indium tin oxide,<sup>104</sup> glass,<sup>105–107</sup> hafnium dioxide (HfO<sub>2</sub>),<sup>108</sup> and sapphire.<sup>109</sup> These studies showed that the average size and spacing of the resulting dewetted metal nanoparticles are correlated to the initial thickness of the deposited metal layer, with thicker layers leading to larger nanoparticles separated by greater center-to-center distances.<sup>110–113</sup> The deposition of thin metal films, including gold, on PDMS also has been the subject of extensive physical analysis and characterization, particularly in

regards to wrinkle formation and related patterns.<sup>114–118</sup> Combining the deposition of thin films of gold on PDMS with dewetting provides a useful starting point for the facile generation of gold nanostructure-based plasmonic stamps that can be applied to drive surface chemistry.

## 2.2 Results and Discussion

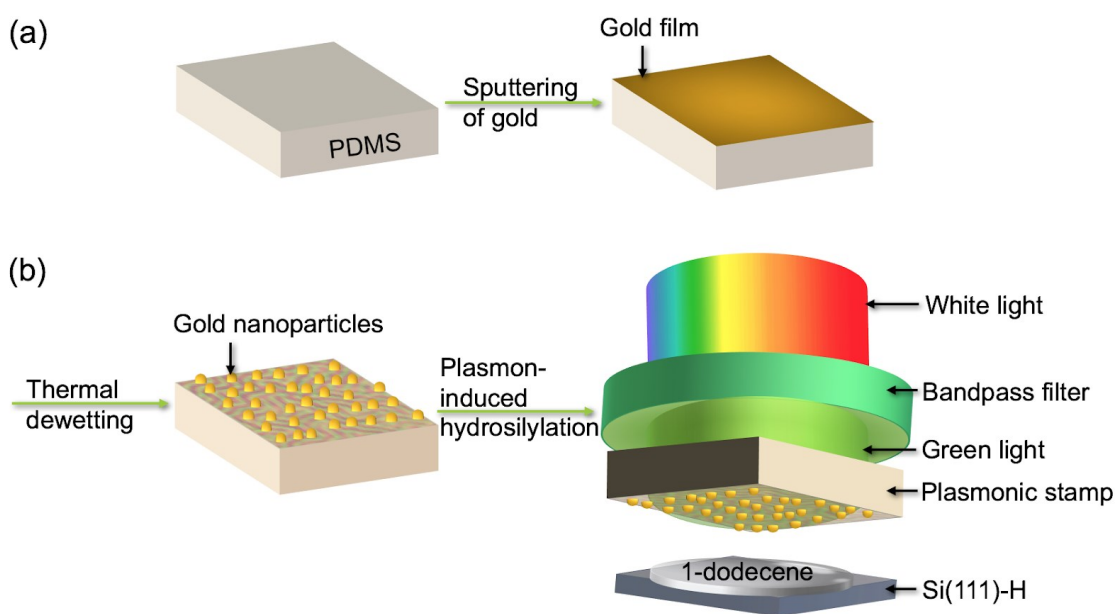


**Figure 2.1** (a) Preparation of the plasmonic stamp: a thin gold film was sputtered on top of a PDMS slab, followed by dewetting of the gold with thermal treatment. (b) Plasmonic stamping and hydrosilylation: A thin layer of 1-dodecene was layered on a flat Si(111)-H surface, and the plasmonic stamp was pressed down onto the surface. Light (400–580 nm) was shone through the plasmonic stamp for 60 minutes.

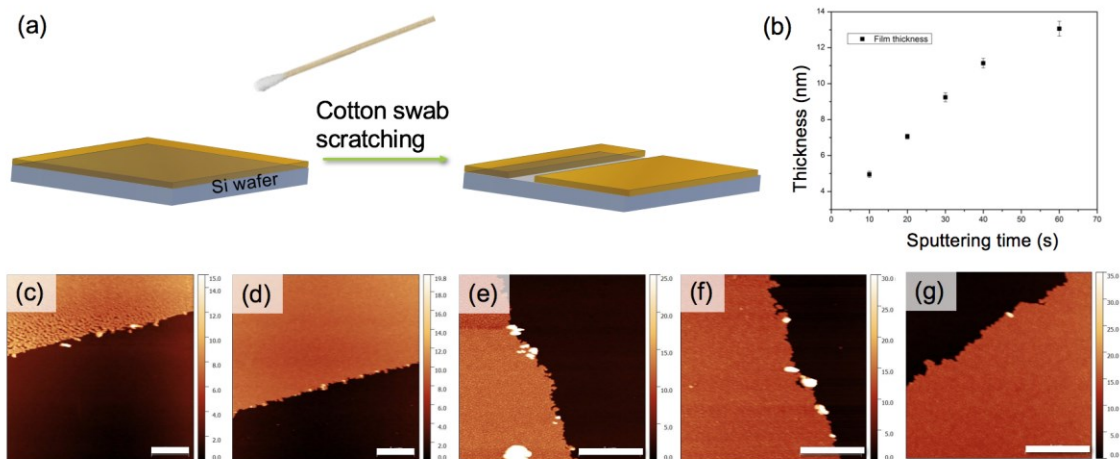


**Figure 2.2 (a)** In order to measure the gold film thickness, gold films were sputtered onto a Si wafer cleaned by a standard RCA procedure, and then a cotton swab was used to scratch a line in the gold film. AFM was used to measure the thickness of the gold. **(b)** Plot of film thickness vs sputtering time, the error bar for the gold film thickness is from one sample with multiple measurements. AFM height images of films with different sputtering times: **(c)** 10 s, **(d)** 20 s, **(e)** 30 s, **(f)** 40 s, **(g)** 60 s. All the scale bars are 1  $\mu\text{m}$ .

After sputtering, the gold films appear smooth by AFM (Figure 2.2) and blue-gray to the eye (Figure 2.3). Previous work by Graudejus and co-workers had shown that thin films of gold on PDMS appeared smooth, as defined by the absence of microcracks or buckles, below a thickness of 50 nm, when deposited at temperatures above room temperature ( $>40\text{--}80\text{ }^\circ\text{C}$ , depending upon thickness of the gold).<sup>114</sup> The gold film sputtered onto the surface of PDMS is only physisorbed as there is no covalent interaction between the two. Upon heating in air at  $150\text{ }^\circ\text{C}$  for 20 h, the gold films dewet into gold nanoparticles on the surface of the PDMS. As shown in Figure 2.3, the UV-visible absorption spectra of the smooth gold films on PDMS are broad, with maxima above 700 nm. After thermal treatment, the UV-visible spectra show a narrower absorption, with maxima varying from 535 to 625 nm, corresponding to the LSPRs of the newly formed gold nanoparticles (Figure 2.3 and Table 2.1). The corresponding colors of the PDMS stamps appear red-pink to red-brown, depending upon the initial thickness of the gold film. The dewetted gold nanoparticles on PDMS (the completed plasmonic stamps) appear to be stable for up to one month based upon a lack of any visible change of color or surface morphology.

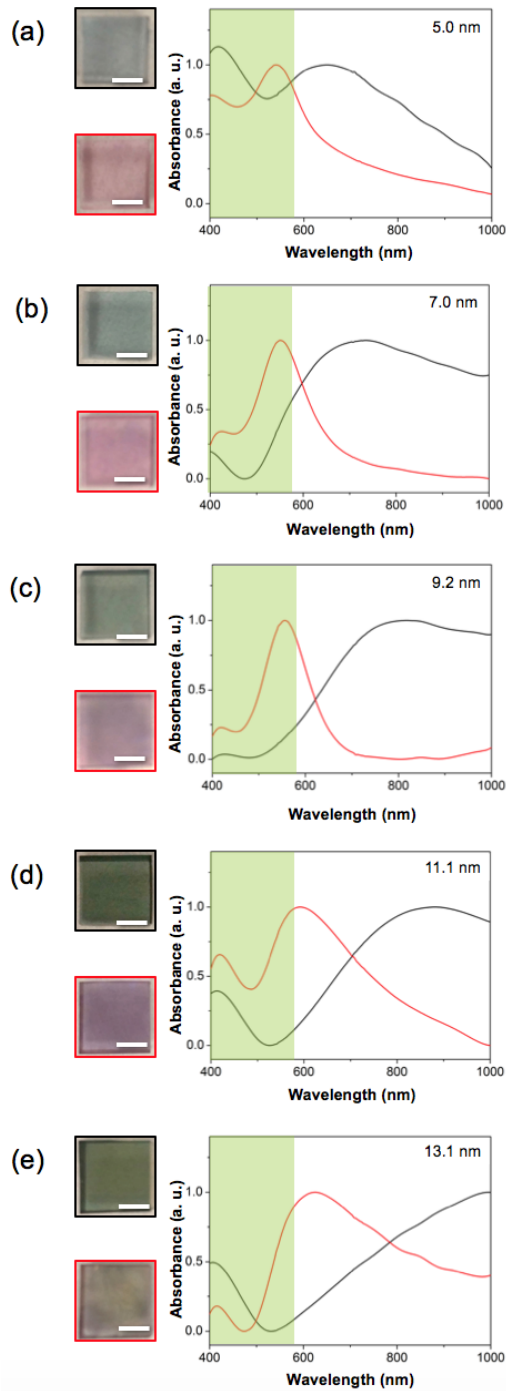


Figure 2.3 Photographs of PDMS stamps with varying initial thickness of gold: 5.0 nm (a), 7.0 nm (b), 9.2 nm (c), 11.1 nm (d), 13.1 nm (e), before (black border) and after (red border) thermal dewetting of the gold film. Corresponding UV-vis spectra are shown on the right; black plot before dewetting, and red plot post-dewetting. The green band in the UV-vis plots indicates the spectral window of light used to drive the plasmonic stamping. All the scale bars are 0.5 cm. Thickness measurements of the sputtered gold films were carried out on a native oxide-capped silicon wafer, as shown in Figure 2.2.

**Table 2.1 Deposition Parameters and Optical characteristics of Sputter-deposited Au films on PDMS.**

Sputtering time (s) <sup>a</sup>	Gold film thickness (nm)	LSPR absorption maxima after dewetting (nm)
10	5.0 ± 0.2	535
20	7.0 ± 0.1	548
30	9.2 ± 0.3	556
40	11.1 ± 0.2	592
60	13.1 ± 0.4	625

<sup>a</sup>Sputtering time, as-deposited gold film thickness and LSPR wavelength.

Optical micrographs (1000× magnification) of the PDMS samples before and after dewetting of the sputtered gold films are shown in Figure 2.4a and Figure 2.4b, respectively, and low-magnification AFM micrographs after dewetting are shown in Figure 2.5. After dewetting of Au films on PDMS substrates, the substrates adopted a wrinkle morphology, which commonly is observed in layered PDMS samples subject to strain.<sup>119–123</sup> Wrinkling of the PDMS was not observed upon thermal treatment in the absence of a gold film (Figure 2.6), nor was it observed after sputtering of the gold film (Figure 2.7), which suggests that the wrinkling of the PDMS substrate is due to the interfacial stresses that occur during dewetting.

AFM images of the dewetted gold-on-PDMS samples (Figure 2.4c) show that when the as-deposited thickness of the sputtered gold film increases, the resulting size of the dewetted gold nanoparticles also appears to increase, which agrees with the expected LSPR red-shift of larger gold nanoparticles,<sup>124</sup> as seen in our measured absorption spectra in Figure 2.3 and Table 2.1. Moreover, as seen in the AFM micrographs of the three thinnest films (5.0, 7.0, and 9.2 nm), the dewetted particles appear to be mostly uniform in size and shape, possessing aspect ratios close to unity. However, the morphology of the dewetted 11.1 nm thick film clearly shows a much broader distribution of particle sizes and a large fraction of particles with aspect ratios significantly larger than unity and possessing irregular shapes. This symmetry breaking of particle shapes is expected to give rise to additional LSPR modes at longer wavelengths,<sup>125</sup> which is seen clearly in the UV-vis spectra in Figure 2.3.

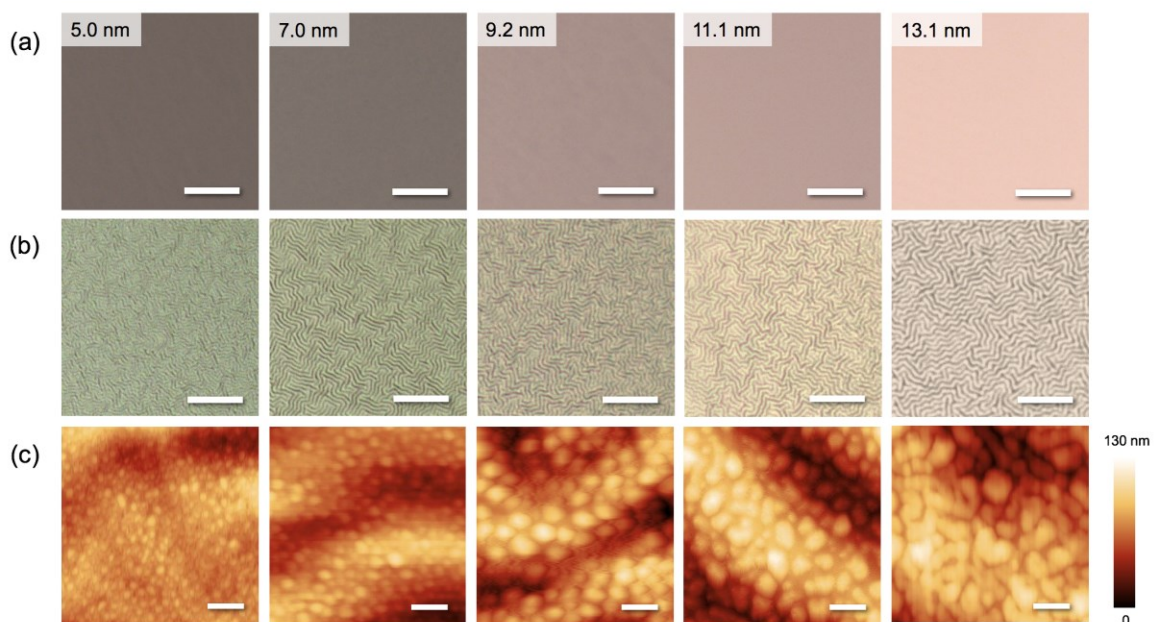


**Figure 2.4** Optical microscope images ( $1000\times$  magnification) of gold films on PDMS surfaces, (a) before and (b) after gold dewetting. From left to right, initial gold film thickness increased from 5.0 nm to 13.1 nm. All scale bars are  $10\ \mu\text{m}$ . (c) AFM height images of dewetted gold films on PDMS, with different initial thicknesses of gold. All scale bars are 200 nm.

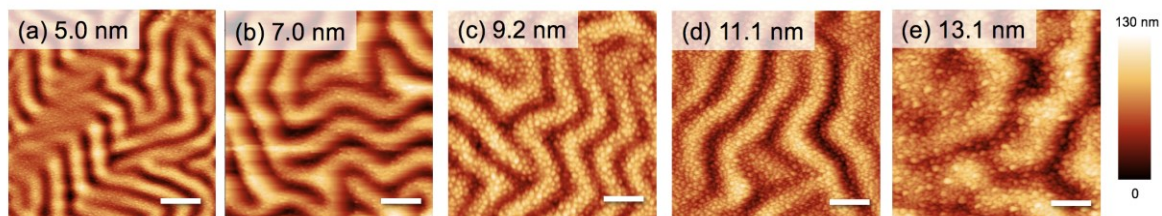


**Figure 2.5** (a) - (e) AFM images of plasmonic stamps fabricated from dewetted Au films on PDMS with as-deposited thicknesses ranging from 5.0 to 13.1 nm. All scale bars are  $1\ \mu\text{m}$ .

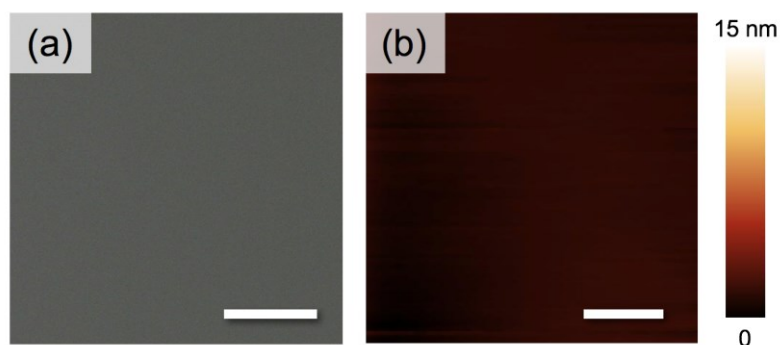


**Figure 2.6** Blank PDMS, heated at 150 °C for 20 h. (a) Optical microscope images (1000× magnification) to show the morphology of the PDMS; scale bar = 10 μm. (b) Corresponding AFM height image. No wrinkles are observed with heating only; scale bar = 500 nm.

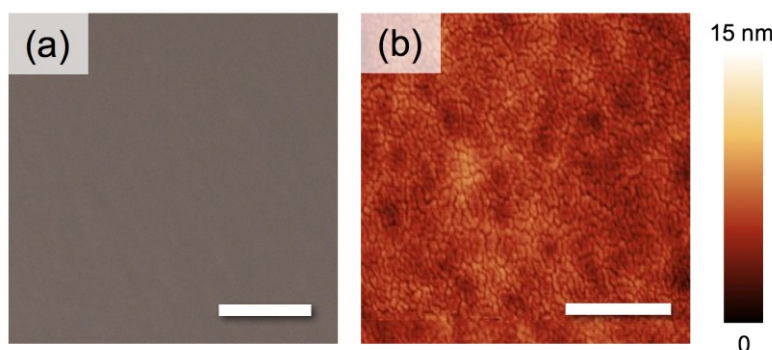


**Figure 2.7** As-sputtered 5.0 nm-thick gold on PDMS before heating. (a) Optical microscope images (1000× magnification) to show the morphology of the PDMS; scale bar = 10 μm. (b) Corresponding AFM height image. No wrinkles are observed with gold sputtering only; scale bar = 500 nm.

A scheme illustrating the mechanism of how plasmonic stamping can be used to carry out hydrosilylation on a silicon surface is shown in Figure 2.8. The proposed mechanism in Figure 2.8 is based upon earlier published work by our group, which had shown the necessity of illumination, the role of doping of the underlying silicon, and other important factors that underline the critical role of the LSPR.<sup>85, 86</sup> These two earlier studies also had examined the LSPR-driven chemistry of both alkenes and alkynes and used atomic labels (fluorine, sulfur) to substantiate the claim of hydrosilylation and Si–C bond formation by XPS, static water contact angle measurements, and detailed AFM imaging. This present work, therefore, builds upon this earlier work and focuses most heavily on water contact angle measurements to reveal the extent of hydrosilylation as promoted by these plasmonic stamps. Light

(400–580 nm), which matches the LSPR absorbance of the nanoparticles of gold on the plasmonic stamp, induces a local electric field (E-field). A built-in metal-insulator-semiconductor (MIS) junction is established, with the 1-dodecene layer acting as the insulator. Electron-hole pairs are generated from the intense LSPR E-field, and these holes are then swept to the Si-H interface due to the built-in field of the depletion region from the MIS junction, which results in nucleophilic attack by the alkene and Si–C bond formation. As shown in earlier work, the thickness of the 1-dodecene “ink” layer is ~5 nm, which is thin enough to enable the electric field of the LSPR to generate the electron-hole pairs in the silicon.<sup>86</sup> Static water contact angle measurements of the starting and reacted Si(111)-H surfaces are summarized in Figure 2.9 and Table 2.2 and include critical control experiments to elucidate the important factor(s) that lead to an increase in hydrophobicity, which occurs upon hydrosilylation with 1-dodecene. The starting static water contact angle of a freshly etched Si(111)–H surface is ~83°. Blank PDMS stamps and PDMS with non-dewet films of gold do not induce hydrosilylation among others, as evidenced by the lack of change of contact angle. Only the combination of illumination and a 5.0–9.2 nm-thick (as-deposited) dewetted films of gold on PDMS resulted in a significant increase of water contact angle to ~98°. The two thicker gold films, with initial thicknesses of 11.1 nm and 13.1 nm, resulted in lower water contact angles of ~91° and ~88°, respectively. It should be noted that the ‘highest’ water contact angle of ~98° is less than would be expected for a complete, smooth, and uninterrupted monolayer due to the patchy nature of the plasmonic stamp-induced patterning.

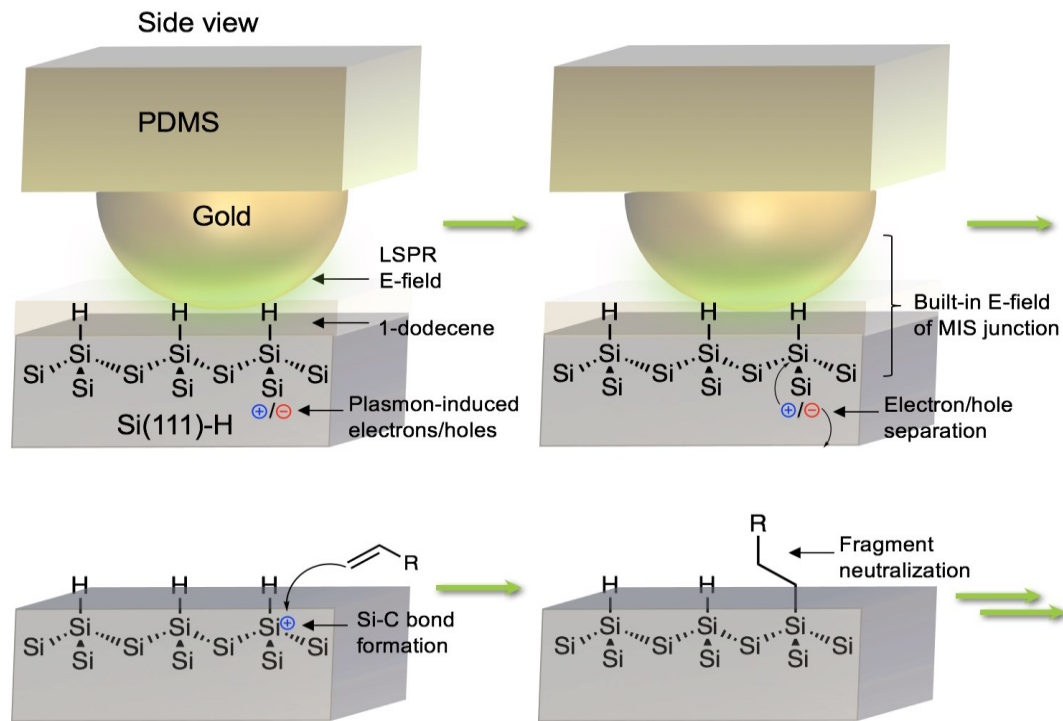


**Figure 2.8 Mechanism for plasmonic stamp-induced hydrosilylation on a flat Si(111)-H surface. The built-in electric field of the LSPR results in electron-hole pair formation in the silicon, triggering the mechanism for hydrosilylation.  $R = -(CH_2)_9CH_3$ .**

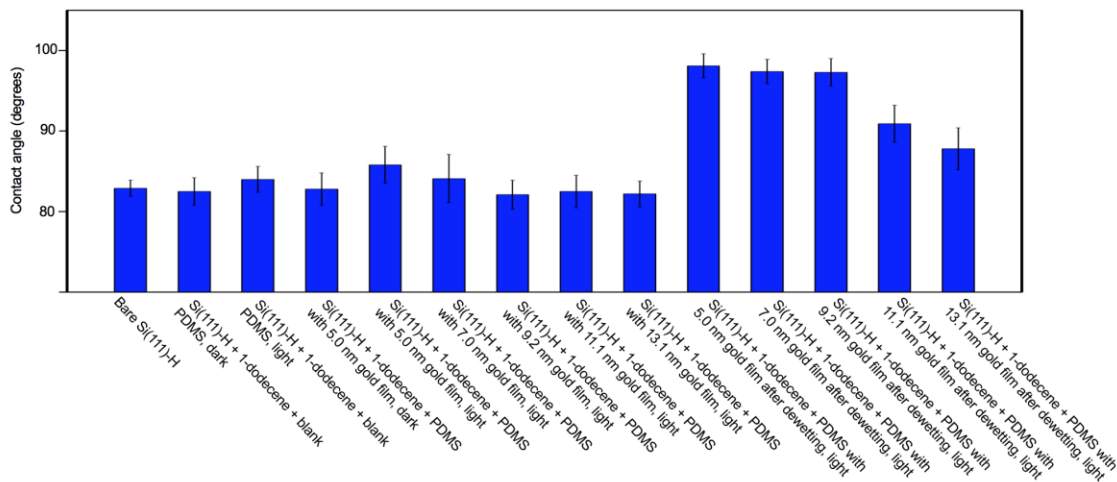


**Figure 2.9 Summary of the measured values of static water contact angles of Si(111)-H surfaces under various conditions, including control experiments. Detailed statistics and errors are found in Table 2.2.**

**Table 2.2 Summary of Static Water Contact Angle.**

Samples	Illumination condition <sup>a</sup>	Contact angle (°) <sup>b</sup>
Si(111)-H	Dark	82.9 ± 1.0
Si(111)-H + 1-dodecene + blank PDMS	Dark	82.5 ± 1.7
Si(111)-H + 1-dodecene + blank PDMS	Light	84.0 ± 1.6
Si(111)-H + 1-dodecene + PDMS with 5.0 nm gold film	Dark	82.8 ± 2.0
Si(111)-H + 1-dodecene + PDMS with 5.0 nm gold film	Light	85.8 ± 2.3
Si(111)-H + 1-dodecene + PDMS with 7.0 nm gold film	Light	84.1 ± 3.0
Si(111)-H + 1-dodecene + PDMS with 9.2 nm gold film	Light	82.1 ± 1.8
Si(111)-H + 1-dodecene + PDMS with 11.1 nm gold film	Light	82.5 ± 2.0
Si(111)-H + 1-dodecene + PDMS with 13.1 nm gold film	Light	82.2 ± 1.6
Si(111)-H + 1-dodecene + PDMS with 5.0 nm gold film after dewetting	Light	98.1 ± 1.5
Si(111)-H + 1-dodecene + PDMS with 7.0 nm gold film after dewetting	Light	97.4 ± 1.5
Si(111)-H + 1-dodecene + PDMS with 9.2 nm gold film after dewetting	Light	97.3 ± 1.7
Si(111)-H + 1-dodecene + PDMS with 11.1 nm gold film after dewetting	Light	90.9 ± 2.3
Si(111)-H + 1-dodecene + PDMS with 13.1 nm gold film after dewetting	Light	87.8 ± 2.6

<sup>a</sup>The contact measurement data of the Si(111)-H surface after hydrosilylation with 1-dodecene under various conditions are listed. For each condition, at least 10 measurements were collected. <sup>b</sup>Measurements the uncertainty given is the standard deviation of these measurements.

As seen from the AFM micrographs of the plasmonic stamps, for the initial thicker Au films that result in larger gold nanoparticles (Figure 2.4c), there is an increased fraction of gold nanoparticles with irregular non-circular shapes and aspect ratios greater than unity. The result is a larger fraction of stamping surface requiring longer wavelength light to drive the localized surface plasmon resonance (Figure 2.3). Given that the light used to drive the plasmonic stamping is limited to wavelengths shorter than ~580 nm, particles with LSPR modes greater than ~580 nm will not

hydrosilylate the silicon surface underneath. As such, the plasmonic stamps possessing a significant fraction of these longer wavelength LSPR modes (11.1 and 13.1 nm) would be expected to have lower static water contact angles due to the lower coverage of dodecyl groups on the surface. This result points to the necessity of the LSPR in driving this chemistry on the silicon surface.

AFM images of the silicon surfaces that were stamped using the three plasmonic stamps with dewet films of gold with as-deposited thicknesses of 5.0 nm, 7.0 nm, and 9.2 nm on PDMS are shown in Figure 2.10. The terraces of silicon ( $\sim 3.0$  Å in height), which are due to miscutting of the Si(111) wafer, can be seen clearly in Figure 2.10a. Upon hydrosilylation with the plasmonic stamps, the terraces vanish, presumably due to coverage with flexible 1-dodecyl chains. Insets of the corresponding static water contact angle measurements are included, showing the increase from  $83^\circ$  for the Si(111)-H, to  $\sim 98^\circ$  for the hydrosilylated surfaces. The small gold nanoparticles (5.0 nm as-deposited gold film thickness) led to small spots on the silicon surface, and larger gold particles (7.0 and 9.2 nm as-deposited gold film thicknesses) appeared to produce correspondingly larger features on the silicon, but imaging these very thin and soft features by AFM is difficult due to their mechanically compliant nature. The wrinkle pattern of the original PDMS stamp does not appear to have been transferred to the silicon surface in the form of non-hydrosilylated regions on the surface; most likely, the applied pressure compresses the plasmonic stamps on the hard surface, leading to mostly uniform contact by the stamp. The plasmonic stamps can be used for at least three times, which is similar to the previous results.<sup>86</sup>

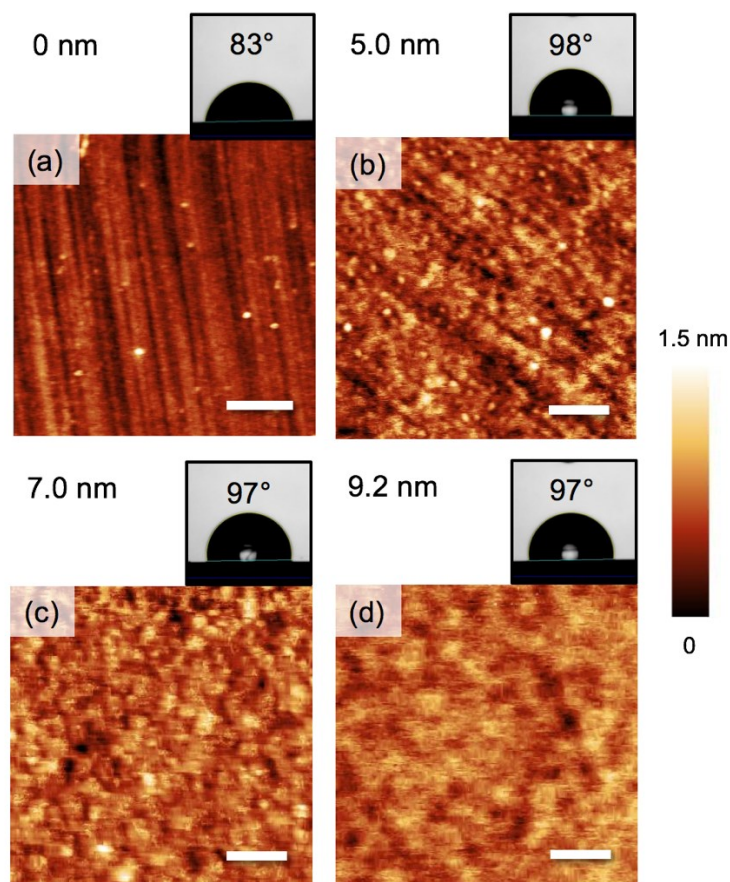


**Figure 2.10** AFM height maps and static water contact angles of Si(111)-H surfaces reacted with 1-dodecene under illumination with light (400–580 nm) using plasmonic stamps with different thicknesses of as-sputtered gold films: 0 nm (a), 5.0 nm (b), 7.1 nm (c) and 9.2 nm (d). All scale bars are 200 nm.

In order to assist in the visualization of possible domains of grafted alkyl chains that would have been formed in close proximity to the nanoparticles on the PDMS stamp, the silicon samples were treated with aqueous  $\text{KAuCl}_4$  and HF to promote galvanic displacement of gold (Figure 2.11a). Au(III) salts deposit on exposed silicon surfaces in the presence of HF (aq) via reduction with electrons derived from the silicon wafer itself.<sup>126–129</sup> Areas that are protected with alkyl chains, however, would be expected to prevent gold deposition. Si(111)-H surfaces that underwent hydrosilylation via plasmonic stamping with 1-dodecene were immersed in aqueous 1 mM  $\text{KAuCl}_4$ /1% HF for 5 min. SEM images (Figure 2.11b–d) show dark circular regions surrounded by bright deposited gold nanoparticles, which only occur on the areas that are not protected

by 1-dodecene. These dark regions increase in size with the size of the gold nanoparticles on the PDMS stamp. AFM height mapping (Figure 2.12) shows a similar morphology where the circular regions are lower in height, which further confirms that the dark circular regions in SEM correspond to silicon protected by 1-dodecene. Control experiments on unpatterned silicon surfaces are shown in Figure 2.13.

Because of AFM tip convolution effects, the actual feature sizes are not exactly as they appear, although the centre-to-centre spacing should be accurate. In order to assist in the visualization of grafted alkyl chains that would have been formed in close proximity to the nanoparticles, galvanic displacement was used as an imaging fiduciary, and qualitatively, we can conclude that, the spacing of the empty spots surrounded by gold nanoparticles (presumably patches of 1-dodecyl groups that prevent galvanic displacement) is similar to the spacing of gold nanoparticles on the PDMS stamp.

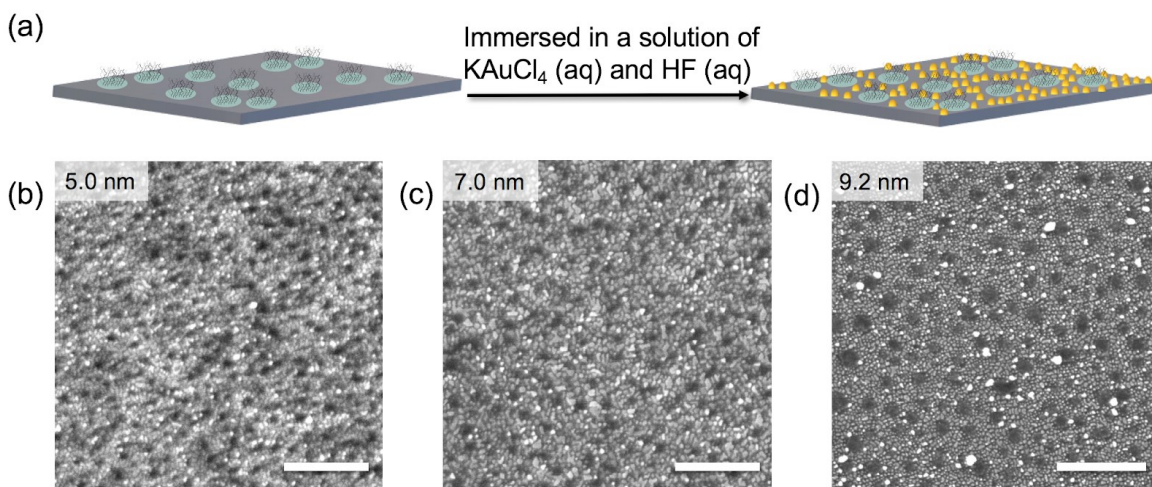


**Figure 2.11 Hydrosilylation visualization using gold nanoparticle deposition. (a) Schematic outline of galvanic displacement with aqueous  $\text{KAuCl}_4$  and  $\text{HF}$ : hydrosilylated regions prevent galvanic displacement of metallic gold, thus enabling their visualization as dark, unreacted regions. (b-d) Silicon surfaces that have been hydrosilylated with plasmonic stamps of different initial thickness of gold films (5.0 nm, 7.0 nm and 9.2 nm). All the scale bars are 200 nm.**

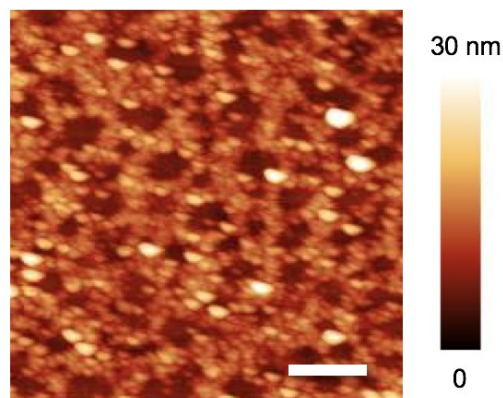


Figure 2.12 AFM image of the Si(111)–H sample after (i) hydrosilylation using a plasmonic stamp with a sputtered gold film thickness of 9.2 nm, and (ii) galvanic displacement with the aqueous  $\text{KAuCl}_4$  and HF solution indicated in Figure S9; scale bar = 200 nm.

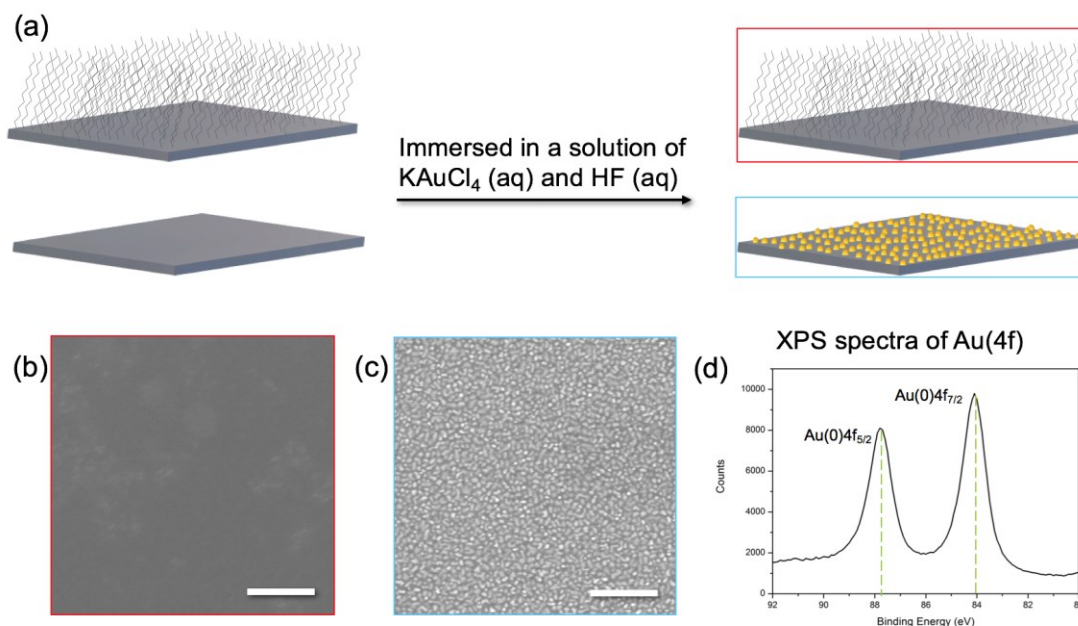


Figure 2.13 Method for visualization of hydrosilylation using gold nanoparticle fiducials. (a) Schematic outline of gold deposition via galvanic displacement. (b+c) SEM micrograph of two different silicon surfaces: (b) The Si(111)–H surface was functionalized with a monolayer of 1-dodecene by thermal-induced hydrosilylation (150 °C, 24 h), followed by exposure to an aqueous 1 mM  $\text{KAuCl}_4$  and 1% HF mixture for 5 min at room temperature in air. The SEM image shows no gold deposited onto the Si wafer (image with red border). (c) Immersing a freshly etched sample of Si(111)–H into the same aqueous  $\text{KAuCl}_4$  and HF mixture solution directly resulted in gold deposition via galvanic displacement on the silicon surface (image with blue border). (d) XPS spectra of Au(4f) of the Si(111)–H treated wafer upon galvanic displacement confirms the presence of Au(0); SEM scale bar = 200 nm.

## 2.3 Conclusions

Plasmonic stamps were prepared by a straightforward gold deposition on PDMS and dewetting procedure in order to access stamps with tunable plasmonic properties. The localized surface plasmons of the gold particles generate a proximal electric field in the underlying silicon, leading to production of charge carriers that drive surface hydrosilylation. Because the plasmonic stamps are removable, they provide a means to access mechanisms that are influenced by the electronic effects on a surface, on demand. Other reactions on semiconductors that could be driven by charge carriers can be studied using these plasmonic stamps.

## 2.4 Experimental Section

### 2.4.1 Materials

Si wafers (111-oriented, p-type, B-doped,  $\rho = 1\text{--}10 \text{ } \Omega \text{ cm}$ , thickness =  $525 \pm 25 \text{ } \mu\text{m}$ ) were purchased from WRS Materials Inc. Millipore water (resistivity of  $18.2 \text{ M}\Omega\cdot\text{cm}$ ) was used for the preparation of all aqueous solutions. The precursors for Sylgard 184 PDMS were purchased from Dow Corning.  $\text{NH}_4\text{OH}$  (aqueous, 30%) and  $\text{HCl}$  (aqueous, 37%) were purchased from Caledon Laboratories, Ltd.  $\text{H}_2\text{O}_2$  (aqueous, 30%) was obtained from Sigma-Aldrich.  $\text{NH}_4\text{F}$  (aqueous, 40%, semiconductor grade) was purchased from Transene Company, Inc.  $\text{KAuCl}_4\cdot x\text{H}_2\text{O}$  (99.999%) was obtained from Sigma-Aldrich. 1-Dodecene from Sigma-Aldrich was passed through a short column of hot alumina (dried at  $100 \text{ } ^\circ\text{C}$  for over 24 h and used while still hot) to remove water residues and peroxides, then deoxygenated with nitrogen gas. The optical filter [CW526 (center band wavelength) of 526 nm; full width at half-maximum (fwhm) of 180 nm] was purchased from Edmund Optics Inc (see Figure 2.14 for transmission spectrum).

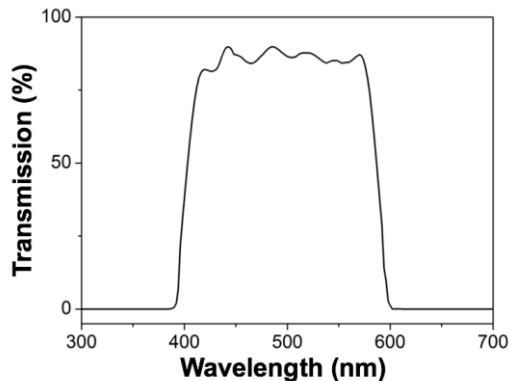


**Figure 2.14** Transmission spectrum of the band-pass filter used for plasmonic stamping (CW 526 nm, fwhm: 180 nm, Edmund Optics Inc.).

## 2.4.2 Characterization

Optical microscopy images were performed using a Zeiss Axio Lab A1 optical microscope. UV-vis absorption spectroscopy measurements were carried out in air using an Agilent UV-8453 spectrophotometer at 1 nm resolution. A baseline correction procedure (through a blank PDMS stamp) was implemented prior to measurement. Scanning electron microscopy (SEM) images were obtained with a field emission scanning electron microscope (S-4800, Hitachi), with a working pressure of  $<10^{-8}$  Torr. Tapping mode atomic force microscopy (AFM) micrographs were captured using a Digital Instruments/Veeco Nanoscope IV with silicon PPP-NCHR cantilevers purchased from Nanosensors (thickness 4  $\mu\text{m}$ , length 125  $\mu\text{m}$ , width 30  $\mu\text{m}$ , n-type Si with an Al coating, resonance frequency of 330 kHz, force constant of 10–130 N/m, tip height of 10  $\mu\text{m}$ , and tip radius of  $<10$  nm.). Sessile drop contact angles of the functionalized silicon surfaces were measured using 3  $\mu\text{L}$  of water on a Rame-Hart Model 100-00 contact-angle goniometer after the droplet on the sample surface reached a static state. X-ray photoelectron spectroscopy (XPS) spectra were taken on a Kratos Axis Ultra X-ray photoelectron spectroscopy system using an Al source with an energy of 1487 eV, in the University of Alberta nanoFAB, with binding energies calibrated to C(1s) (285.0 eV).

### **2.4.3 Blank PDMS Stamp Preparation**

The soft substrates used in our experiment were polydimethylsiloxane (PDMS). PDMS prepolymer and the curing agent (Sylgard 184, Dow Corning) were mixed in a 10:1 ratio and degassed by applying a vacuum to the prepolymer three times at room temperature. Then, ~10 mL of the mixtures was added to a petri dish (polystyrene, diameter 100 mm), with a PDMS layer thickness of ~3 mm, and cured at 65 °C for at least 6 h in an oven and then naturally in air. The cured PDMS was removed slowly and carefully from the petri dish, cleaned with Soxhlet extraction in hexane for 6 h in order to remove low molecular weight PDMS, and rinsed with ethanol and water. The blank PDMS was cut into  $1 \times 1 \text{ cm}^2$  squares and stored under vacuum for further use.

### **2.4.4 Preparation of Plasmonic Stamps**

A Denton desk II sputter coater was used to deposit the gold films onto the square blank PDMS sample at room temperature. This system uses a direct current power source to form the plasma. The target (diameter ~60 mm)-substrate distance was ~50 mm. The working argon gas (99.99% purity) pressure was 50 mTorr. The sputtering current was fixed to 20 mA. The deposition time was controlled precisely, ranging from 10 to 60 s. Because PDMS is soft, measurement of the thickness of the gold films was difficult; to solve this issue, gold films were sputtered simultaneously onto native oxide-capped silicon wafers. Film thicknesses were determined by gently wiping off an area of the gold with a cotton swab, and the thickness difference measured by tapping mode AFM (Figure 2.2). Given that the surface of native oxidize-capped silicon wafers and PDMS are chemically similar, it is reasonable to assume that the sputter-deposited gold would have essentially the same sticking coefficient on both surfaces. Even if there are small differences in sticking coefficients, there will only be a small systematic offset in the absolute values of the reported as-deposited thicknesses of these smooth films. As such, the relative differences in gold film thickness would be expected to be the same for native oxide-coated silicon or PDMS substrates. Given that the absolute thicknesses of the gold films on PDMS are not used to predict or explain any of our observations but rather the relative differences (e.g., thicker or thinner) and the similar sticking

coefficients for gold on PDMS or native silicon oxide, the reported gold film thicknesses are almost certainly sufficiently accurate and precise as given.

Thermal treatment of the deposited thin gold films on PDMS substrates to induce dewetting was carried out in air, heating at 150 °C for 20 h in an oven, and then allowed to cool to room temperature.

#### **2.4.5 Silicon Wafer Cleaning and Preparation**

Silicon wafers were cut into  $1 \times 1 \text{ cm}^2$  squares using a dicing saw (Disco DAD 321). After being sonicated in 2-propanol for 15 min and dried with a nitrogen gas stream, each chip underwent a standard RCA cleaning procedure: the chips were immersed first in a base solution [ $\text{H}_2\text{O}/30\% \text{NH}_4\text{OH} (\text{aq})/30\% \text{H}_2\text{O}_2 (\text{aq}) (6:1:1)$ ] at 80 °C for 15 min, rinsed with water, and then immersed in an acid solution [ $\text{H}_2\text{O}/37\% \text{HCl} (\text{aq})/30\% \text{H}_2\text{O}_2 (\text{aq}) (5:1:1)$ ] at 80 °C for another 15 min. The chips were rinsed with water and dried in a stream of nitrogen gas.

#### **2.4.6 Plasmonic Stamping on Hydride-Terminated Silicon Surfaces**

The cleaned silicon chips were immersed in degassed 40%  $\text{NH}_4\text{F}$  for 5 min (caution: this solution is highly corrosive and toxic; handle it with care) and then immersed into deoxygenated water for 10 s. After being dried with an argon stream, each chip was transferred immediately into a nitrogen-filled glovebox ( $\text{O}_2$  and  $\text{H}_2\text{O} < 1 \text{ ppm}$ ) and placed into a customized sample holder (Figure 2.15). Typically, neat alkene (30  $\mu\text{L}$ ) was dropped onto the hydride-terminated Si(111) surface and covered quickly by the plasmonic stamp with the side containing the gold nanoparticles facing the Si surface. Following this, a quartz slip was placed on top of the plasmonic stamp. To apply reproducible pressure, two bulldog clamps were applied on both sides to fix the sandwich structure, as shown in Figure 2.15. White light (150 W ELH bulb) was focused through a periscope convex (PCX) lens, filtered through a bandpass filter (CW526), and shone onto the sandwiched sample for 60 min with an incident intensity of 50  $\text{mW}/\text{cm}^2$ . After the plasmonic stamping steps, the wafer was rinsed with dichloromethane and dried with a stream of argon gas.



**Figure 2.15** Photograph of a customized experimental setup for plasmonic stamping: a silicon wafer was stamped with a plasmonic stamp and sandwiched between a quartz coverslip and a customized reaction holder, which was made of polytetrafluoroethylene (PTFE). Two clips were applied on both sides of the sandwich structure.

### **2.4.7 Gold Deposition on Silicon via Galvanic Displacement**

After stamping, the silicon wafer was immersed in the aqueous gold salt and hydrofluoric acid solution in a Polytetrafluoroethylene (PTFE) beaker for 5 min. The gold salt/acid solutions were prepared by mixing 0.1 mL of 0.01 M  $\text{KAuCl}_4 \cdot x\text{H}_2\text{O}$  and 9.9 mL of 1% HF (aq) (caution: this solution is highly corrosive and toxic; handle it with care). After gold deposition, the sample was thoroughly rinsed with water and dried under a stream of nitrogen gas.

# Chapter 3 Mechanistic Investigation of Plasmon-induced Hydrosilylation on Si Surfaces by Kinetic Studies

## 3.1 Introduction

Light energy is converted to chemical energy by plasmonic nanostructures, which provide tunable optical properties that can drive chemical reactions.<sup>4, 24, 37</sup> The combination of plasmonics and surface chemistry is an emerging research area,<sup>59</sup> with a wide range of promising applications, including sensing, photovoltaics, catalysis, imaging, and nanomedicine.<sup>130–133</sup>

Silicon, as the second most abundant element after oxygen on the earth's crust, is the cornerstone of the semiconductor industry.<sup>134</sup> The functionalization of silicon surfaces to tailor the physical and chemical properties is of great importance; which it widens the range of applications, including silicon-based devices for sensing,<sup>135, 136</sup> solar energy conversion,<sup>137</sup> electronic properties modulation,<sup>138, 139</sup> and light-emitting devices,<sup>140, 141</sup> to name a few. Hydrosilylation is a commonly used tool to functionalize Si surface with alkenes or alkynes via the formation of Si–C bonds. This reaction can be initiated in a number of ways, including the use of heat, radical initiators, and light. Among them, light-promoted hydrosilylation is promising because it is clean and efficient and can be patterned via masking/shadowing; it requires no input of thermal energy and thus may reduce surface contamination and the numbers of defects.<sup>67, 71</sup>

The Sugimura group showed the utility of plasmon-mediated surface chemistry on silicon in a set of experiments using gold nanoparticles conjugated with alkene-terminated thiols.<sup>84</sup> When irradiated with visible light that corresponds with the LSPR-based absorption maximum of gold nanoparticles, more gold nanoparticles adhered to the Si(111)–H surface due to hydrosilylation between terminal alkenes and the silicon surface, as compared to the cases when different wavelengths (longer, shorter) were used. Two years later, inspired by this work, our group introduced the concept of “plasmonic stamps”,<sup>85, 86, 142</sup> transparent and flexible PDMS stamps with gold

nanopatterns to drive hydrosilylation on silicon surfaces with various “ink” molecules (alkenes and alkynes) on silicon wafers of different doping levels. Liu et al. found that the hydrosilylation yield is influenced strongly by the doping level of the silicon and proposed that a metal-insulator-semiconductor (MIS) junction drives the accumulation of plasmonically generated holes at the Au-organic-Si interface; the schematic mechanism figure is shown in Figure 2.8.<sup>86</sup> Several assumptions regarding this proposed mechanism remain to be explored to substantiate it fully.

Investigating the kinetics of catalytic reactions is a very useful way to understand the mechanism of any chemical reaction, including those that are plasmon-driven.<sup>143</sup> Currently, the reported ways to monitor the kinetics of plasmon-driven chemical reactions either take advantage of surface-enhanced Raman scattering (SERS) or tip-enhanced Raman scattering (TERS) technology.<sup>144–150</sup> A very recent example reported in 2020<sup>151</sup> used SERS and TERS together to investigate the plasmon-driven reaction kinetics of *p*-aminothiophenol (PATP) and *p*-nitrothiophenol (PNTP) dimerizing into *p,p'*-dimercaptoazobenzene (DMAB) on rough metal surfaces. The results indicate that the electron acceptor or donor plays a decisive role in whether the reactions can occur (Figure 3.1).

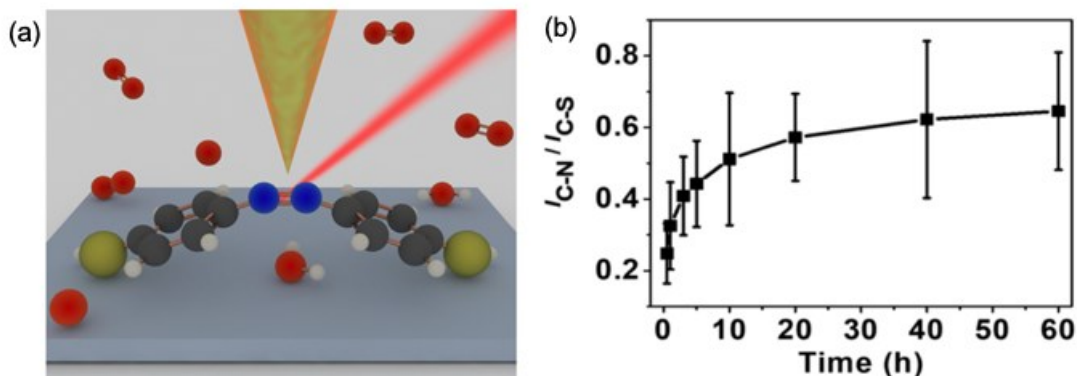


**Figure 3.1 (a) Scheme of azo-dimerization reactions of PATP and PNTP molecules, monitored by high-vacuum TERS. (b) Raman peak intensity ratio of  $I_{C-N}/I_{C-S}$  on Ag surfaces, which were oxidized for different time durations in air, varying from 0.5 to 60 h. The ratio increased with the oxidation time, indicating that more PATP molecules converted into DMAB molecules on the Ag surface. Reproduced with permission from reference 151. Copyright 2020 American Chemical Society.**

In our case, as plasmon-induced hydrosilylation occurs on flat silicon substrates, water contact angle measurements can be used to study the kinetics; the contact angle value will increase or decrease after surface functionalization, depending on the functional group on the silicon surface, the length of carbon chain, and the density of packing.<sup>152–154</sup> For example, in 2012, Huck et al. carried out kinetic studies on UV-initiated hydrosilylation with various “ink” molecules and found that the addition of aromatic compounds caused the reaction to proceed much faster,<sup>155, 156</sup> which supports a mechanism involving the ejection of electrons to leave behind reactive holes (Figure 3.2).

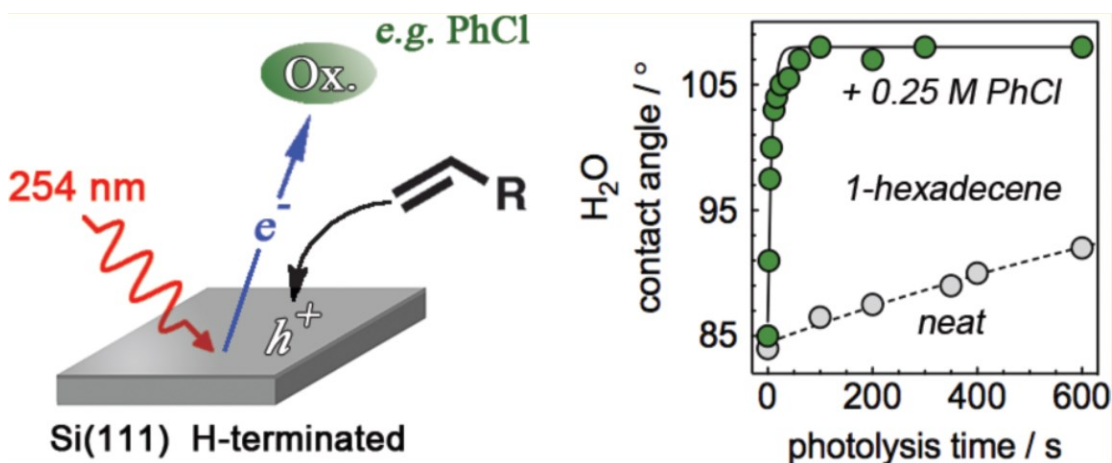
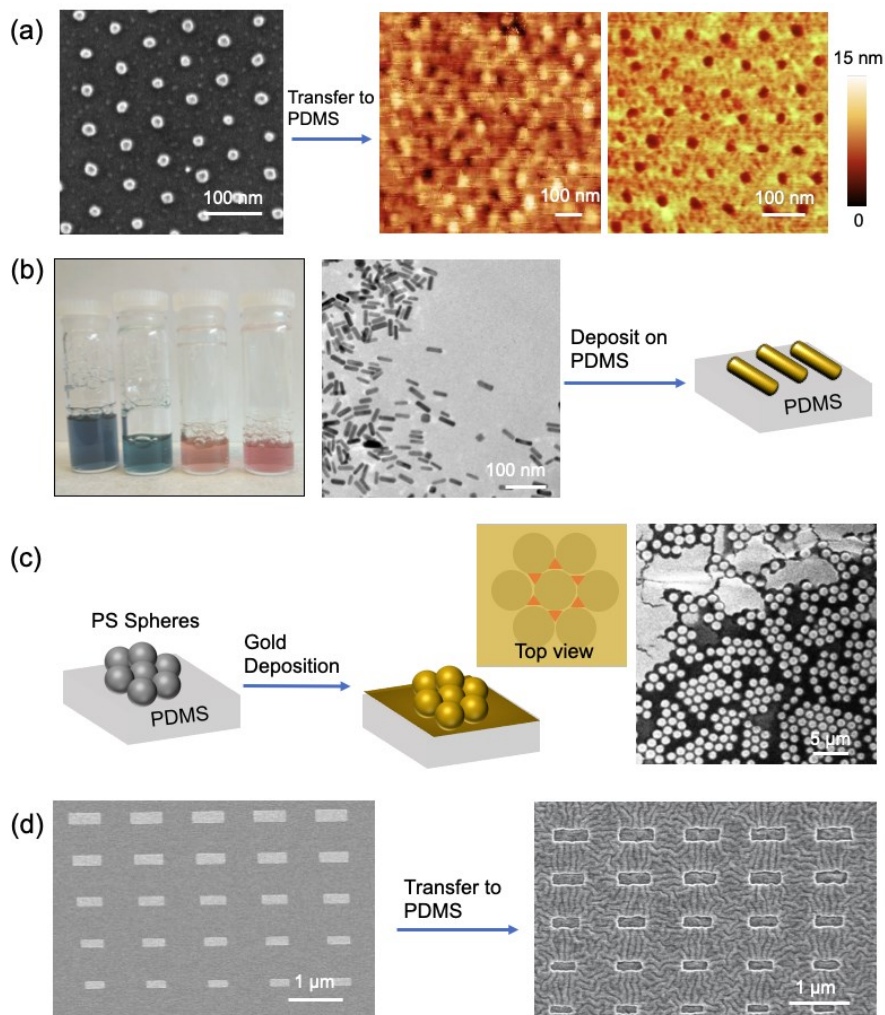


Figure 3.2 Water contact angle of the surface of Si(111)–H coated with neat hexadecene and 0.25 M PhCl in hexadecene and irradiated with 254 nm light. Reproduced with permission from reference 155. Copyright 2012 American Chemical Society.

In order to perform a systematic kinetic study of plasmon-induced hydrosilylation, a reproducible and scalable method is of great need. The block-copolymer self-assembly approach to make the gold nanoparticle arrays is very challenging, and there were persistent difficulties related to reproducibility. In our group, we had screened five methods internally, including bottom-up self-assembly (metallization of block copolymers<sup>157</sup> and colloid gold nanorods synthesis<sup>158, 159</sup>) and top-down methods (nanosphere lithography,<sup>160</sup> electron-beam lithography,<sup>161</sup> and gold sputtering and dewetting), as shown in Figure 3.3. Among all these methods, gold dewetting on PDMS directly appears to be the most scalable and reliable method and hence was used for this systematic study of plasmon-induced hydrosilylation. We first

improved the gold dewetting method further and optimized the sputtering rate and film thickness before using the as-prepared PDMS plasmonic stamps to drive hydrosilylation on flat Si(111)-H substrates with various doping levels. A physical model was built to show the relationship between reaction rate and doping density, optical absorption coefficients, depletion width, and the plasmonic E-field.



**Figure 3.3** Four additional methods tested for the fabrication of plasmonic stamps. (a) Preparation of gold hexagonal patterns on silicon wafers via block copolymer metallization followed by transfer of the gold nanoparticles to PDMS. (b) Gold nanorods with tunable aspect ratios were synthesized and then deposited onto blank PDMS. Wet chemistry needs multiple synthetic and purification steps, and surface ligands on gold nanorods could be an obstacle for the following reaction. (c) Deposition of polystyrene (PS) nanospheres on PDMS directly, followed by gold deposition. This approach was complicated by residual PS spheres. (d) Preparation of gold nanorods of various sizes by electron-beam lithography (EBL) on silicon wafers, followed by transfer to PDMS. The gold nanorods could not be removed by the PDMS.

## 3.2 Kinetic Studies of Plasmon-induced Hydrosilylation on Si Surfaces

The parameters for the gold deposition on the PDMS needed to be refined further. First, a clear understanding of the thickness of the gold layer on the PDMS stamp is needed before dewetting. Because PDMS is soft and nonconducting, direct measurement of the gold film's thickness and dewetted gold nanoparticles on PDMS was more difficult than on silicon surfaces. The surfaces of native oxide-capped silicon wafers and PDMS are chemically similar, thus the sputter-deposited gold would be expected to have almost the same sticking coefficient, and the relative differences in gold film thickness and dewetting behavior would be expected to be the same for both surfaces. Therefore, gold films were sputtered onto native oxide-capped silicon chips to study the relationship between sputtering rate, film thickness, and dewetting behaviors.

The SEM images in Figure 3.4 show the morphology of gold films (5.0 nm and 10.0 nm) sputtered onto silicon wafers. As the sputtering rate is increased from 0.16 nm/s to 0.22 nm/s, the film becomes more discontinuous for both 5.0 nm and 10.0 nm thick gold films. With the same sputtering rate (0.22 nm/s), when the gold film thickness is increased from 2.5 nm to 10.0 nm (thickness was measured by AFM height profiles, shown in Figure 3.6), the film becomes more continuous (Figure 3.5a), leading to different thermal dewetting morphologies after heating for 20 h at 150 °C. Specifically, gold dewetting only partially occurred when the thickness of gold films exceeded 5.0 nm (Figure 3.5b). Therefore, we know that the continuity of the as-sputtered gold film is closely related to the sputtering rate, i.e., gold films sputtered at lower rates have better continuity. When the sputtering rate is the same, thicker films have better continuity, which eventually affects or even hinders the gold dewetting process.

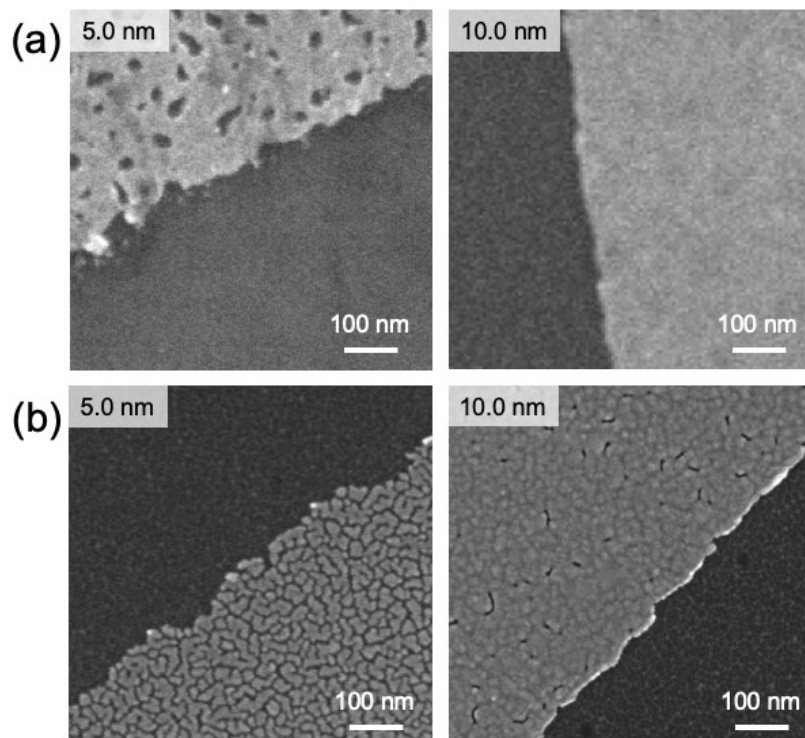


Figure 3.4 SEM images of the as-sputtered 5.0 and 10.0 nm thickness gold film on Si wafers with different sputtering rate, (a) 0.16 nm/s, (b) 0.22 nm/s.

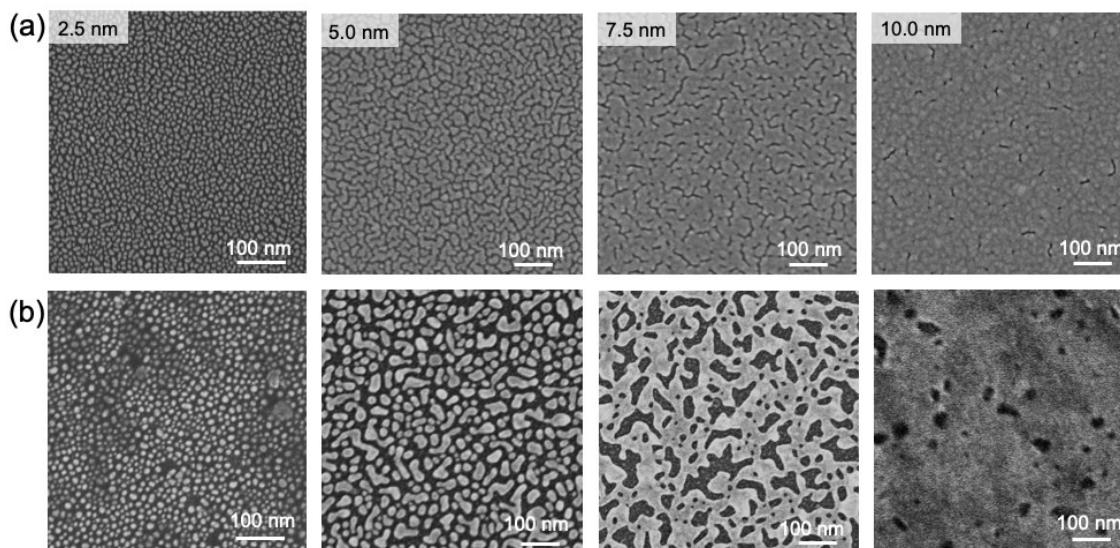


Figure 3.5 SEM images of the as-sputtered gold film on Si wafers with the same sputtering rate (0.22 nm/s), but different thickness (2.5 nm, 5.0 nm, 7.5 nm, 10.0 nm), before (top row) and after (bottom row) dewetting via thermal treatment at 150 °C for 20 h.

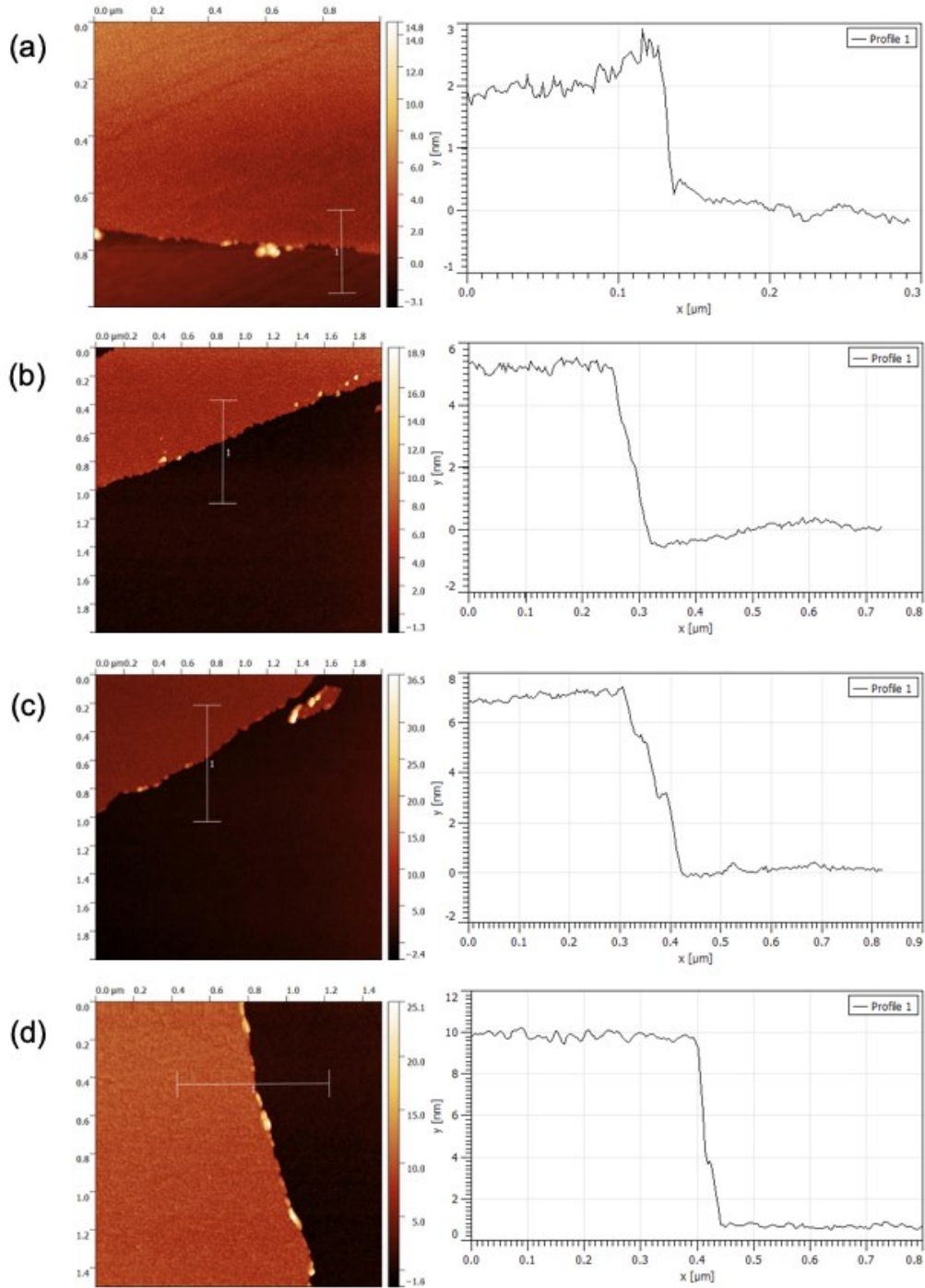
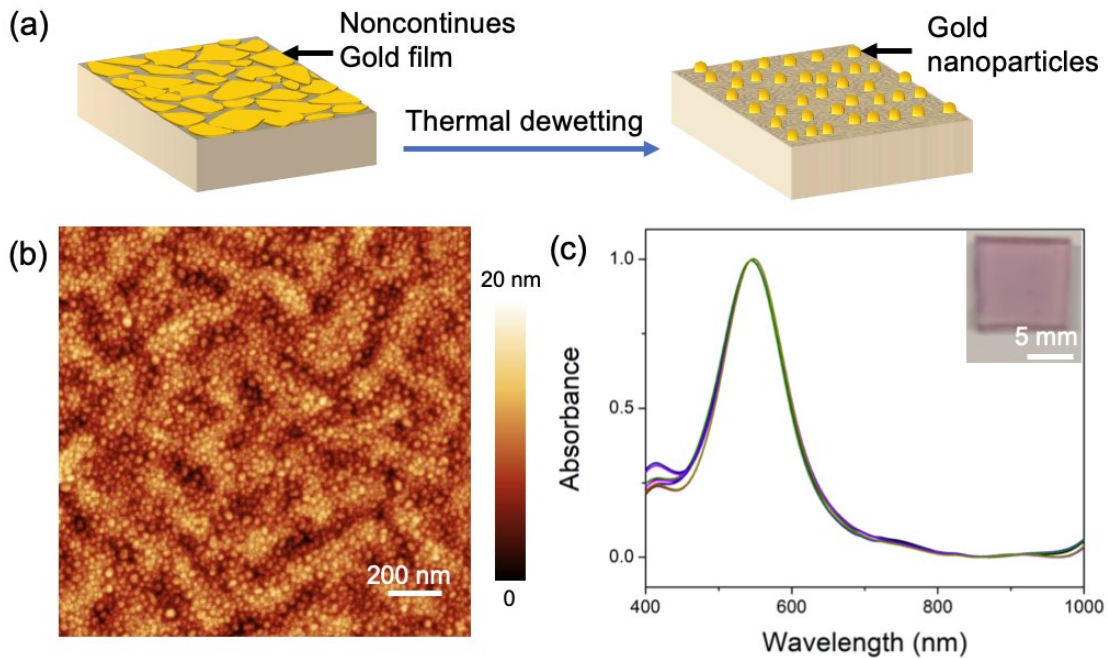


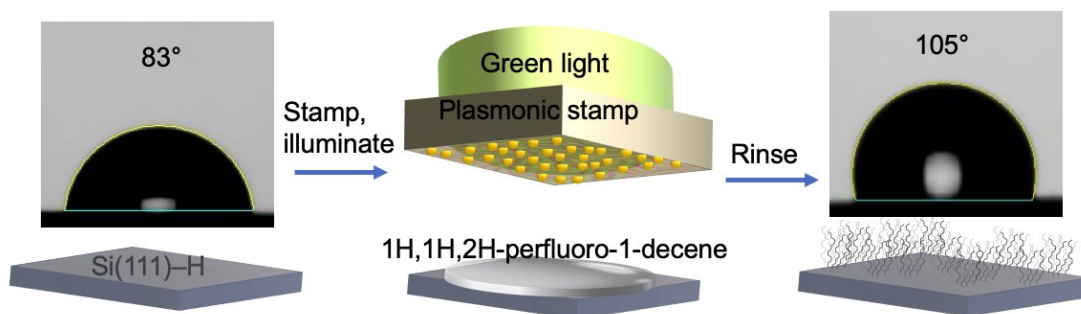
Figure 3.6 Gold films were sputtered onto Si wafers, and AFM height graphs were used to measure the thickness of the gold film. The thickness of gold films are (a)  $2.5 \pm 0.3$  nm, (b)  $5.0 \pm 0.3$  nm, (c)  $7.5 \pm 0.2$  nm, (d)  $10.0 \pm 0.2$  nm, which agree well with the designed thickness, confirming the thickness accuracy and reproducibility of this method.

After optimization for the sputtering rate and film thickness for gold dewetting on Si surfaces, the relationship between sputtering rate and film thickness was determined, leading to a more controllable and repeatable gold dewetting method. Therefore, a 2.5 nm thick gold film sputtered at 0.22 nm/s was used as the working condition for gold dewetting on ~3 mm thick blank PDMS. Upon thermal treatment at 150 °C for 20 h, the gold films dewet into gold nanoparticles on the surface of the PDMS; the scheme and the AFM image are shown in Figure 3.7a and b, respectively. The substrates adopted a wrinkle morphology, which commonly is observed in layered PDMS samples due to the interfacial stresses during dewetting. As shown in Figure 3.7c, the color of the PDMS stamp appears red-pink, and the corresponding UV-visible absorption spectra of dewetted gold nanoparticles on PDMS show a peak at  $546 \pm 3$  nm, corresponding to the LSPRs of the newly formed gold nanoparticles. The UV-vis spectra for ten different plasmonic stamps are quite identical, confirming the repeatability of gold dewetting on the PDMS method and thus enabling the following kinetic study for plasmon-induced chemical reactions.



**Figure 3.7** (a) Schematic representation of gold dewetting on PDMS process. (b) AFM height images of plasmonic stamps fabricated from dewetted Au films on PDMS. (c) UV-vis spectra for ten plasmonic stamps; the inset photograph is the plasmonic stamp.

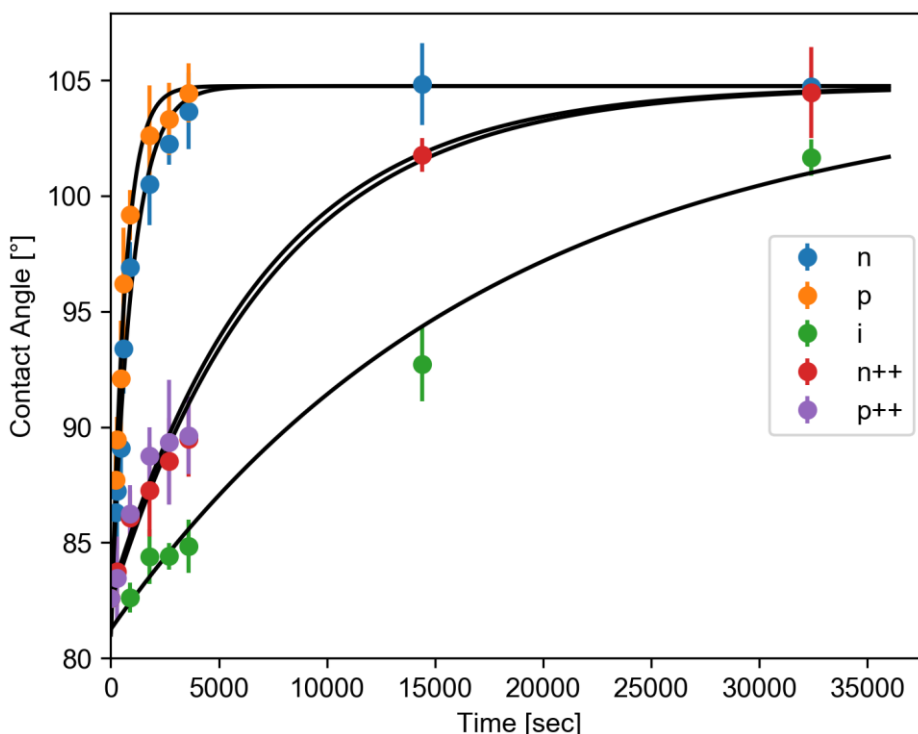
Driving silicon surface-mediated chemistry by as-prepared PDMS stamps involved three parts, a freshly prepared Si(111)–H surface, sandwiching a thin layer of the “ink” molecule (1H,1H,2H-perfluoro-1-decene) between the plasmonic stamp, and illumination the silicon surface through the PDMS stamp and molecular layer with green light, as shown in Figure 3.8. After the reaction, the silicon surface was rinsed with dichloromethane, and the water contact angle increased from  $\sim 83^\circ$  to  $\sim 105^\circ$ , which is less than would be expected for a complete, smooth, and uninterrupted monolayer due to the patchy nature of the plasmonic stamp-induced hydrosilylation.



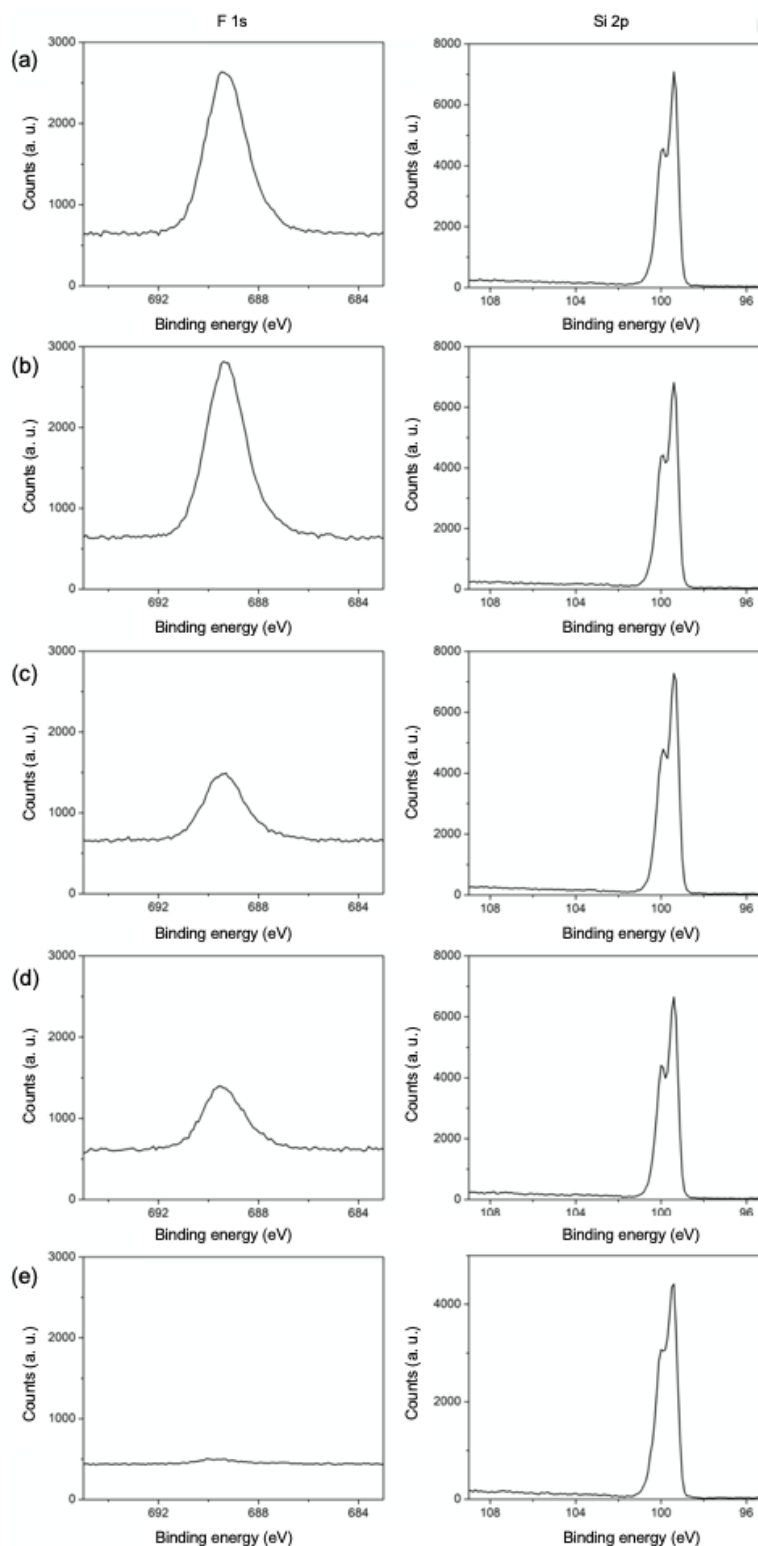
**Figure 3.8** Scheme of plasmonic stamp-assisted hydrosilylation on a Si(111)–H surface. Green light shines through the optically transparent, PDMS-based plasmonic stamp with gold nanoparticle on the surface. Hydrosilylation occurs in a spatially defined fashion on the Si(111)–H surface, resulting in the increment of water contact angle from  $\sim 83^\circ$  to  $\sim 105^\circ$ .

Figure 3.9 shows the growth of the water contact angle on silicon surfaces resulting from the plasmon-induced hydrosilylation by using 1H,1H,2H-perfluoro-1-decene. Five kinds of silicon wafers with different doping levels were used to investigate their reaction kinetics for up to 9 h. The water contact angle for plasmon-induced hydrosilylation silicon wafers with 1H,1H,2H-perfluoro-1-decene eventually will reach the same value ( $\sim 105^\circ$ ) when the reaction time is long enough (over 9 h). However, the water contact angle at 1 h reaction time is quite different on five kinds of silicon wafers, with  $n^{++}$  and  $p^{++}$  silicon showed only a small increase in water contact angle after hydrosilylation, to  $\sim 90^\circ$  from  $\sim 83^\circ$  for freshly etched Si(111)–H. Intrinsic silicon showed no significant increase in water contact angle, while in terms of lightly doped  $n$ - and  $p$ -type silicon, the water contact angles increased from  $\sim 83^\circ$  for freshly etched Si(111)–H to  $\sim 105^\circ$  for 1H,1H,2H-perfluoro-1-decene modified silicon

surfaces. The corresponding X-ray photoemission spectroscopy (XPS) spectras are shown in Figure 3.10. The F(1s) signal is used to compare the yield of hydrosilylation reactions at 1 h for five kinds of silicon wafers. Hydrosilylation on lightly doped n- and p-type silicon (Figure 3.10a and b) shows the highest F(1s) signal intensity, followed by n++ and p++ type silicon (Figure 3.10c and d), while intrinsic silicon (Figure 3.10e) has the lowest intensity among all of them. The Si 2p spectra of all the silicon samples reveal no significant oxidation, which would appear as higher energy features above 102 eV due to the oxidation insertion into surface Si–Si and Si–H bonds.<sup>76, 162</sup>



**Figure 3.9** Kinetic profile of plasmonic stamp-assisted hydrosilylation on a hydrogen-terminated Si(111) surface of various doping densities and types. Data is fitted to the pseudo-first-order kinetics (equation 3.4). Each black dot represents a unique sample that had been reacted for the indicated reaction time. The error bars represent the standard deviation of five measurements.



**Figure 3.10** High-resolution X-ray photoelectron spectroscopy (XPS) of each sample was taken of the F(1s) and Si(2p) regions. The hydrosilylation of 1H,1H,2H-perfluoro-1-decene on Si(111)-H occurred on different silicon wafers through plasmonic stamps for 1 h. (a) n-type silicon, (b) p-type silicon, (c) n<sup>++</sup>-type silicon, (d) p<sup>++</sup>-type silicon, and (e) intrinsic silicon.

## 3.3 Mechanistic Understanding of Plasmon-induced Hydrosilylation on Si Surfaces

### 3.3.1 Reaction Rate Calculations

Shown in Figure 3.9 are the water contact angles of various silicon substrates of different doping types and levels that have undergone plasmonic stamping. As expected from previous work by Huck et al.<sup>155</sup> the water contact angle increases as the illumination time increases, until a terminal contact angle is reached ( $\sim 105^\circ$ ), which physically corresponds to a terminally substituted surface. A mathematical description of the hydrosilylation kinetics, which follows first-order adsorption, is straightforward to derive. If there are a total of  $N$ , available surface sites for grafting on the silicon surface, then the rate of change in the number of grafted sites,  $N_g$ , is assumed to be proportional to the number of available surface sites,

$$\frac{dN_g}{dt} = kN = k(N_T - \beta N_g - N_{ox}) \quad (3.1)$$

where  $N_T$  is the total number of surface sites of H-terminated silicon and  $N_{ox}$  is the number of Si sites that have become oxidized. The prefactor  $\beta$  is a steric parameter, which accounts for the average number of silicon sites that become unavailable after a molecule is grafted to the silicon surface. For planar aromatic molecules, the value of  $\beta$  can be quite large ( $\beta \approx 7$ ), while linear molecules are expected to have  $\beta$  values in the range of 1 to 3.<sup>43</sup> Lastly, the proportionality factor,  $k$ , which is known as the first-order rate constant or kinetic constant, quantifies the rate of the hydrosilylation reaction. If it is assumed that oxidation of the silicon is negligible, which is substantiated by XPS measurements shown in Figure 3.10, Equation 3.1 can be converted to substitution level,  $\phi = N_g/N_T$ , and subsequently solved to yield

$$\phi = \frac{1 - \exp(-\beta kt)}{\beta} \quad (3.2)$$

If we take the limit as the time approaches infinity the substitution level equals  $1/\beta$ , which gives a value for the physically intuitive resting maximum substitution level,  $\phi_M$ , is equal to  $1/\beta$ . It is also noted that we can write  $k_{obs} = \beta k$ , which gives the following equation for the relative substitution level,  $\phi_r$ ,

$$\phi_r = \phi/\phi_M = 1 - \exp(-k_{obs}t) \quad (3.3)$$

Finally, the relative substitution level can be related to the experimentally measured water contact angle,  $\theta_w$ , by assuming that they are linearly related

$$\begin{aligned} \theta_w &= \theta_0 + (\theta_M - \theta_0)\phi_r \\ \theta_w &= \theta_0 + (\theta_M - \theta_0)(1 - \exp(-k_{obs}t)) \end{aligned} \quad (3.4)$$

where  $\theta_0$  is the water contact angle for H-terminated silicon ( $\sim 82 \pm 1^\circ$ ) and  $\theta_M$  is the maximum contact angle for a terminally substituted surface.

The data in Figure 3.9 are fitted to Equation 3.4 by implementing a non-linear least squares algorithm from SciPy (a Python library). The value of  $\theta_0$  is constrained to the range of  $80\text{--}84^\circ$  and  $k_{obs}$  is constrained to the range of  $10^{-7}\text{--}10^{-1} \text{ sec}^{-1}$ , while the value of  $\theta_M$  is fixed at  $104.8^\circ$ . The maximum contact angle is constrained to be the same for all substrates, independent of the doping level, as there is no thermodynamic/chemical reason to believe that the terminal substitution would change, as even in the most heavily doped case ( $N_d = 1.8 \times 10^{19} \text{ cm}^{-3}$ ), there is roughly 1 dopant atom per 3000 silicon atoms on the surface. This assumption is substantiated by the data acquired for n, n++, and intrinsic silicon, where it appears that all surfaces eventually approach the same terminal contact angle, independent of the substitution level. The fixed terminal contact angle of  $104.8^\circ$  is chosen by taking the average value of the contact angles of the n and n++ substrates measured after 9 h of continuous hydrosilylation via plasmonic stamping. Lastly, when fitting these data, the uncertainty in each measured data point is accounted for by minimizing the following objective function,

$$\min \left( \sum_{i=1}^N \frac{(f(t_i, \theta_0, k_{obs}) - \theta_i)^2}{\sigma_i^2} \right) \quad (3.5)$$

where  $\sigma_i$  are the standard deviations of the contact angle on the same sample from five measurements. The results of these fittings are shown in Figure 3.9, and the values of rate constants are in Table 3.1, where the uncertainty of the rate constant is computed from the covariance matrix of the fitting procedure.

**Table 3.1 Resistivity, Rate Constants for Plasmon-induced Hydrosilylation for Five Kinds of Silicon Wafers.**

Si type	Resistivity ( $\Omega$ cm) <sup>a</sup>	$k_{\text{obs}}$ ( $10^{-3}$ s <sup>-1</sup> )
n	$15.09 \pm 0.21$	$1.0 \pm 0.1$
p	$6.53 \pm 0.51$	$1.6 \pm 0.1$
n <sup>++</sup>	$0.0036 \pm 0.00002$	$0.13 \pm 0.01$
p <sup>++</sup>	$0.0067 \pm 0.00008$	$0.14 \pm 0.04$
Intrinsic	$15173 \pm 866$	$0.057 \pm 0.005$

<sup>a</sup>Measurements, with the uncertainty given as standard deviation of these measurements; at least 10 measurements were collected.

The following important observations from these data are made: the rate constant of moderately n-type doped silicon is  $\sim 10$ x larger than degenerately doped n<sup>++</sup> silicon and  $\sim 20$ x larger than intrinsic silicon. The rate constants of p-type silicon with similar doping to the n-type silicon are within the same order of magnitude, but slightly higher.

### 3.3.2 Mechanistic Discussion

From previous work exploring plasmonic stamping on H-terminated silicon, the following mechanisms were explored: resonant photon scattering, nanoparticle plasmonic heating, hot carrier injection, and near-field electromagnetic electron-hole pair generation (EHP),<sup>85</sup> where it was concluded that near-field electromagnetic EHP generation from the plasmonic field in the Si substrate was the candidate most responsible for the plasmonic stamping effect. In follow-up work, which looked at the effect of changing the doping density, it was proposed that the Schottky or metal-insulator-semiconductor (MIS) junction formed between the Au nanoparticles and the silicon substrate had a major role to play.<sup>86</sup> The theoretical band diagrams at the MIS junction shown in Figure 3.11, for the different types of doped silicon used in our work (n<sup>++</sup>, n, i, p, and p<sup>++</sup>) are either only upward band bending or flat band conditions, because of the deep work function of Au ( $\sim 5.15$  eV) relative to the Fermi level of the

silicon. In the case of upward band bending, injected/photogenerated holes will be swept toward the interface and electrons away from the interface. Therefore, if holes are either injected or photogenerated within the depletion width of the junction, they will be swept toward the junction to subsequently drive the hydrosilylation reaction.<sup>86</sup>

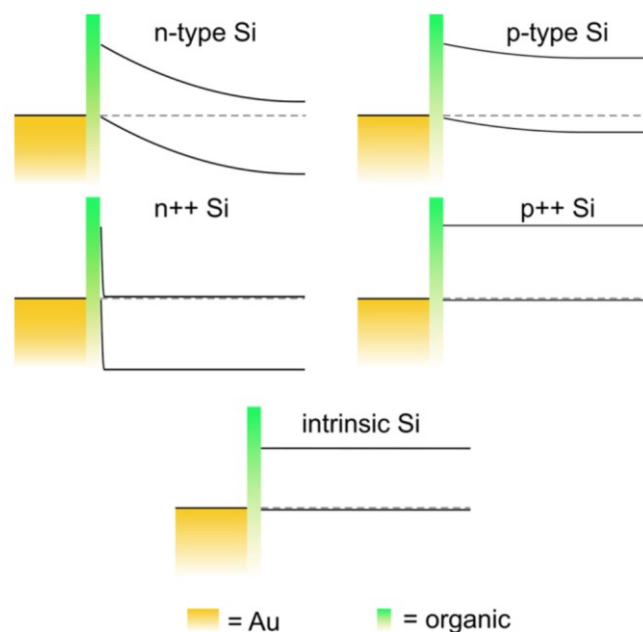


**Figure 3.11** Theoretical band diagrams of the gold–organic–silicon junction for different doping levels and types of Si substrates. All band diagrams are shown to a distance of 800 nm from the interface and were calculated using the Mott–Schottky rule. Reproduced with permission from reference 86. Copyright 2016 American Chemical Society.

Specifically, it was found that after an hour of constant illumination, the contact angle of the n and p-type silicon substrates had much higher contact angles than the degenerately doped substrates, which was again still higher than the intrinsic Si substrate. This observation was attributed to the much longer expected depletion regions of the moderately doped silicon (~300–2000 nm), compared to the much shorter depletion width of the degenerately doped silicon (~1–5 nm), where photogenerated holes are expected to be swept to the silicon surface via the action of the built-in electric field of the depletion region. This mechanistic hypothesis was largely qualitative as it was difficult to connect a single contact angle measurement to theoretical predictions.

Now that we have measured the kinetic rate constants, it should be possible to connect these experimentally measured constants to theoretical predictions. The important observation is that the rate of the reaction (rate constant) should be directly proportional to the density of holes at the surface,<sup>163</sup> which is proportional to the short-circuit current density,  $J_{sc}$ , or photoinduced current density,  $J_{ph}$ , of the Schottky junction under illumination. To estimate the  $J_{ph}$ , it is first necessary to calculate the values of key parameters of these junctions for the different types of silicon substrates used, which are shown in Table 3.2 below.

**Table 3.2 Important Parameters of Schottky Junction Between Au and Silicon of Various Doping Types and Levels.  $N_d$ : doping density;  $E_F$ : Fermi level;  $V_{bi}$ : built-in electrical field;  $W$ : depletion width;  $1/\alpha_{526}$ : illumination length.**

Si type	$N_d$ (cm <sup>-3</sup> )	$E_F$ (eV)	$V_{bi}$ (eV)	$W$ (nm)	$1/\alpha_{526}$ (nm)
n	$2.97 \times 10^{14}$	4.35	0.80	$1.9 \times 10^3$	250
n++	$1.81 \times 10^{19}$	4.06	1.09	8.9	125
p	$2.10 \times 10^{15}$	4.93	0.22	$3.7 \times 10^2$	250
p++	$1.53 \times 10^{19}$	5.16	0.01	1.1	200
Intrinsic	$8.30 \times 10^9$	4.61	0.54	$2.92 \times 10^5$	250

In Table 3.2 the doping density,  $N_d$ , is determined experimentally from four-point probe resistivity measurements listed in Table 3.1. The Fermi level,  $E_F$ , is determined from the following equations,

$$E_{Fn} = \chi + \frac{k_B T}{q} \ln(N_c/N_d)$$

$$E_{Fp} = \chi - \frac{k_B T}{q} \ln(N_v/N_d) + E_g \quad (3.6)$$

where  $\chi$  is the electron affinity of silicon (4.05 eV),  $k_B T/q$  is the thermal energy of the charge carriers at a temperature  $T$  (25.9 meV),  $E_g$  is the indirect bandgap of silicon (1.12 eV), while  $N_c$  and  $N_v$  are the density of states at the conduction and valence band

edges, which are  $2.81 \times 10^{19}$  and  $1.88 \times 10^{19} \text{ cm}^{-3}$ , respectively. The built-in field,  $V_{\text{bi}}$ , is estimated using the Mott-Schottky rule,<sup>164</sup>

$$V_{\text{bi}} = \phi_{\text{Au}} - E_{\text{F}} \quad (3.7)$$

where  $\phi_{\text{Au}}$  is the work function of gold, which is assumed to be 5.15 eV. The depletion width,  $W$ , is given by

$$W = \sqrt{\frac{2\epsilon_{\text{si}}V_{\text{bi}}}{qN_{\text{d}}}} \quad (3.8)$$

where  $\epsilon_{\text{si}}$  is the permittivity of silicon ( $1.05 \times 10^{-12} \text{ F/cm}$ ). Finally,  $\alpha_{526}$  is the optical absorption coefficient of silicon at 526 nm (values taken from ref. 23).

Using these Schottky junction properties we can begin to formulate a mechanistic understanding of the plasmonic stamping hydrosilylation reaction kinetics. For the sake of simplicity, we shall restrict ourselves to n-type substrates for the time being. When the plasmonic stamp is placed in contact with the substrate, there is a net flow of majority carriers (electrons) towards the interface in order to equilibrate the Fermi levels between the n-type silicon and the gold nanoparticles. This results in a built-in field, over the depletion width (Equation 3.8) where the photogenerated holes are swept toward the junction, and electrons swept in the opposite direction. The generation rate of EHPs in the silicon at depth,  $x$ , from the surface will be proportional to the electromagnetic field strength of the incident illumination, which can be approximated by Beer's Law,

$$G(x, \lambda) = G_0 \exp(-\alpha(\lambda)x) \quad (3.9)$$

where  $G_0$  is the EHP generation rate at the surface and  $\alpha(\lambda)$  is the absorption coefficient as a function of the incident illumination wavelength. For the purposes of this analysis, we assume a constant absorption coefficient, which is a reasonable approximation since the incident white light is filtered over a narrow wavelength range. As such, the absorption coefficient is taken at the center wavelength of the filter of 526 nm, which is listed in Table 3.2. The total rate of carrier absorption,  $G_{\text{T}}$ , can be determined by integrating equation 3.9,

$$G_{\text{T}} = \int_0^{\infty} G(x) dx = G_0/\alpha_n \quad (3.10)$$

Using this result, we can make the simplifying assumption that there is a uniform illumination over a distance of  $1/\alpha$ , with a constant generation rate  $G_0$ , which will

result in the same total carrier generation rate. Using this model of carrier generation, we can approximate the photogenerated current density of holes of these illuminated Schottky junctions.

The current density needs to be broken up into two parts: the drift current  $J_d$ , and the diffusion current  $J_{diff}$ . The drift current is the current from EHPs generated within the depletion region and the diffusion current is from EHPs generated outside the depletion region. Furthermore, the photocurrent density needs to be separated into the current from the EHPs generated from the intense E-field of the plasmons and the continuous wave (CW) illumination of the incident light source.

For the moderately doped n-type silicon used in this work, the depletion width is  $\sim 1900$  nm, which is much larger than the illumination length,  $L_{op} = 1/\alpha = 250$  nm. As such, the diffusion current is zero, as all EHPs are generated within the depletion region,

$$J_n^{CW} = qG_0/\alpha_n \quad (3.11)$$

In the case of degenerately doped n++ silicon, the depletion width ( $\sim 9$  nm) is much less than the illumination length (125 nm), as such, EHPs will be generated outside of the built-in field, and holes will diffuse isotropically a distance  $L_D$ , before they recombine (on average), which is known as the diffusion length.<sup>164</sup> It is straightforward to show that if  $G_0 dx$  holes are generated at a depth,  $x$ , from the surface, the diffusion current density contribution from these holes will be  $qG_0(1 - x/L_D)/2dx$ , which is integrated to give the final result,

$$J_{n^{++}}^{CW} = \int_0^{\frac{1}{\alpha}} \frac{qG_0}{2} (1 - x/L_D) dx = \frac{qG_0}{2\alpha} (1 - 1/2\alpha L_D) \quad (3.12)$$

The diffusion length of n++ silicon is  $\sim 2$   $\mu$ m, the value of  $1/2\alpha L_D = 0.03 \ll 1$ , which gives the simple result of

$$J_{n^{++}}^{CW} = \frac{qG_0}{2\alpha} \quad (3.13)$$

For intrinsic silicon, the depletion width is very large, however, due to the extremely low density of the majority carriers ( $\sim 8.3 \times 10^9$  cm<sup>-3</sup>), the built-in field strength is very weak, and the average kinetic energy imparted by the built-in field is less than the thermal energy at room temperature (25.9 meV). As such, the current density from the

CW illumination is identical to the n++ substrate, being purely diffusional (the diffusion length of intrinsic silicon is even larger than n++).

$$J_i^{\text{CW}} = \frac{qG_0}{2\alpha} \quad (3.14)$$

Next, we need to consider the additional charge carriers generated by the plasmonic field. The plasmonic E-field can be very intense, generating a very high density of charge carriers within the effective spatial extent of the plasmonic field,  $W_{\text{SPR}}$ . The generation rate due to the plasmonic field is

$$G_{\text{SPR}} = SG_0 \quad (3.15)$$

where  $S$  is the enhancement factor of the plasmonic field. For n-type silicon, the depletion width is larger than the spatial extent of the plasmonic field, and it is assumed that all of the plasmonically generated carriers will be swept towards the junction,

$$J_n^{\text{SPR}} = qG_0SW_{\text{SPR}} \quad (3.16)$$

If we now combine Equation 3.11 and Equation 3.16, the total photocurrent density is given by

$$J_n = J_n^{\text{CW}} + J_n^{\text{SPR}} = qG_0\left(\frac{1}{\alpha} + SW_{\text{SPR}}\right) \quad (3.17)$$

For degenerately doped silicon the depletion width is very small ( $\sim 9$  nm), likely less than the effective spatial extent of the plasmonic field. Therefore, it is assumed that any charge carriers generated outside of the depletion region will recombine rapidly due to the extremely high density of EHPs generated by the plasmonic field. The photocurrent density due to the plasmonic field is thus

$$J_{n++}^{\text{SPR}} = qG_0SW \quad (3.18)$$

where the final expression for the total photocurrent density of n++ silicon is

$$J_{n++} = J_{n++}^{\text{CW}} + J_{n++}^{\text{SPR}} = qG_0\left(\frac{1}{2\alpha} + SW\right) \quad (3.19)$$

For intrinsic silicon, we assume that none of the plasmonically generated charge carriers are captured due to the weak built-in field, and the total photogenerated current is given by Equation 3.14. Given that the kinetic rate constant will be proportional to the photocurrent densities, the ratio of rate constants should equal the corresponding ratio of photocurrent densities. For the ratio between n++ and intrinsic silicon,

$$\frac{k_{++}}{k_i} = \frac{J_{++}}{J_i} = \frac{1/2\alpha_{++} + SW_{++}}{1/2\alpha_i}$$

$$\Rightarrow S = \frac{1}{2W_{++}} \left( \frac{k_{++}}{\alpha_i k_i} - \frac{1}{\alpha_{++}} \right) \quad (3.20)$$

It is worth noting at this point that the depletion widths listed in Table 3.2 are what would be expected for no illumination. However, under illumination, the bands will move towards flat band conditions, as when calculating the value of  $S$ , a reduced depletion width of 4.5 nm (instead of 8.9) is used. Using the values in Table 3.2 and the experimentally determined ratio of rate constants ( $k_{++}/k_i \sim 2.3$ ), the enhancement factor is estimated to be  $\sim 50$ . Next, we take the ratio of n-type and intrinsic, giving the expression,

$$\begin{aligned} \frac{k_n}{k_i} &= \frac{J_n}{J_i} = \frac{1/2\alpha_n + SW_{\text{SPR}}}{1/2\alpha_i} \\ \Rightarrow W_{\text{SPR}} &= \frac{1}{S} \left( \frac{k_n}{2\alpha_i k_i} - \frac{1}{\alpha_n} \right) \end{aligned} \quad (3.21)$$

Again, if we use the values in Table 3.2, the experimentally determined ratio of rate constants ( $k_n/k_i \sim 17.5$ ) and value of  $S = 49$ , the value of  $W_{\text{SPR}}$  comes to 39 nm, which is physically reasonable. Finally, the expression for the ratio of rate constants for n-type to n++ is given by

$$\frac{k_n}{k_{++}} = \frac{J_n}{J_{++}} = \frac{1/\alpha_n + SW_{\text{SPR}}}{1/2\alpha_i + SW_{++}} \quad (3.22)$$

Utilizing the derived values of  $S = 50$ ,  $W_{\text{SPR}} = 39$  nm, and the absorption coefficients from Table 3.2, the predicted value of the rate constant ratio is 9.2. This predicted ratio of 9.2 agrees remarkably well with the experimental value of  $k_n/k_{++} \sim 7.7$ , especially considering the large number of simplifying assumptions that went into this model.

It is believed that in the case of p-type silicon, a similar analysis can be applied, despite the majority carriers being holes. This is due to the very deep work function of Au, which still results in holes being swept towards the silicon surface. The higher experimentally observed rate constants for p-type silicon (compared to n-type) are not entirely clear at this point, but it may be due to the additional holes that are accumulated at the silicon surface from the Schottky junction.

### 3.4 Conclusions

Detailed mechanistic studies involving silicon wafers with different doping densities revealed critical insights that allowed us to tie together charge mobility, doping, and

surface chemistry, driven by the electric field of localized surface plasmon resonance. The Si(111)-H interfaces comprised silicon wafers with the following doping regimes: n, p, n<sup>++</sup>, p<sup>++</sup>, and intrinsic type silicon. Water contact angles of the hydrosilylated and functionalized silicon surfaces revealed strong differences of reaction rate coefficients, and XPS spectra showed successful hydrosilylation on silicon surfaces, with no oxidation. A physical model was built, which predicts the rate constant as a function of doping density, optical absorption coefficients, depletion width, and the plasmonic E-field. The rate constant is proportional to the current density of holes, which is composed of the drift current (charge movement from the built-in field from the Schottky junction) and the diffusion current of photogenerated charges.

## **3.5 Experimental Section**

### **3.5.1 Materials**

Si wafers (111-oriented, prime grade, p-type, B-doped,  $\rho = 1-10 \text{ } \Omega \text{ cm}$ , thickness of 600–650  $\mu\text{m}$ ; 111-oriented, prime grade, n-type, P-doped,  $\rho = 1-10 \text{ } \Omega \text{ cm}$ , thickness of 600–650  $\mu\text{m}$ ; 111-oriented, prime grade, n-type, As-doped,  $\rho = 0.001-0.004 \text{ } \Omega \text{ cm}$ , thickness of 500–550  $\mu\text{m}$ ; 111-oriented, prime grade, p-type, B-doped,  $\rho = 0.001-0.005 \text{ } \Omega \text{ cm}$ , thickness of 400–450  $\mu\text{m}$ ) were purchased from WRS Materials Inc. Millipore water (resistivity of 18.2  $\text{M}\Omega\cdot\text{cm}$ ) was used for the preparation of all aqueous solutions. The precursors for Sylgard 184 PDMS were purchased from Dow Corning.  $\text{NH}_4\text{OH}$  (aqueous, 30%) and  $\text{HCl}$  (aqueous, 37%) were purchased from Caledon Laboratories, Ltd.  $\text{H}_2\text{O}_2$  (aqueous, 30%) was obtained from Sigma-Aldrich.  $\text{NH}_4\text{F}$  (aqueous, 40%, semiconductor grade) was purchased from Transene Company, Inc. 1H,1H,2H-perfluoro-1-decene (99.0%) from Sigma-Aldrich was passed through a short column of hot alumina (dried at 100 °C for over 24 h and used while still hot) to remove water residues and peroxides, then deoxygenated with nitrogen gas. The optical filter [CW526 (center band wavelength) of 526 nm; full width at half-maximum (fwhm) of 180 nm] was purchased from Edmund Optics Inc.

### 3.5.2 Characterization

SEM images were obtained using a field emission scanning electron microscope (S-4800, Hitachi); the working pressure for imaging was  $<10^{-8}$  Torr. UV-vis absorption spectroscopy measurements were carried out in air using an Agilent UV-8453 spectrophotometer at 1 nm resolution. Prior to measurement, a baseline correction procedure (through a blank PDMS stamp) was implemented. Tapping mode atomic force microscopy (AFM) micrographs were captured using a Digital Instruments/Veeco Nanoscope IV with silicon PPP-NCHR cantilevers purchased from Nanosensors (thickness 4  $\mu\text{m}$ , length 125  $\mu\text{m}$ , width 30  $\mu\text{m}$ , n-type Si with an Al coating, resonance frequency of 330 kHz, force constant of 10–130 N/m, tip height of 10  $\mu\text{m}$ , and tip radius of  $<10$  nm.). Sessile drop contact angles of the functionalized silicon surfaces were measured using 3  $\mu\text{L}$  of water on a Rame-Hart Model 100-00 contact-angle goniometer after the droplet on the sample surface reached a static state. The resistivity of silicon wafers was measured by a Lucus Pro4 4000 sheet and bulk resistivity measurement system with Keithley 2601A sourcemeter. X-ray photoelectron spectroscopy (XPS) spectra were taken on a Kratos Axis Ultra X-ray photoelectron spectroscopy system using an Al source with an energy of 1487 eV, in the University of Alberta nanoFAB, with binding energies calibrated to C(1s) (285.0 eV).

### 3.5.3 Blank PDMS Stamp Preparation

Polydimethylsiloxane (PDMS) prepolymer and the curing agent (Sylgard 184, Dow Corning) were mixed in a 10:1 ratio and degassed by applying a vacuum three times to the prepolymer at room temperature. Then, 10 mL of the mixtures were added to a polystyrene petri dish, with a PDMS layer thickness of  $\sim 3$  mm, and cured at 65  $^{\circ}\text{C}$  in an oven for over 6 h. The cured PDMS was removed slowly and carefully from the petri dish, cleaned with Soxhlet extraction in hexane for 6 h to remove low molecular weight PDMS, and rinsed with ethanol and water. The blank PDMS was cut into  $1 \times 1$   $\text{cm}^2$  squares and stored under vacuum.

### **3.5.4 Silicon Wafer Cleaning and Preparation**

By using a Disco DAD 321 dicing saw, silicon wafers were cut into  $1 \times 1 \text{ cm}^2$  squares. After being sonicated in 2-propanol for 15 min and dried with a nitrogen gas stream, each chip underwent a standard RCA cleaning procedure: the chips were immersed in a base solution [ $\text{H}_2\text{O}/30\% \text{ NH}_4\text{OH (aq)}/30\% \text{ H}_2\text{O}_2 \text{ (aq)}$  (6:1:1)] at  $80 \text{ }^\circ\text{C}$  for 15 min, rinsed with water, and then immersed in an acid solution [ $\text{H}_2\text{O}/37\% \text{ HCl (aq)}/30\% \text{ H}_2\text{O}_2 \text{ (aq)}$  (5:1:1)] at  $80 \text{ }^\circ\text{C}$  for another 15 min. The chips were rinsed with water and dried in a stream of nitrogen gas.

### **3.5.5 Gold Dewetting on Si wafers or PDMS**

The sputtering system, ATC Orion 8 (AJA International Inc.) was used to deposit the gold films onto silicon wafers or the blank PDMS at room temperature. The working argon gas (99.99% purity) pressure was 4 mTorr. The sputtering powers were fixed to 100 W and 150 W, and the deposition rates were 0.16 and 0.22 nm/s, respectively. Afterwards, thermal treatment at  $150 \text{ }^\circ\text{C}$  for 20 h of the deposited thin gold films on silicon wafers or PDMS substrates was carried out in an oven to induce dewetting, and then allowed to cool to room temperature.

### **3.5.6 Plasmonic Stamping on Hydride-Terminated Silicon Surfaces**

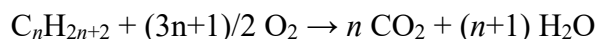
The cleaned silicon chips were immersed in degassed 40%  $\text{NH}_4\text{F}$  for 5 min and deoxygenated water for 10 s, respectively. After being dried with an argon stream, each chip was transferred immediately into an argon-filled glovebox ( $\text{O}_2$  and  $\text{H}_2\text{O} < 1 \text{ ppm}$ ) and placed into a customized sample holder. Typically, neat 1H,1H,2H-perfluoro-1-decene (30  $\mu\text{L}$ ) was dropped onto the hydride-terminated Si(111) surface and covered by the plasmonic stamp with the side containing the gold nanoparticles facing the Si surface. Then, a quartz slip was then placed onto the plasmonic stamp. Two bulldog clamps were applied on both sides to fix the sandwich structure and apply reproducible pressure. White light (150 W bulb) was focused through a periscope convex (PCX) lens, filtered through a bandpass filter (CW526), and shone onto the sandwiched

sample for various minutes with an incident intensity of 50 mW/cm<sup>2</sup>. Upon completion of the reaction, the wafer was rinsed with dichloromethane repeatedly and dried with argon gas. The wafers were immediately subjected to water contact angle measurements or XPS analyses.

# Chapter 4 Pd-Pt@void@ZrO<sub>2</sub> Yolk-Shell Nanoparticles for Wet Methane Combustion

## 4.1 Introduction

Natural gas is an abundant fossil fuel, with a total proven worldwide reserve of over 193.9 trillion cubic meters; it is of interest due to its lower emissions upon combustion, compared to gasoline and diesel.<sup>165, 166, 167, 168</sup> The main component of natural gas is methane, which has the lowest carbon/hydrogen ratio among all kinds of hydrocarbon fuels, thus, methane combustion generates the lowest amount of CO<sub>2</sub> per unit of energy released. Notably, methane itself is the second most significant greenhouse gas of all greenhouse gases after CO<sub>2</sub>,<sup>169, 170, 171, 172, 173</sup> with a global warming potential of 23 times higher than that of CO<sub>2</sub>; therefore, the release of unburned methane during combustion is a serious environmental concern. The use of heterogeneous catalysts enables methane oxidation at lower temperatures, compared to conventional thermal combustion (up to 1600 °C).<sup>174, 175</sup> The equation for alkane oxidation is:



Among alkanes, CH<sub>4</sub> has the strongest C–H bonds (450 kJ/mol),<sup>176, 177, 178</sup> thus, this molecule is difficult to oxidize catalytically. Platinum group metals (such as Pd, Pt, Rh, Au) and transition metal oxides (such as Mn, Cr, Cu, Co oxides) have been studied extensively for catalytic combustion.<sup>179, 180, 181, 182, 183</sup> In the operating conditions of the catalytic converter (i.e., in the presence of abundant oxygen, since complete combustion of unburned methane favors lean operation conditions), Pd catalysts have the highest activity. The proposed mechanism for Pd catalyzed methane combustion is as follows: CH<sub>4</sub> oxidation at low temperatures was reported to follow a Mars–van Krevelen redox mechanism and involve the activation of CH<sub>4</sub> on site pairs consisting of Pd-PdO<sub>x</sub> crystallites. In these pairs, Pd acts as an oxygen vacancy and PdO<sub>x</sub> provides the oxygen atoms. CH<sub>4</sub> is adsorbed and dissociated on metallic Pd producing H and CH<sub>x</sub> species; while the oxidation takes place on the adjacent PdO.<sup>184</sup> Although Pd shows high initial activity, it tends to deactivate under exhaust conditions mainly due to thermal and hydrothermal-induced sintering of the Pd nanoparticles,<sup>185–188</sup> which is

one major challenge in the development of stable combustion catalysts for automotive catalytic converters. This factor, coupled with a four-fold rise in the price of Pd in the last decade,<sup>189</sup> means that a stable and economically viable catalyst to efficiently combust methane is of great need.

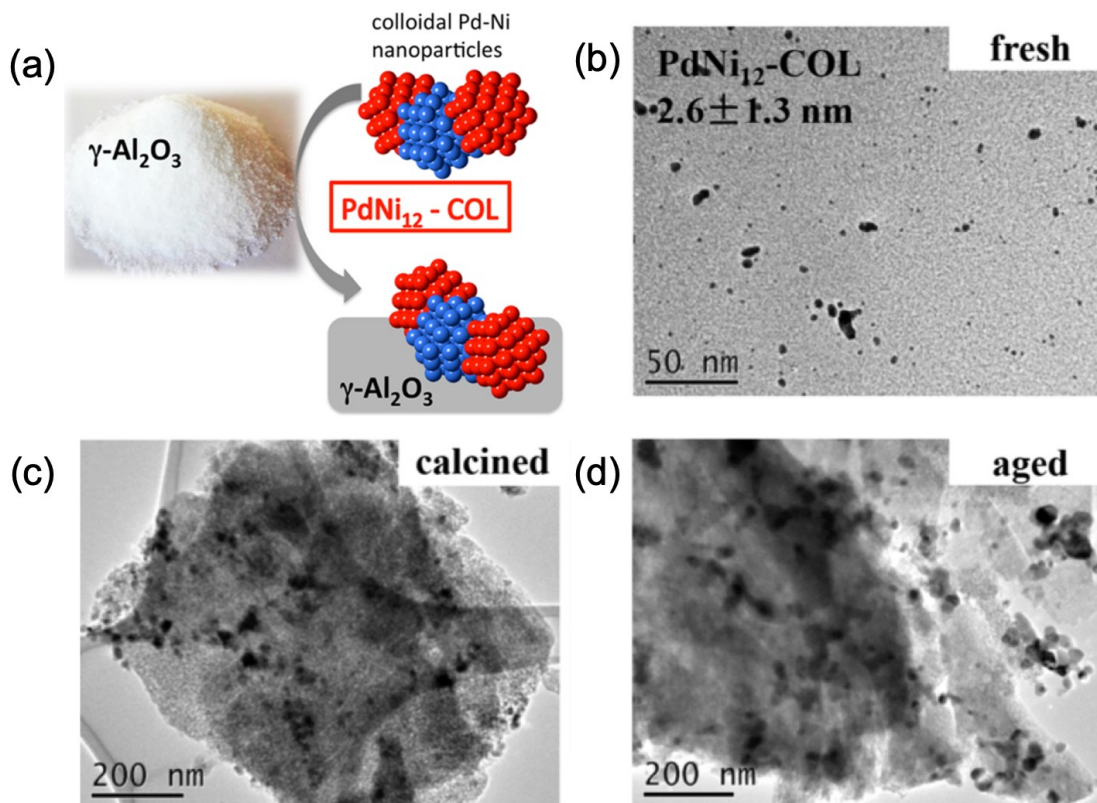
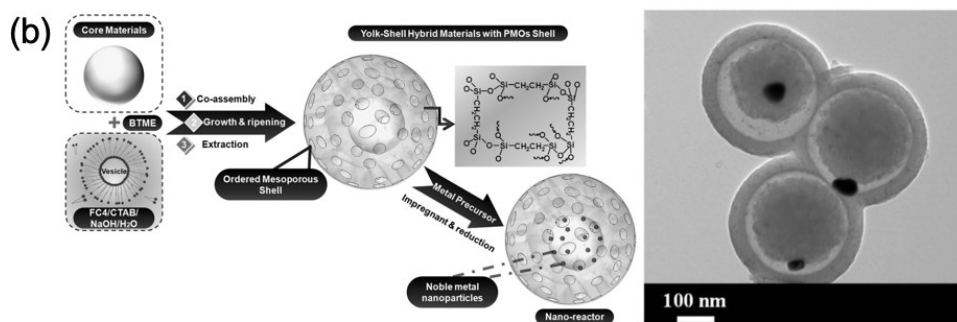
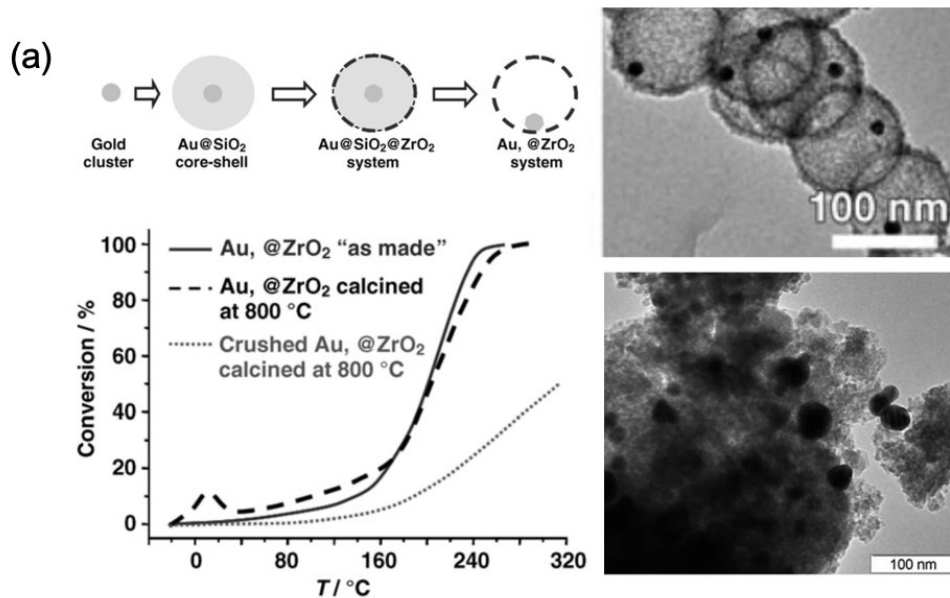


**Figure 4.1** (a) Schematic of Pd-Ni bimetallic catalyst preparation via colloidal techniques (PdNi<sub>12</sub>-COL). (b) TEM images of the PdNi<sub>12</sub>-COL catalyst: nanoparticles before deposition on the support (“fresh”); (c) after deposition and calcination for 16 h at 550 °C (“calcined”), and after hydrothermal aging (methane combustion) for 40 h (“aged”). Reproduced with permission from reference 190. Copyright 2015 American Chemical Society.

One widely used strategy to form heterogeneous catalysts is to deposit metal nanoparticles, such as metal oxides,<sup>191</sup> zeolites,<sup>192</sup> carbon,<sup>193</sup> etc., on a catalyst support. Although it is theoretically possible to optimize the catalytic activity and improve the stability, in practice, nanoparticles may evolve during catalysis, adopt low-energy shapes, and grow by agglomeration, leading to a significant loss of activity.<sup>194–196</sup> To solve these problems, researchers have tried either to add different elements to the metal nanoparticles or to modify the catalyst support by surface functionalization,<sup>197–200</sup> but

metal nanoparticles atop the support surface are still prone to agglomeration and sintering. For example, Shen et al.<sup>190</sup> synthesized Pd-Ni bimetallic nanoparticles and then deposited them onto a commercial  $\gamma$ -Al<sub>2</sub>O<sub>3</sub> support as a catalyst for methane combustion (synthetic scheme is shown in Figure 1a). The initial size of the Pd-Ni nanoparticles is 2.6 nm (Figure 1b). The TEM images in Figures 1c and 1d are the Pd-Ni nanoparticles on the Al<sub>2</sub>O<sub>3</sub> support after calcination for 16 h at 550 °C and the used catalyst after hydrothermal aging for methane combustion, respectively. It can be seen clearly that the size of the nanoparticles becomes much larger due to thermal agglomeration, compared to the freshly prepared Pd-Ni bimetallic nanoparticles in Figure 1b. The author used a larger (200 nm) scale bar in Figure 1c and 1d and a smaller (50 nm) scale bar in Figure 1b.

Another route towards stabilization of catalysts<sup>201, 202, 203, 204, 205, 206</sup> is based on the concept of an “inverted” metal-support structure: the support material forms a porous nanoshell around the active metal nanoparticles. The reason is that the porous nanoshells can isolate nanoparticles and suppress agglomeration, while permitting gaseous molecules to access the active sites on the metal nanoparticles. A series of core-shell nanostructures have been screened for methane combustion by other groups, including Pd@SiO<sub>2</sub>,<sup>207–209</sup> Pd@CeO<sub>2</sub>,<sup>210, 211</sup> and Pd@ZrO<sub>2</sub>.<sup>212, 213</sup> (note that with the nomenclature, Y@MO<sub>x</sub>, the metal nanoparticle cores, Y, are encapsulated by the metal oxide shell, MO<sub>x</sub>). Among more complex nanostructures, yolk shell (core@void@shell) nanoparticles are recognized as a promising catalyst candidate because this nanostructure has shown catalytic activity for many different varieties of reactions.<sup>214–218</sup>



Substrates	Products	RT <sup>b)</sup> [°C]	Time [h]	Conversion [%]
		50	8	94
		50	8	92
		50	8	100
		50	8	100
		50	8	53

Figure 4.2 Catalytic oxidation reactions by yolk-shell nanoparticles. (a) Au@void@ZrO<sub>2</sub> nanoparticles were synthesized and tested for CO oxidation. (b) Pd yolk-shell nanoparticles with an outer shell based on periodic mesoporous organosilica were synthesized for the selective oxidation of various alcohol substrates. Reproduced with permission from reference 219 and 220. Copyright 2006, 2012 Wiley-VCH.

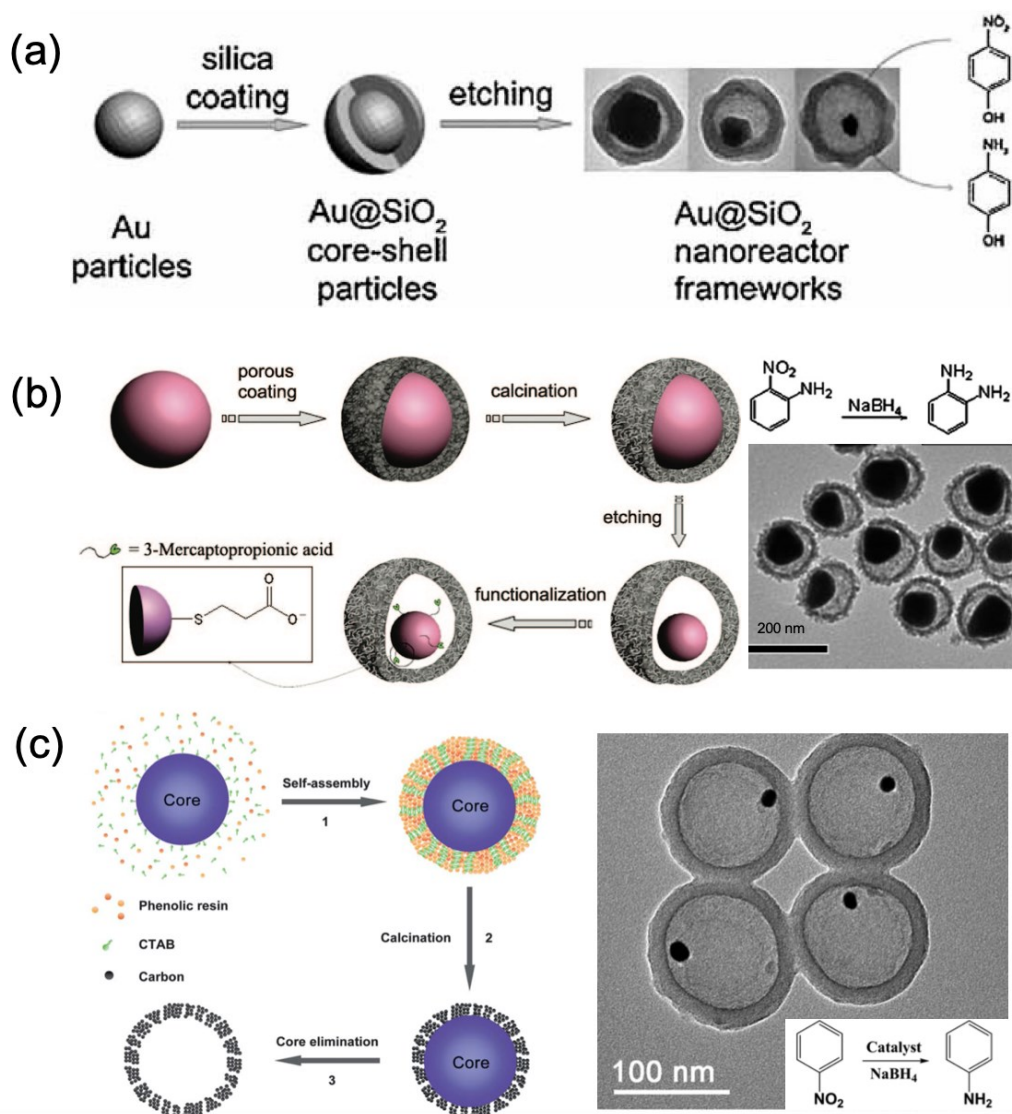


Figure 4.3 Catalytic reduction reactions by yolk-shell nanoparticles (a) The Au@SiO<sub>2</sub> yolk-shell nanostructure was synthesized by selective etching of the gold cores in Au@SiO<sub>2</sub> core-shell particles. This nanoreactor system was used to catalyze the reduction of *p*-nitrophenol. (b) The gold cores of Au@SiO<sub>2</sub> yolk-shell catalysts were functionalized selectively by the addition of 3-MPA, which generated carboxylate anions on the surface. It was a very effective means of increasing the reaction rates of 2-nitroaniline reduction. (c) Au@carbon yolk-shell nanoparticles were synthesized as the catalyst for hydrophobic nitrobenzene reduction. Reproduced with permission from reference 221, 222, and 223. Copyright 2008 Wiley-VCH, Copyright 2008 American Chemical Society, and Copyright 2013 Royal Society of Chemistry, respectively.

One classical example was reported by Schüth in 2006; Au@void@ZrO<sub>2</sub> yolk shell nanoparticles were synthesized for CO oxidation.<sup>219</sup> The plots showing CO oxidation (Figure 4.2a, left) reveal that when the Au nanoparticles are encapsulated within the ZrO<sub>2</sub> shell, the temperature for 50% CO conversion is about 200 °C. However, when the yolk-shell structures were crushed by ball-milling for 2 h, the catalytic performance reduced significantly, resulting in low reactivity of 10% CO conversion at 200 °C due to the growth of the gold particles through a thermal sintering process, as shown in the TEM image (Figure 4.2a, right); the hollow, porous zirconia outer shell is indeed advantageous for the thermal stabilization of the catalysts as it separates the metal nanoparticles and prevents agglomeration. Since this landmark paper, this yolk-shell nanostructure has been tested extensively for a range of reactions, including the catalytic oxidation of alcohols (Figure 4.2b)<sup>220</sup> and the reduction of *p*-nitrophenol,<sup>221, 224, 225</sup> 2-nitroaniline,<sup>222, 226, 227</sup> and nitrobenzene,<sup>223, 228, 229</sup> (Figure 4.3a, b, c), but to the best of our knowledge, it has not been reported yet for methane combustion. By using yolk-shell nanoparticles for methane combustion, the problems of agglomeration of the active metal nanoparticle core could be avoided.

ZrO<sub>2</sub> was chosen as the outer shell material, and Pd-Pt bimetallic nanoparticles as the core in the architecture tested here. To mimic the combustion conditions in lean-burn natural gas exhaust, the yolk-shell nanoparticles were tested for methane combustion in the presence of 5 mol% water in the feed.<sup>230</sup> Prior work pointed to the utility of the choice of ZrO<sub>2</sub> for the metal oxide, ZrO<sub>2</sub> showed stable activity during reaction in the presence of water vapor,<sup>231</sup> whereas other metal oxide supports showed deactivation in the presence of water vapor (Al<sub>2</sub>O<sub>3</sub>, TiO<sub>2</sub>, and SnO<sub>2</sub>)<sup>232–234</sup> The earlier examples of yolk-shell ZrO<sub>2</sub> structures pointed to pore sizes of ~5 nm,<sup>219, 235</sup> which is permeable to the passage of gases. While previous work immobilized monometallic nanoparticles inside the ZrO<sub>2</sub> yolk shell structure,<sup>236</sup> we examined the use of bimetallic Pd-Pt nanoparticles because other work had shown that Pd catalysts improved considerably by addition of Pt to Pd.<sup>237–239</sup> Recently, Nassiri et al.<sup>240</sup> showed an improvement of the activity of Pd-Pt catalysts, compared to monometallic Pd in wet methane combustion conditions, and a Pd/Pt molar ratio of 1 was reported to show the most stable performance. The addition of Pt to a Pd system is to increase activity and

also to improve the thermal durability in the combustion of methane.<sup>241</sup> The effect of Pt on the performance of Pd catalysts is still debated and can be explained in terms of electronic and geometric effects, synergistic effect, and/or presence of mixed sites.<sup>242</sup> Moreover, the Pd nanoparticles are reported to have the highest methane combustion turnover frequencies at a particle size of 8 to 10 nm.<sup>179, 207, 208</sup> Thus, in our study, 8 nm Pd-Pt bimetallic nanoparticles with a 1:1 molar ratio were selected as the core for the yolk-shell nanoparticles.

Herein, we report the preparation of Pd-Pt@void@ZrO<sub>2</sub> yolk shell nanoparticles (1:1 molar ratio of Pd to Pt) and Pd-Pt@ZrO<sub>2</sub> (1:1 molar ratio of Pd to Pt) core-shell nanoparticles, which were tested for wet methane combustion. The catalytic lifetimes of the encapsulated catalysts were evaluated by hydrothermal ageing tests and compared with non-yolk-shell Pd/Pt@ZrO<sub>2</sub> materials. Our study shows the advantages and limitations of the yolk-shell nanoparticles for methane combustion by a comparison with core-shell nanoparticles and classical impregnated catalysts.

## 4.2 Results and Discussion

### 4.2.1 Synthesis of Pd-Pt@void@ZrO<sub>2</sub> Yolk-Shell Nanoparticles

The Pd-Pt nanoparticles were prepared by a reported method.<sup>243</sup> Briefly, a 1:1 molar ratio of potassium tetrachloroplatinate (K<sub>2</sub>PtCl<sub>4</sub>, aqueous solution) and sodium tetrachloropalladate (Na<sub>2</sub>PdCl<sub>4</sub>, aqueous solution), polyvinylpyrrolidone (PVP), an aqueous solution of sodium iodide (NaI), and N, N-dimethylformamide (DMF) were mixed in a capped vial. After the mixture was ultrasonicated for about 2 min, the resulting homogeneous mixture was transferred into a conventional oven, heated at 130 °C for 5 h, and then cooled to room temperature. The resulting colloidal products were collected by centrifugation and washed with acetone. The representative transmission electron microscope (TEM) of the colloidal products are shown in Figure 4.4a and Figure 4.5a. The typical TEM images show that the product consisted of uniform cubic nanoparticles, with an average edge length of  $8.0 \pm 1.3$  nm according to the size distribution. A high-resolution TEM (HRTEM) image in Figure 4.4a shows that it is a single crystal with well-defined fringes, and the lattice spacing along the edge of the nanocube is 0.19 nm. We characterized the Pd-Pt nanoparticles by energy-

dispersive X-ray spectroscopy (EDX) analyses, and the compositional images (Figure 4.4b) and spectra (Figure 4.4c) of Pd and Pt suggested that it was a Pd<sub>50.6</sub>-Pt<sub>49.4</sub> alloy, with a homogeneous distribution of the Pd and Pt, which agrees well with the reported result.<sup>243</sup> This value was in good agreement with the Pt/Pd atomic ratio of the initial reaction precursors, suggesting that the Pt and Pd precursors were reduced completely and taken up in the product.

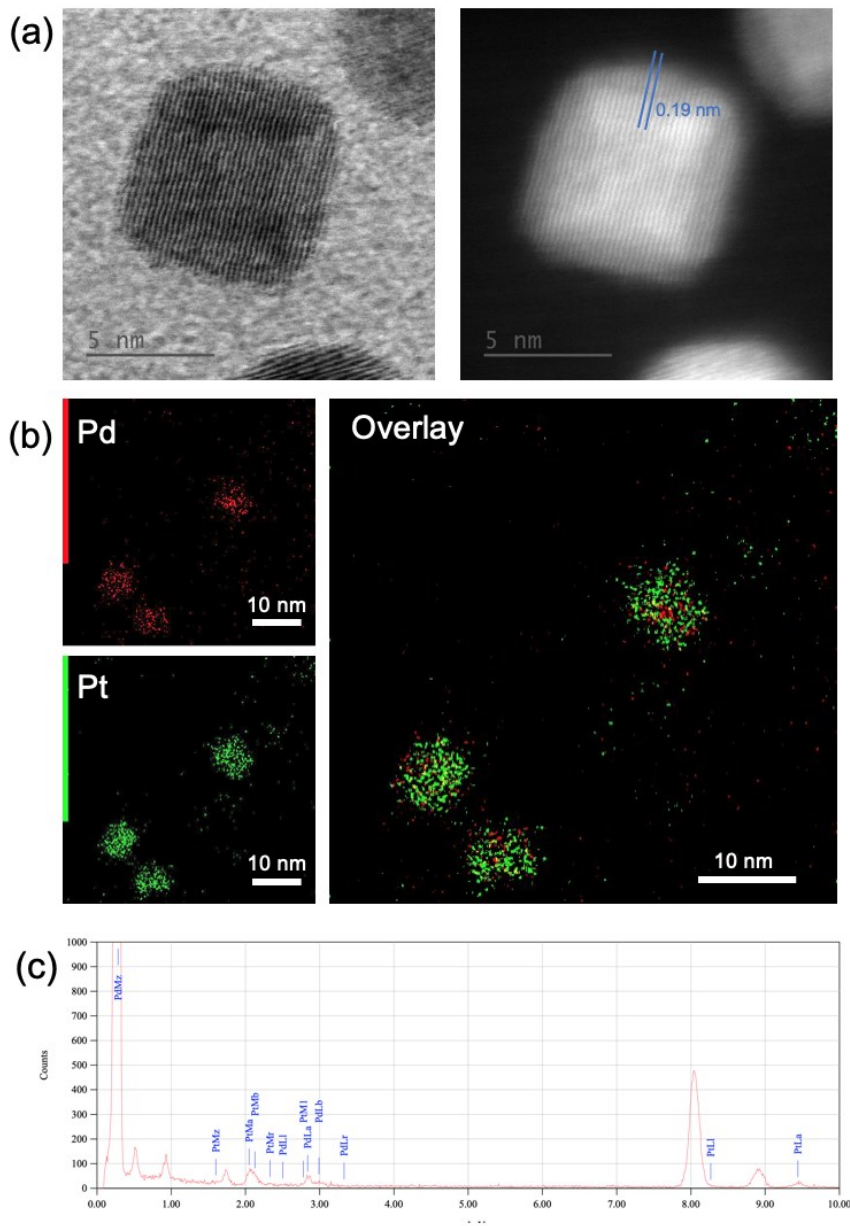


**Figure 4.4** (a) S/TEM images of the cubic Pd-Pt nanoparticles. (b) EDX images for Pd-Pt nanoparticles, and corresponding EDX spectrum (c) for Pd, Pt element quantification.

In the next step, the as-prepared Pd-Pt nanoparticles were encapsulated by a silica shell by the Stöber process for the synthesis of silica spheres.<sup>244</sup> The TEM images of as-synthesized Pd-Pt@SiO<sub>2</sub> obtained under optimized experimental conditions (Pd-Pt colloid/tetraethylorthosilicate, TEOS = 1:20), where each Pd-Pt nanoparticle is encapsulated by a silica layer, are shown in Figure 4.5b. The average diameter of the Pd-Pt@SiO<sub>2</sub> was 204 ± 44 nm, which was estimated by the size distribution histogram.

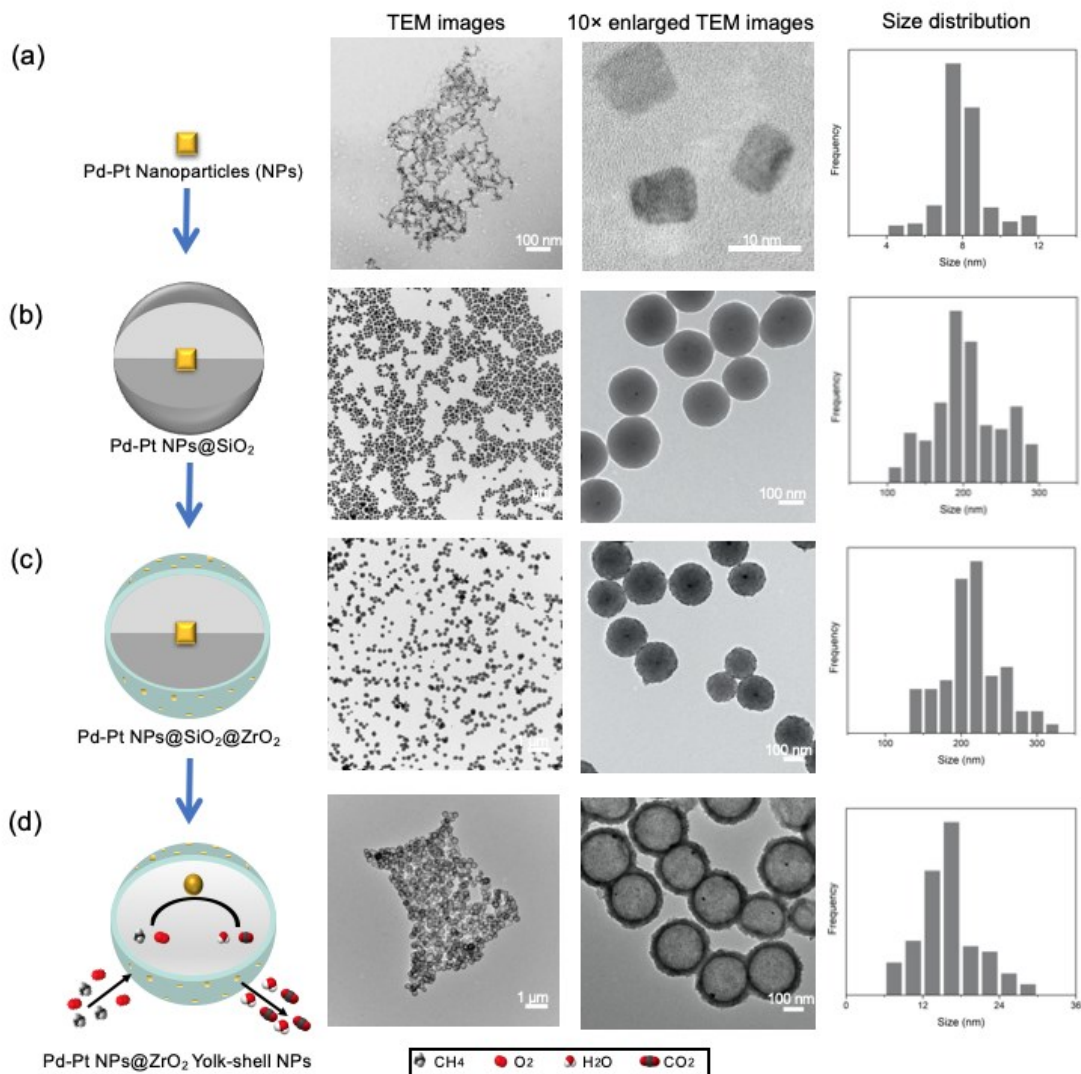
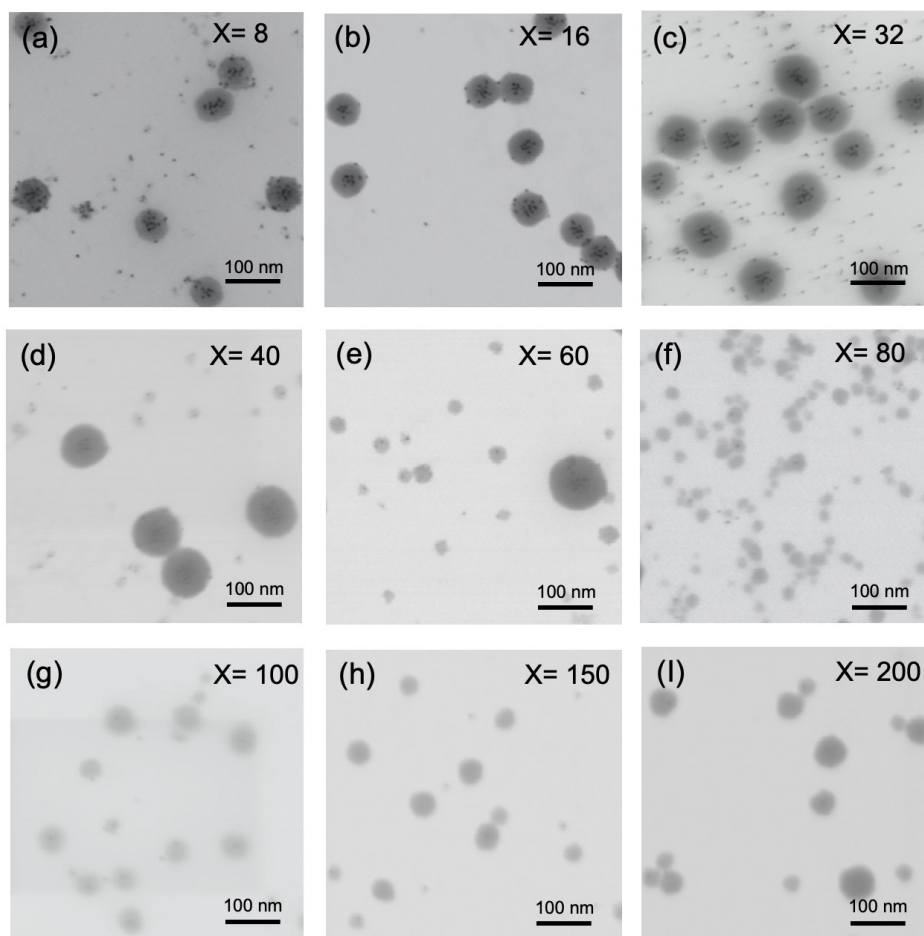


Figure 4.5 From left to right, schematic figures, TEM images, 10× enlarged TEM images and size distribution histograms for (a) Pd-Pt nanoparticles; (b) Pd-Pt nanoparticles@SiO<sub>2</sub>; (c) Pd-Pt nanoparticles@SiO<sub>2</sub>@ZrO<sub>2</sub>; (d) Pd-Pt nanoparticles@void@ZrO<sub>2</sub>. Notably, for the size distribution histograms, from top to bottom, is the diameter of (a) Pd-Pt nanoparticles; (b) Pd-Pt nanoparticles@SiO<sub>2</sub>; (c) Pd-Pt nanoparticles@SiO<sub>2</sub>@ZrO<sub>2</sub>; and ZrO<sub>2</sub> shell thickness of (d) Pd-Pt nanoparticles@void@ZrO<sub>2</sub>.

The configuration of core shell nanoparticles was tuned by changing the amount of the silica source (TEOS).<sup>245</sup> If the amount of TEOS was decreased compared with the amount required for the optimized condition, the silica shell contained multiple Pd-Pt particles, as shown in Figures 4.6a–e; Increasing the amount of TEOS resulted in the formation of a mixture of Pd-Pt@SiO<sub>2</sub> and amorphous silica particles without any cores (Figure 4.6f–i).



**Figure 4.6** TEM images for TEOS/Pd-Pt ratio control experiments, Pd-Pt@SiO<sub>2</sub> core-shell nanoparticles synthesized under lower amounts of TEOS (TEOS volume, X < 60  $\mu$ L): the silica shell contained multiple Pt particles; higher (TEOS volume, X > 80  $\mu$ L) amounts of TEOS: a mixture of Pd-Pt@SiO<sub>2</sub> and silica particles without cores; compared to the Pd-Pt@SiO<sub>2</sub> nanoparticles synthesized under the optimum TEOS amounts (X = 70  $\mu$ L) shown in Figure 4.5b, where each Pt particle is encaged within a silica shell. Reaction conditions: 10 mL PVP-stabilized Pd-Pt dispersed in EtOH, 0.5 mL NH<sub>4</sub>OH, 0.9 mL water, X  $\mu$ L TEOS, continued by stirring at room temperature for 24 h. No centrifugation or other purification.

Prior to encapsulating the Pd-Pt@SiO<sub>2</sub> with ZrO<sub>2</sub>, the as-prepared Pd-Pt@SiO<sub>2</sub> nanoparticles needed to be washed with water and absolute ethanol sequentially. If only washed with water, ZrO<sub>2</sub> was not deposited onto the SiO<sub>2</sub> surface in a conformal fashion, as the zirconium butoxide hydrolysis process is affected strongly by the water/Zr source ratio and pH value.<sup>246-248</sup> On the right side of this TEM image in Figure 4.7, there are some Pd-Pt@SiO<sub>2</sub> nanoparticles without ZrO<sub>2</sub> coating; the surfaces are very smooth, compared to the rough surface of Pd-Pt@SiO<sub>2</sub>@ZrO<sub>2</sub> shown in Figure 4.5c. As described in previous work, a surfactant is needed, thus, Lutensol AO5 (BASF) was used.<sup>219, 236</sup> Here, Lutensol XP50 (BASF) coats the Pd-Pt@SiO<sub>2</sub> nanoparticle surfaces, followed by reaction with zirconium butoxide, and then calcined at 600 °C to produce a shell of porous zirconia; the diameter of the particles increases from 204 ± 44 nm to 221 ± 48 nm, as shown in Figure 4.5c.

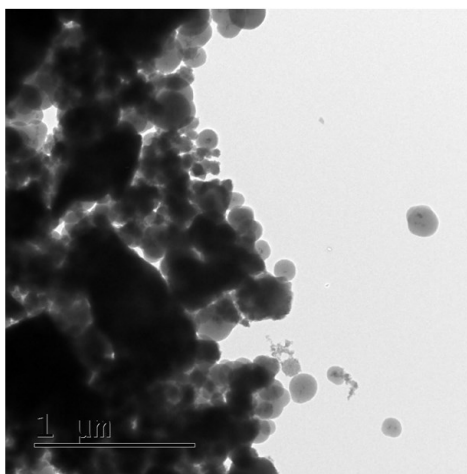


**Figure 4.7** Before ZrO<sub>2</sub> encapsulation, as-prepared Pd-Pt@SiO<sub>2</sub> nanoparticles need to be washed with water and absolute ethanol, respectively. If only washed with water, ZrO<sub>2</sub> will not be encapsulated onto the SiO<sub>2</sub> surface as shown in the TEM image.

Notably, when using a lower amount of zirconium butoxide than the optimized amount, the ZrO<sub>2</sub> shell is very thin and the Pd-Pt nanoparticles are released from the yolk-shell nanostructure (Figure 4.8).

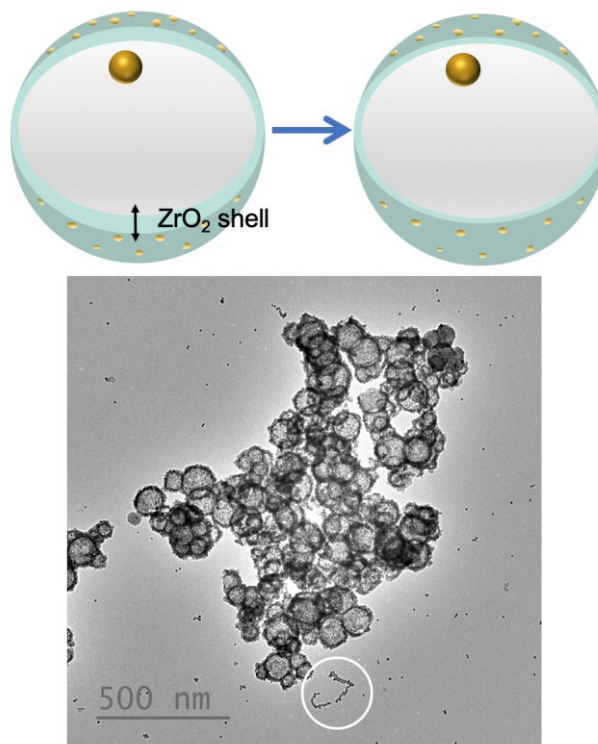


**Figure 4.8** When using a lower amount of zirconium butoxide than the optimized amount, the shell of  $ZrO_2$  is very thin, and some Pd-Pt nanoparticles are released from the yolk-shell nanostructures (highlighted in the white circle).

Finally, the silica shell was removed via dissolution with a NaOH solution to form the Pd-Pt@void@ $ZrO_2$  yolk-shell structures (Figure 4.5d). At this point, the Pd-Pt nanoparticles ‘rattle’ within the empty  $ZrO_2$  shell and can be observed by TEM on the inner side of the  $ZrO_2$  shell. Once the  $SiO_2$  shell has been removed, the yolk-shell structure is very fragile and is fractured upon sonication for 5 min (Figure 4.9). According to the histogram in Figure 4.5d, the thickness of the porous zirconia shell is  $16 \pm 4$  nm, which agrees well with a 17-nm size increment from Pd-Pt@ $SiO_2$  (204 nm) to Pd-Pt@ $SiO_2$ @ $ZrO_2$  (221 nm).

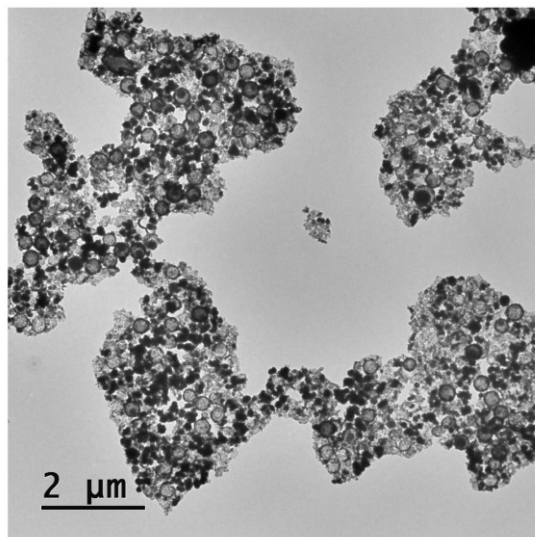


**Figure 4.9** Observed fracturing of the Pd-Pt@void@ZrO<sub>2</sub> yolk-shell nanoparticles upon sonication for 5 min in a water solution.

#### **4.2.2 Testing of Pd-Pt on ZrO<sub>2</sub> for Wet Methane Combustion**

In the past, tremendous efforts have been made to develop catalysts with superior catalytic activity, which enable full methane conversion below 450 °C. For example, a Pd/Co/Al<sub>2</sub>O<sub>3</sub> catalyst prepared by a galvanic deposition (Figure 4.10a) exhibited full methane combustion at 450 °C,<sup>249</sup> but the catalytic lifetime of the catalyst was not investigated. Another recent example is a Al<sub>2</sub>O<sub>3</sub>/Pd/SiO<sub>2</sub> catalyst that was prepared by an atomic layer deposition method; this catalyst delivered full methane conversion below 400 °C, and remained stable for only five full combustion cycles (Figure 4.10b).<sup>250</sup> Noble metal/metal oxide yolk-shell structured nanoparticles have been exploited for catalytic applications, including gas phase and liquid phase reactions, as outlined earlier. Here we expand its application for methane combustion. To confirm that the ZrO<sub>2</sub> shell we prepared permits diffusion of gases, we carried out gas adsorption isotherms, Brunauer–Emmett–Teller (BET), and Barrett–Joyner–Halenda (BJH) model analyses of N<sub>2</sub> adsorption isotherms (Figure 4.11a and Table 4.1), which showed a surface area of 316.3 m<sup>2</sup>/g, and an average pore size of 5.6 nm.

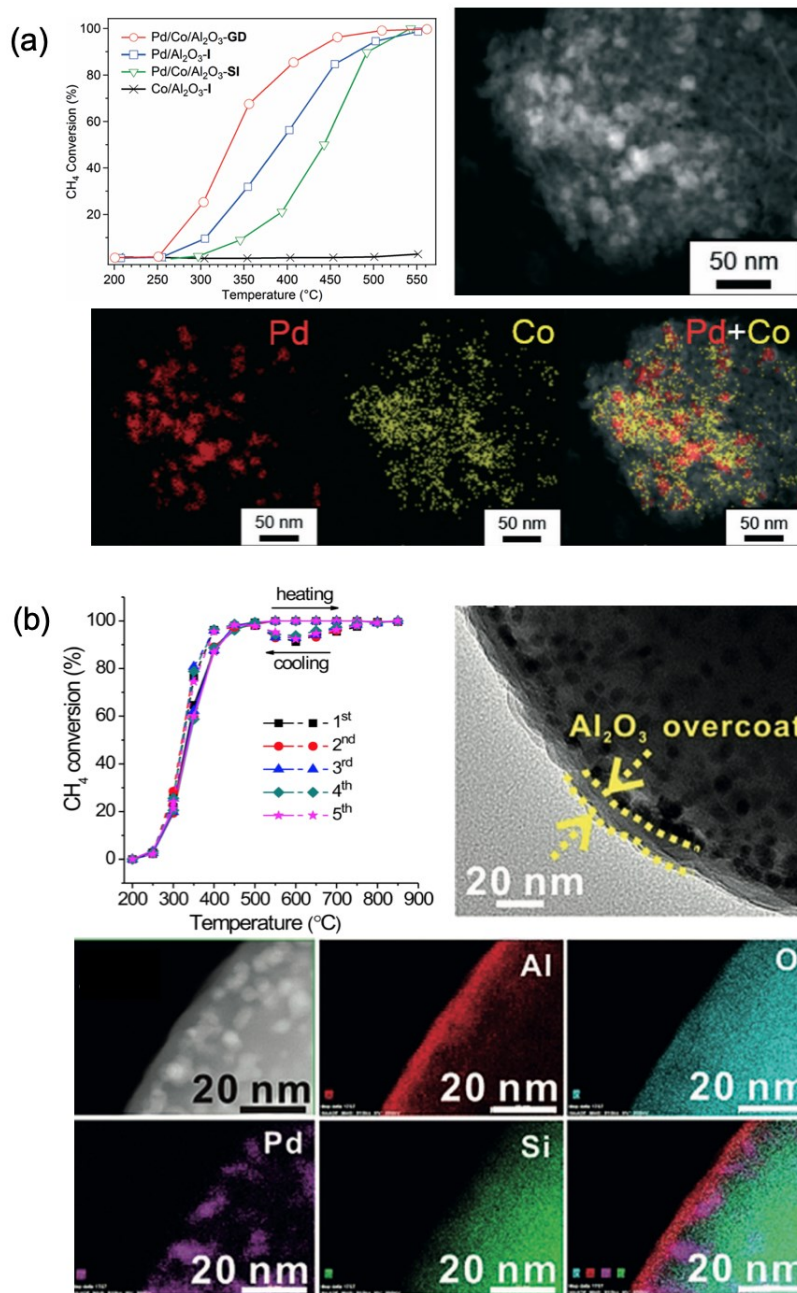
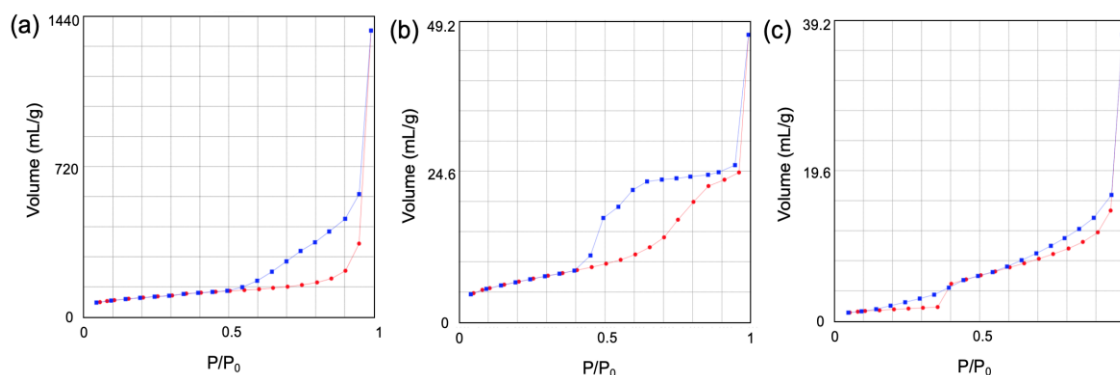


Figure 4.10 (a) TEM images and EDX mapping images for Pd/Co/Al<sub>2</sub>O<sub>3</sub> catalyst, synthesized by galvanic displacement. By comparing catalytic activity of methane combustion with Pd/Co/Al<sub>2</sub>O<sub>3</sub> impregnated catalyst, methane combustion over Pd/Co/Al<sub>2</sub>O<sub>3</sub>-GD (galvanic displacement) proceeded at a temperature about 50 °C lower than that over impregnated catalyst. Reproduced with permission from reference 45 (Copyright 2016 Royal Society of Chemistry). (b) TEM images and EDX mapping images of Al<sub>2</sub>O<sub>3</sub>/Pd/SiO<sub>2</sub> catalyst, prepared by an atomic layer deposition method. Ignition–extinction curves show the catalyst delivered full methane conversion at 400 °C and maintained its activity during the five cycles. Reproduced with permission from reference 250. Copyright 2019 Wiley-VCH.



**Figure 4.11** Nitrogen adsorption (red) and desorption (blue) isotherms for (a) Pd-Pt@void@ZrO<sub>2</sub> yolk-shell nanoparticles, (b) Pd-Pt@ZrO<sub>2</sub> directly, (c) Pd-Pt/ZrO<sub>2</sub> impregnated catalyst.

**Table 4.1** Pd, Pt Contents, Pd/Pt Molar Ratio, Size of Pd-Pt Nanoparticles, BET Surface Area and BJH Pore Size from Three As-prepared Catalysts.

Catalyst	Pd loading (wt%)	Pt loading (wt%)	Pd/Pt molar ratio	Size of Pd-Pt nanoparticles	BET surface area (m <sup>2</sup> g <sup>-1</sup> )	BJH Pore size (nm)
Pd-Pt@void@ZrO <sub>2</sub>	0.57	0.90	53.8:46.2	8.0 ± 1.3 nm	316.3	5.6
Pd-Pt@ZrO <sub>2</sub>	0.59	0.95	53.2:46.8	8.0 ± 1.3 nm	23.57	3.8
Impregnated Pd-Pt/ZrO <sub>2</sub>	0.61	1.00	53.0:47.0	7.7 ± 5.0 nm	5.24	3.0

As a comparison, two related sets of heterogeneous catalysts were synthesized, Pd-Pt@ZrO<sub>2</sub> and Pd-Pt/ZrO<sub>2</sub> impregnated catalysts. Briefly, Pd-Pt@ZrO<sub>2</sub> nanoparticles were obtained by the hydrolysis of zirconium butoxide in the presence of the preformed Pd-Pt nanoparticles (the same Pd-Pt nanoparticles described previously for the synthesis of the yolk-shell nanoparticles). After calcination, the Pd-Pt nanoparticles were immobilized within porous ZrO<sub>2</sub>, shown in Figure 4.12. The pore size determined for these Pd-Pt@ZrO<sub>2</sub> nanoparticles is 3.8 nm, and the surface area is 23.57 m<sup>2</sup>/g, as shown by BJH and BET analyses, respectively (Figure 4.11b and table 4.1).

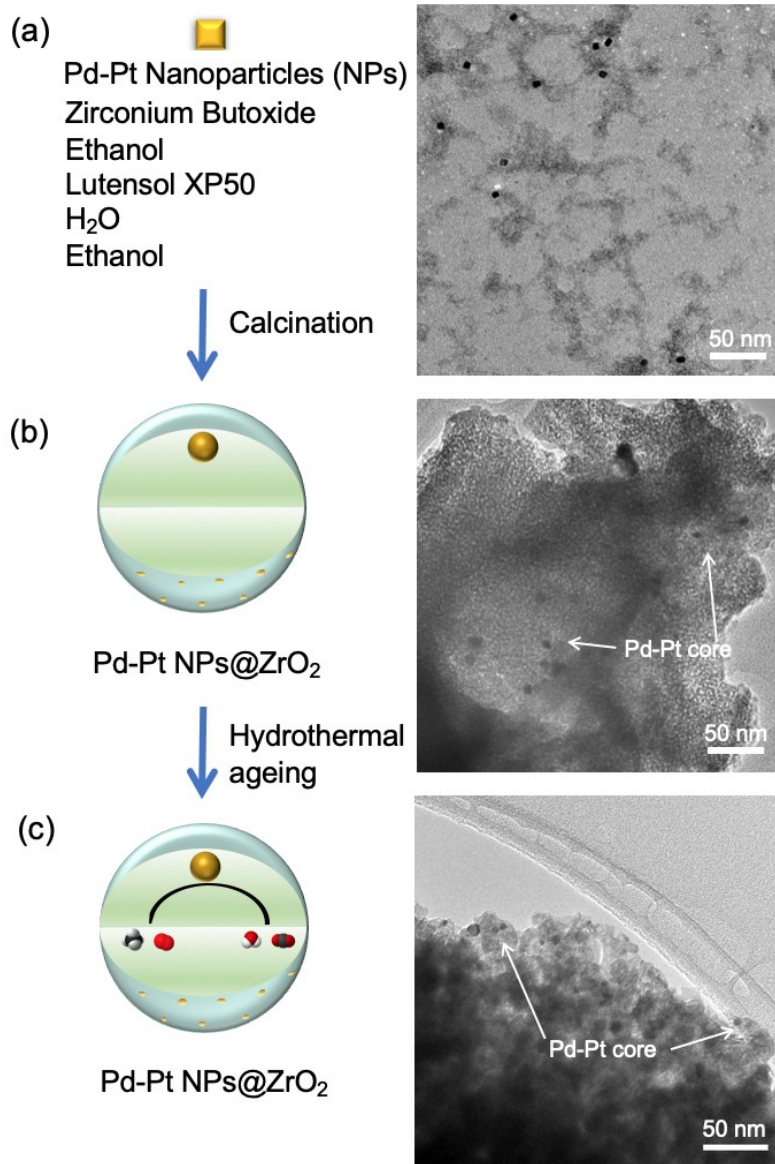


**Figure 4.12** TEM images of Pd-Pt@ZrO<sub>2</sub> core-shell nanoparticles. (a) Pd-Pt nanoparticles reacted with zirconium butoxide, Lutensol XP50, water, and ethanol. The Pd-Pt nanoparticles were synthesized using the same protocols as that of Pd-Pt@void@ZrO<sub>2</sub>, hence, Pd-Pt nanoparticles are of cubic shape, and the side length is ~8 nm in solution; (b) after calcination at 600 °C for 6 h, the shape of Pd-Pt nanoparticles changes from cube to sphere, size is still comparable, although some become bigger because of the thermal aggregation; (c) after 42 h hydrothermal ageing (methane combustion), Pd-Pt nanoparticles can be seen through the ZrO<sub>2</sub> shell. As the Pd-Pt nanoparticles are immobilized by the ZrO<sub>2</sub> shell, the size is still comparable, although some become bigger due to aggregation.

The other “control” catalyst architecture, the Pd-Pt impregnated onto a ZrO<sub>2</sub> support, was prepared via wet impregnation of palladium chloride and hexachloroplatinic acid in a 1:1 molar ratio onto a commercially obtained ZrO<sub>2</sub> support, as reported earlier.<sup>230</sup> As shown in Figure 4.13, Pd and Pt in the impregnated catalysts are observed to have formed bimetallic nanoparticles, as confirmed by EDX mapping, which is in agreement with the reported result.<sup>208</sup> The Pd-Pt nanoparticles ( $7.7 \pm 5.0$  nm) are, however, polydispersed (dispersity = 42%) and are scattered on the ZrO<sub>2</sub> surface. The surface area was determined to be 5.24 m<sup>2</sup>/g, revealing that the ZrO<sub>2</sub> is solid and not porous. (Figure 4.11c and Table 4.1).

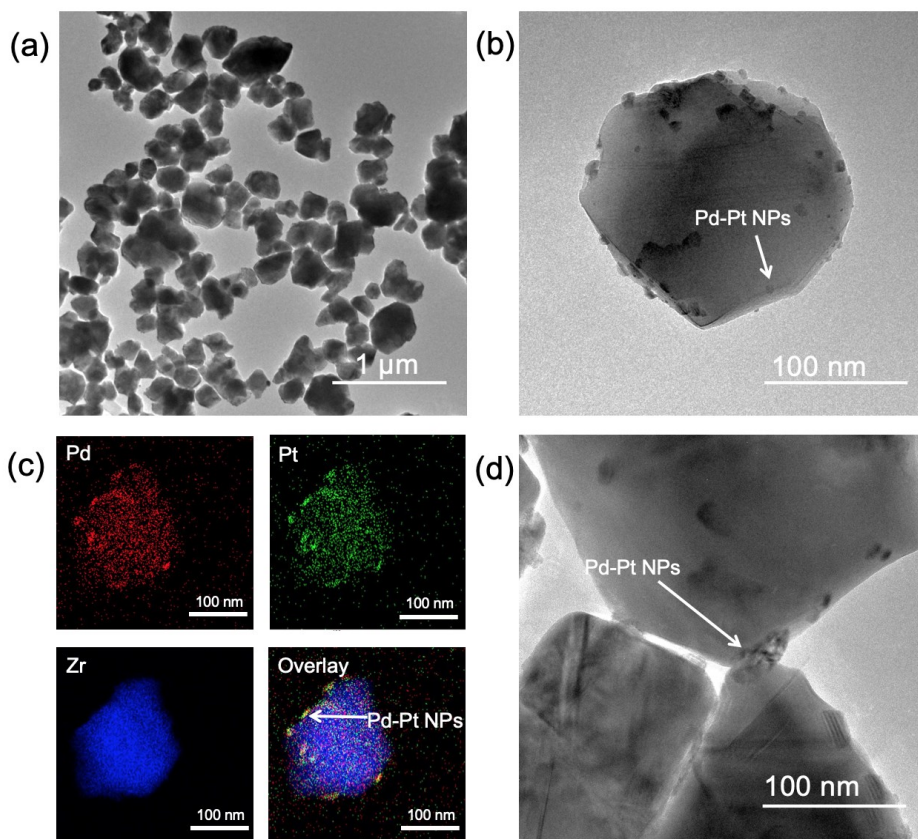


**Figure 4.13** TEM images (a), (b) and EDX mapping images (c) for prepared Pd-Pt/ZrO<sub>2</sub> impregnated catalysts. The size of Pd-Pt nanoparticles is  $7.7 \pm 5.0$  nm. The Pd and Pt elements are distributed all over the surface as there is no washing step for the conventional impregnation method, i.e., just calcination of the mix solution of palladium chloride, hexachloroplatinic acid with ZrO<sub>2</sub> powder. However, we can see Pd-Pt nanoparticles on the surface (white arrow), especially compared to the Zr element map. (d) TEM image for the used Pd-Pt/ZrO<sub>2</sub> impregnated catalyst after 42 h hydrothermal ageing (methane combustion). The average size of Pd-Pt nanoparticles is  $29.8 \pm 11.3$  nm.

Metal loading of each of these catalysts was measured by inductively coupled plasma-mass spectroscopy (ICP-MS) and is summarized in Table 4.1. The Pd/Pt molar ratio for the Pd-Pt@void@ZrO<sub>2</sub>, Pd-Pt@ZrO<sub>2</sub>, and Pd-Pt/ZrO<sub>2</sub> impregnated catalysts, are 53.8:47.2, 53.2:47.8, and 53.0:47.0, respectively, which are all consistent with the 1:1 molar ratio of Pd/Pt. The total Pd metal loading of these three catalysts is 0.57 %, 0.59 %, and 0.61 %, respectively.

The catalytic activities of these three nanoparticle formulations for the same Pd metal loading were assessed in wet lean methane combustion between 300 and 650 °C. The ignition-extinction curves (Figure 4.14b, c) show that the Pd-Pt/ZrO<sub>2</sub> impregnated catalyst and Pd-Pt@ZrO<sub>2</sub> catalysts exhibited a limited maximum conversion of ~65% at 650 °C, but the Pd-Pt@void@ZrO<sub>2</sub> (Figure 4.14a) showed a 100% conversion rate at the same temperature.

During hydrothermal ageing, the reactor temperature was increased to 650 °C and then reduced to 475 °C (with a holding time of 1 h at each step). The high-low temperature cycling was repeated eight times over about 22 h. After cycling was complete, the reactor temperature was held at 475 °C for another 20 h. Therefore, hydrothermal ageing was done for 42 h in total; these figures are shown on the right side of Figure 4.14. During the cycling at 650 and 475 °C for just 5 h, the Pd-Pt/ZrO<sub>2</sub> impregnated catalyst lost its activity significantly, i.e., the methane conversion rate at 475 °C decays to below 10% in 5 h. However, the Pd-Pt@void@ZrO<sub>2</sub> and Pd-Pt@ZrO<sub>2</sub> catalysts both maintain their activity for the entire hydrothermal aging test (up to 42 h).

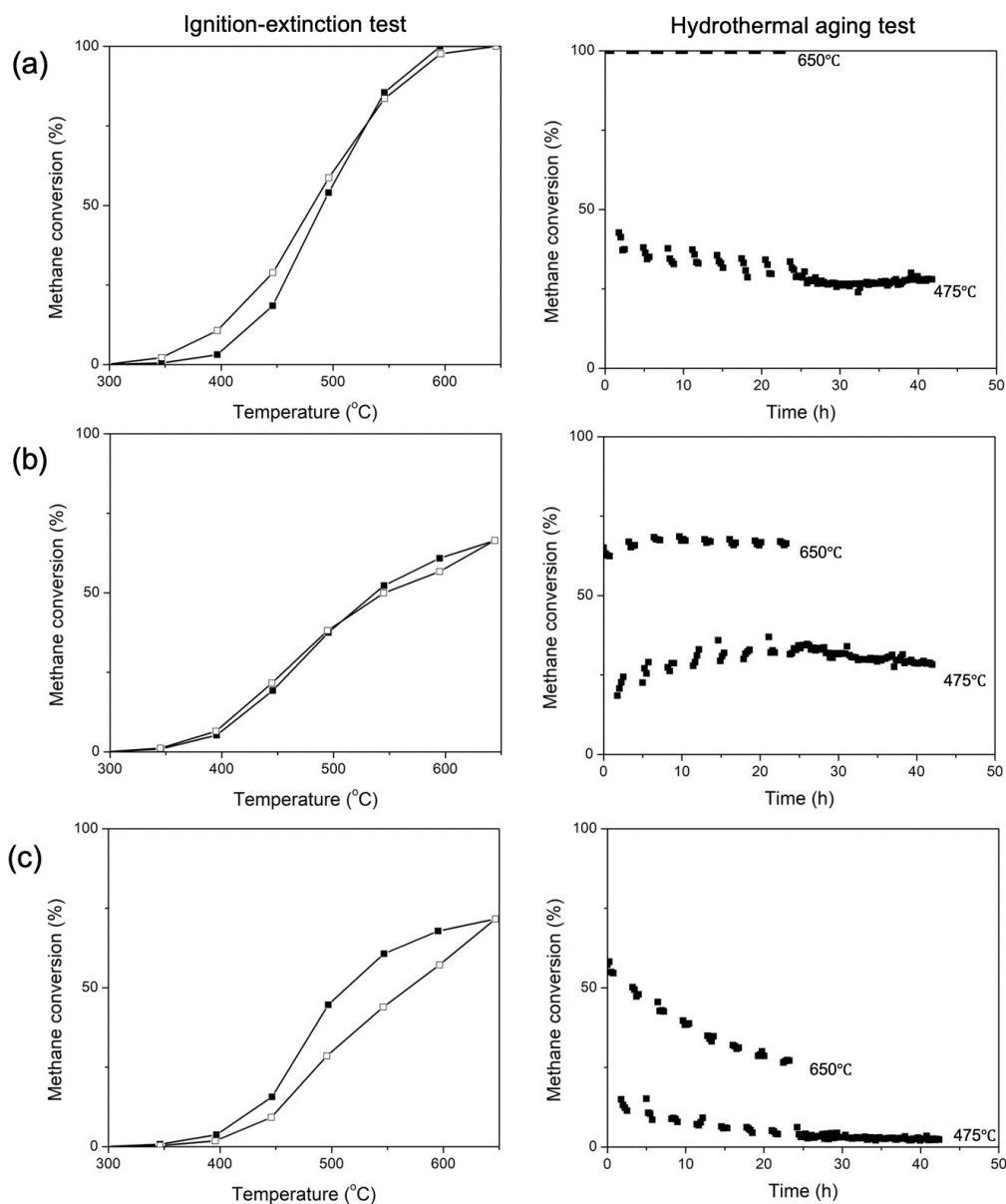


**Figure 4.14** Ignition (solid circle) and extinction (hollow circle) curves on the left side and hydrothermal tests on the right side for three different Pd-Pt on ZrO<sub>2</sub> catalysts (a) Pd-Pt@void@ZrO<sub>2</sub> yolk-shell nanoparticles, (b) Pd-Pt@ZrO<sub>2</sub> directly, (c) Pd-Pt impregnated on ZrO<sub>2</sub>. For the ignition–extinction curves, the catalyst was tested at 300, 350, 400, 450, 500, 550, 600, and 650 °C during ignition, and then tested at 650, 600, 550, 500, 450, 400, 350, 300 °C during extinction, for 30 min at each temperature. For the hydrothermal tests, they were done after the ignition–extinction test, so we know the estimated 100% conversion (~650 °C) and 50% conversion temperature (~475 °C). Thus, the temperature was cycling between 650 and 475 °C for 1 h at each temperature; in total, eight cycles in about 22 h. Then, reactor temperature was held at 475 °C for another 20 h.

The TEM image in Figure 4.15 shows that after hydrothermal ageing, the Pd-Pt@void@ZrO<sub>2</sub> yolk-shell nanoparticles have maintained their structural integrity. For the Pd-Pt@ZrO<sub>2</sub> core-shell nanoparticles after hydrothermal ageing, we can still see Pd-Pt nanoparticles through the ZrO<sub>2</sub> shell in Figure 4.12c. As the Pd-Pt nanoparticles are immobilized within the ZrO<sub>2</sub> shell, the size is still ~8 nm. Therefore, the reason that the Pd-Pt@void@ZrO<sub>2</sub> and Pd-Pt@ZrO<sub>2</sub> catalysts maintain their activity for the entire hydrothermal aging test (up to 42 h), is that the Pd-Pt nanoparticles are kept isolated by the ZrO<sub>2</sub> shell and thus do not undergo sintering at high temperature. For the case of the Pd-Pt/ZrO<sub>2</sub> impregnated catalysts, however, the Pd-Pt nanoparticles are “sitting” on the surface of the bulk ZrO<sub>2</sub> surface, as shown in Figure 4.13b, and these Pd-Pt nanoparticles aggregate after the test (Figure 4.13c), resulting in an appreciable increment in the size of the Pd-Pt nanoparticles from  $7.7 \pm 5.0$  nm to  $29.8 \pm 11.3$  nm.

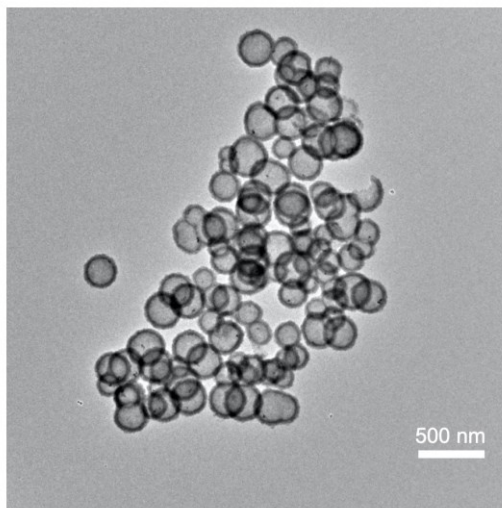


**Figure 4.15** TEM image of the Pd-Pt@void@ZrO<sub>2</sub> yolk-shell nanoparticles after the hydrothermal aging test for 42 h. All yolk-shell particles are not sintered, and the hollow structures are still intact when compared to Figure 4.5d.

The ultimate objective of synthesizing these nanoparticles is to apply them to mitigate unburnt CH<sub>4</sub> in the engine exhaust gas. In exhaust gas systems, the temperature that can be achieved is between 495 and 540 °C, when the catalyst is placed upstream of the engine’s turbocharger.<sup>251, 252</sup> Hence, a catalyst that can offer 100% methane conversion at about 500 °C is ideal in practice. However, Pd-Pt@void@ZrO<sub>2</sub>

nanoparticles, Pd-Pt@ZrO<sub>2</sub> nanoparticles, and Pd-Pt/ZrO<sub>2</sub> impregnated catalysts delivered about 60%, 40%, and 40% methane conversion rate at 500 °C, respectively; therefore, further optimization is needed.

We attempted to improve the catalytic performance further by the following approaches. Firstly, since high metal loading would increase the density and thus enable smaller volume catalytic converters, which are more favorable in industrial applications, we tried to decrease the size of the yolk-shell nanoparticles from 204 nm to 100 nm (shown in Figure 4.16a); this increased the Pd metal loading from 0.57% to 1.23%. Secondly, “free” and unencumbered active sites are crucial, so we attempted to remove as much of the remaining silica as possible by increasing the NaOH etching time from 6 h to 24 h; the Zr/Si molar ratio increased from 1.2 to 1.7 (Table 4.2). We then assessed the catalytic activity and stability of the smaller yolk-shell nanoparticles with higher metal loading; the 100% methane combustion temperature remained the same (Figure 4.16b).

**Table 4.2 SiO<sub>2</sub>, ZrO<sub>2</sub> Contents of Yolk-shell Nanoparticles for Different NaOH Etching Times.**

Catalyst	NaOH etching time (h)	SiO <sub>2</sub> (wt %)	ZrO <sub>2</sub> (wt %)	Zr/Si molar ratio
Pd-Pt@void@ZrO <sub>2</sub> (204 nm)	6	27.7	68.5	1.2
Pd-Pt@void@ZrO <sub>2</sub> (100 nm)	24	21.3	74.1	1.7

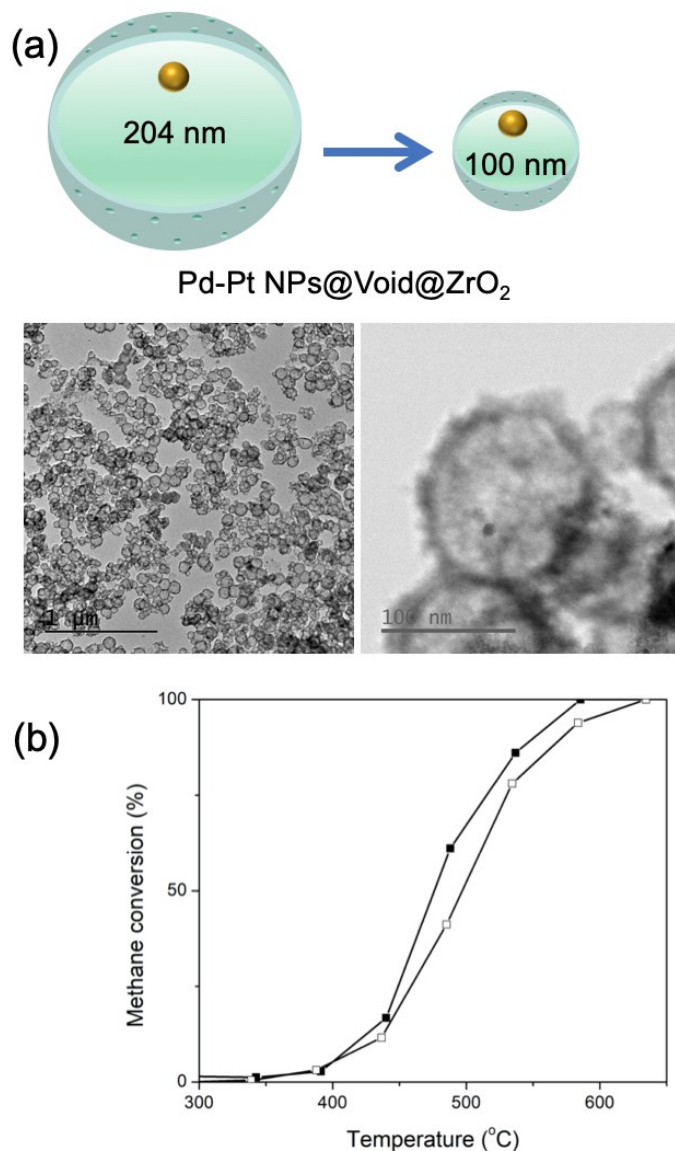


**Figure 4.16 (a) Increasing the metal loading by decreasing the void volume of the nanostructures, so that we get smaller yolk-shell nanoparticles, from  $204 \pm 44$  nm to  $100 \pm 21$  nm and Pd metal loading from 0.57 % to 1.23 %. (b) The corresponding ignition (solid circle) and extinction (open circle) curves for yolk-shell nanoparticles with higher metal loading and longer etching time.**

As has been suggested by Schüth, it is not possible to extract all the silica from the sample even though, when using a NaOH solution for SiO<sub>2</sub> extraction over 50 h, they observed that the Zr/Si ratio reaches a plateau of 1.8 after an extraction time of about 20 h.<sup>235</sup> In other words, incomplete etching of silica might have blocked Pd-Pt active sites, leading to lower activity. Therefore, the steric protection of yolk-shell

nanostructure is an effective structure to enhance the catalysis stability, but the catalysis activity is limited due to the nature of the structure, namely, the remaining SiO<sub>2</sub> that blocks active sites of Pd-Pt nanoparticles.

### 4.3 Conclusions

Bimetallic Pd-Pt@void@ZrO<sub>2</sub> yolk-shell nanostructures were synthesized and tested for wet methane combustion. The stability of the encapsulated catalyst in the lean CH<sub>4</sub> combustion was investigated using a hydrothermal ageing test at temperatures up to 650 °C with 5 mol% water in the feed. The yolk-shell nanoparticles catalyst showed higher conversions (100% methane conversion) and longer stability (up to 42 h) at T = 650 °C, compared to the Pd-Pt/ZrO<sub>2</sub> impregnated catalysts (65% methane conversion, no stability) and Pd-Pt@ZrO<sub>2</sub> (65% methane conversion, stable for 42 h) with the same metal loading. The yolk-shell nanoreactors can be used to increase the lifetime of noble nanoparticles but seem to lower the mass transfer efficiency during the methane combustion due to the remaining silicon.

## 4.4 Experimental Section

### 4.4.1 Materials

Millipore water (resistivity of 18.2 MΩ•cm) was used throughout the work. Sodium tetrachloropalladate (Na<sub>2</sub>PdCl<sub>4</sub>, >99.9%), potassium tetrachloroplatinate (K<sub>2</sub>PtCl<sub>4</sub>, >99.9%), sodium iodide (NaI, ACS reagent, >99.5%), poly(vinyl pyrrolidone) (PVP, MW≈55000), N, N-dimethylformamide (DMF), ammonium hydroxide solution (ACS reagent, 28.0–30.0% NH<sub>3</sub> basis), tetraethylorthosilicate (TEOS, reagent grade, 98%), zirconium butoxide solution (80 wt% in 1-butanol), zirconium oxide (powder, 5 μm, 99% trace metals basis), and palladium (II) chloride solution (PdCl<sub>2</sub>, 5% w/v), hexachloroplatinic acid solution (H<sub>2</sub>PtCl<sub>6</sub>, 8 wt.% in H<sub>2</sub>O), were all purchased from Sigma-Aldrich. All the chemicals were used as received without further purification.

#### 4.4.2 Characterization

The S/TEM/EDX (energy dispersive X-ray) analysis was performed on a JEOL JEM-ARM200cF S/TEM, which was equipped with a cold Field-Emission Gun and a probe Cs corrector. EDX maps were acquired with a Silicon Drift EDX detector at an acceleration voltage of 200 kV. The samples were prepared by dropping a dispersion of samples onto carbon-coated copper TEM grids (Ted Pella, Inc.) using pipettes and dried under ambient condition. ImageJ software was used to measure the particle size and standard deviation of the samples. The measurements were done by counting 200 nanoparticles from the TEM images. The Pd wt% of the prepared catalysts was estimated by a Perkin Elmer Elan 6000 quadrupole inductively coupled plasma mass spectrometer (ICP-MS). The BET surface area and adsorption isotherms of the catalysts were determined at -195 °C by volumetric measurements using a surface area analyzer (Quantachrome, Autosorb iQ). Prior to adsorption analyses, a 30 to 100 mg of the sample was degassed for 4 h at 350 °C under vacuum with a helium backfill gas to remove any moisture or volatiles within the existing pores of the material. The BET model was used to determine the surface area of the catalysts from the N<sub>2</sub> adsorption isotherms. The specific surface area was calculated using the BET method, and the pore size distribution was derived from the BJH model.

#### 4.4.3 Synthesis of Pd-Pt Bimetallic Nanoparticles

In a typical synthesis of cubic Pd-Pt nanocrystals, sodium tetrachloropalladate (Na<sub>2</sub>PdCl<sub>4</sub>, 20 mM, 1.0 mL), potassium tetrachloroplatinate (K<sub>2</sub>PtCl<sub>4</sub>, 20 mM, 1.0 mL), sodium iodide (NaI, 75.0 mg), and poly(vinylpyrrolidone) (PVP, 160.0 mg) were mixed together with 10 mL N, N-dimethylformamide in a 22.0 mL vial. After the vial had been capped, the mixture was ultrasonicated for about 2 min. The resulting homogeneous mixture was transferred into a conventional oven and heated at 130 °C for 5 h before it was cooled to room temperature. The resulting colloidal products were collected by centrifugation at 10000 rpm for 15 min and washed with acetone three times.<sup>243</sup>

#### 4.4.4 Synthesis of Pd-Pt@SiO<sub>2</sub> Nanoparticles

The PVP-stabilized Pd-Pt nanoparticles were dispersed in 200 mL of ethanol, to which 10 mL of NH<sub>4</sub>OH, 18 mL of DI water, and 1.4 mL of tetraethyl orthosilicate (TEOS) were added. The formation of the siliceous gel and its aging were continued by stirring at room temperature for 12 h. Thicker silica shells could be grown by subsequent addition of more TEOS every 12 h. The Pd-Pt@SiO<sub>2</sub> was collected by centrifuging at 10000 rpm for 15 min, washing with water two times, and absolute ethanol two times, respectively.

#### 4.4.5 Synthesis of Pd-Pt@void@ZrO<sub>2</sub> Nanoparticles

As shown in Figure 4.4c and d, the synthesis of Pd@void@ZrO<sub>2</sub> occurred in two steps: Pd@SiO<sub>2</sub> was encapsulated with ZrO<sub>2</sub> to prepare Pd@SiO<sub>2</sub>@ZrO<sub>2</sub>, then the silica layer was etched from Pd@SiO<sub>2</sub>@ZrO<sub>2</sub> with a NaOH solution. The as-prepared Pd@SiO<sub>2</sub> particles were dispersed in a mixture of Lutensol XP50 (BASF, 0.06 mL), water (1.48 mL), and pure ethanol (400 mL) with sonication. Zirconium butoxide solution (2 mL) was added, and the solution was stirred for 15 h at room temperature. The solids (Pd@SiO<sub>2</sub>@ZrO<sub>2</sub>) were collected by centrifuging at 10000 rpm for 15 min and then washed with water three times. This was followed by calcination at 60 °C overnight and calcination at 600 °C for 6 h, both of which were performed in air to remove the organics and form zirconia. The prepared Pd@SiO<sub>2</sub>@ZrO<sub>2</sub> was added to a NaOH solution (500 mL, 0.2 M), which was stirred for 6 h to remove the inner layer of silica. The solids (Pd@void@ZrO<sub>2</sub>) were separated by centrifugation (10000 rpm, 15 min) and washed with water three times. Then, the Pd@void@ZrO<sub>2</sub> was dried overnight at 60 °C in air.

#### 4.4.6 Synthesis of Pd-Pt@ZrO<sub>2</sub> Catalyst

As prepared Pd-Pt nanoparticles were dispersed in a mixture of Lutensol XP50 (BASF, 0.06 mL), water (1.48 mL), and pure ethanol (400 mL) with sonication. Zirconium butoxide solution (2 mL) was added, and the solution was stirred for 15 h at room temperature. The solids (Pd-Pt@ZrO<sub>2</sub>) were collected by centrifuging at 10000 rpm for

15 min and then washed with water three times, followed by calcination at 60 °C overnight and calcination at 600 °C for 6 h in air to remove the organics and form zirconia.

#### **4.4.7 Synthesis of Pd-Pt/ZrO<sub>2</sub> Impregnated Catalyst**

The Pd-Pt/ZrO<sub>2</sub> catalyst was prepared using a wetness impregnation method to achieve the same metals loadings as in the encapsulated PdPt@void@ZrO<sub>2</sub> catalyst. A mix solution of palladium chloride and hexachloroplatinic acid with 1:1 molar ratio was impregnated onto the ZrO<sub>2</sub> support (pre-calcined at 550 °C for 4 h). The catalysts were dried overnight at room temperature and subsequently calcined under air at 550 °C for 16 h.

#### **4.4.8 Test for Wet Methane Combustion**

Wet methane combustion in the presence of 5 mol% water was investigated according to the previous study.<sup>190, 208</sup> A tubular reactor was packed with calcined catalysts (550 °C, 16 h under static air) corresponding to 0.38 mg active Pd in relevant catalysts. Methane (10% balanced in N<sub>2</sub>, Praxair, 8.5 mL/min) and air (extra-dry, Praxair, 200 mL/min) were pre-mixed and fed into the reactor (4100 ppm CH<sub>4</sub> in N<sub>2</sub> and air mixture). The reactions were carried out at a pressure of 1.1 bar. Ignition and extinction curves were obtained by increasing and decreasing the reaction temperature stepwise (50 °C for each step), respectively, with a ramping rate of 60 °C/min; the system was held at each temperature for 30 min. The ignition curves were initiated at 300 °C and ended at 650 °C, and the extinction was performed vice versa to investigate the catalytic performance during cooling down. First, an ignition–extinction experiment (with 5 mol% water) was performed to precondition the catalyst, followed by the hydrothermal aging in the wet methane/air feed by increasing the reaction temperature to 650 °C (60 °C/min ramping rate) and then cooling the reactor to 475 °C, giving about 50% CH<sub>4</sub> conversion. The high-low temperature cycling was repeated eight times (about 22 h). Each temperature stage was held for 1 h. After the cycling was completed, the reactor temperature was held at the selected temperature for another 20 h. The gas outlet from

the reactor was analyzed online every 15-min using an Agilent HP 7890A gas chromatograph equipped with a thermal conductivity detector (TCD) and a flame ionization detector (FID) in series.

## **Chapter 5 Thesis Summary and Outlook**

### **5.1 Summary**

This thesis has examined two reactions that are triggered by noble metal nanoparticles. The primary one is plasmon-driven hydrosilylation on silicon surfaces, which is driven by plasmonic stamps fabricated by gold dewetting on PDMS. Another one is wet methane combustion driven by Pd-Pt@void@ZrO<sub>2</sub> yolk-shell nanoparticles. To conclude the two stories, summaries of each preceding chapter and future research directions are provided in the following sections.

#### **5.1.1 Chapter 1**

In Chapter 1, the background of both plasmonics and hydrosilylation was introduced. Firstly, the concept of plasmonics and plasmon-driven reactions was discussed in the order of their proposed mechanisms, including confined plasmonic fields, hot carrier excitation, and local heat generation. Then, recent advances of plasmon-driven reactions for surface functionalization with molecules, polymers, and nanomaterials were reviewed, followed by surface functionalization on silicon surfaces via hydrosilylation. Lastly, the fabrication of metallic (Pd, Pt, and Au) nanoparticle embedded PDMS stamps and hydrosilylation on flat silicon surfaces were described in detail.

#### **5.1.2 Chapter 2**

Chapter 2 describes a facile method to prepare plasmonic stamps. These stamps with tunable absorption wavelengths were prepared by sputtering gold films on PDMS, followed by thermal annealing to dewet the gold and form an array of gold nanoparticles on the PDMS surface. Then, the as-prepared plasmonic stamps were used to drive hydrosilylation reactions on hydride-terminated silicon surfaces in a spatially defined manner upon illumination with low energy green light (wavelengths of 400–580 nm). By changing the thickness of the initial sputtered gold film on the PDMS, a series of plasmonic stamps with different gold nanoparticle sizes and densities could

be prepared and then employed as a stamp to drive hydrosilylation of 1-alkenes on silicon surfaces. Hydrosilylation of, for instance, 1-dodecene, leads to the formation of monolayers of 1-dodecyl groups with tunable densities on Si(111)-H wafers. The localized surface plasmons of the gold nanoparticles on the PDMS stamp generate a proximal electric field with respect to the underlying silicon, thus forming localized electron/hole pairs that underpin the mechanism for hydrosilylation. These plasmonic stamps are a useful starting point for the discovery of new plasmon-driven reactivity on semiconductor surfaces.

### **5.1.3 Chapter 3**

Chapter 3 describes an in-depth mechanistic investigation of the plasmon-driven hydrosilylation. To ensure reproducibility, fabrication of the production of the plasmonic stamps was optimized via tuning of the sputtering rate and film thickness of the gold, resulting in a more scalable and reliable method to dewet the gold on the PDMS. We carried out reaction kinetic studies for plasmon-induced hydrosilylation on silicon substrates with five different doping levels. As doping levels of the silicon substrates were modulated, the relationship between reaction rates and built-in electrical fields of metal-insulator-semiconductor junctions were investigated. A physical model explaining the relationship between reaction rate and doping density, optical absorption coefficients, depletion width, and plasmonic electrical field has been built.

### **5.1.4 Chapter 4**

Chapter 4 introduces the background of methane combustion catalysis and then describes the preparation of Pd-Pt@void@ZrO<sub>2</sub> yolk-shell nanoparticles and Pd-Pt@ZrO<sub>2</sub> (Pd: Pt molar ratio = 1:1) core-shell nanoparticles, which were tested for wet methane combustion. By using the hydrothermal aging tests, the catalytic lifetimes of the encapsulated catalysts were assessed. By comparing with core-shell nanoparticles and classical impregnated catalysts, the advantages and limitations of the yolk-shell nanostructures for methane combustion were discussed. Among all three catalysts with the same chemical components, the yolk-shell nanoparticles catalyst showed higher

conversions (100% methane conversion) and longer stability (up to 42 h) than the Pd-Pt/ZrO<sub>2</sub> impregnated catalysts (65% methane conversion, no stability) and Pd-Pt@ZrO<sub>2</sub> (65% methane conversion, stable for 42 h) with the same metal loading at the same temperature (650 °C). The yolk-shell nanoreactors can be used to increase the lifetime of noble nanoparticles, but the silicon remaining due to the nature of the yolk-shell nanostructure, may lower the mass transfer efficiency during the methane combustion catalysis process.

## **5.2 Future Works**

### **5.2.1 Expanding the Menu for Metal Dewetting on PDMS**

The above-mentioned solid-state dewetting of the gold metal film on PDMS is an effective way to tailor the plasmonic resonance. This fabrication route also can be used for other metals, such as silver (Ag),<sup>253</sup> copper (Cu),<sup>254</sup> and aluminum (Al)<sup>255</sup> as a thin metal film on PDMS is thermodynamically unstable and it readily dewets or agglomerates to form the nanoparticles through thermal treatment. For example, aluminum for plasmonics has attracted much attention recently.<sup>256, 257, 258</sup> The Halas group reported that, unlike silver and gold, aluminum has material properties that enable strong plasmon resonances spanning much of the visible region of the spectrum and into the ultraviolet(Figure 5.1). This extended response, combined with its natural abundance, low cost, and amenability to manufacturing processes, makes aluminum as a highly promising plasmonic material.

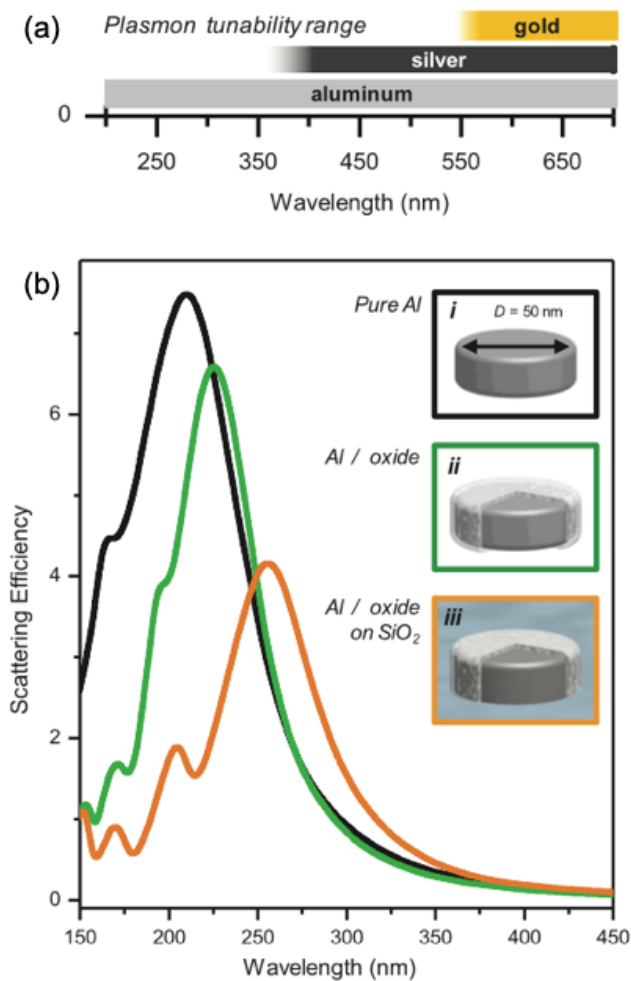


**Figure 5.1 Aluminum as a plasmonic material. (a) Plasmon tuning ranges of the most common plasmonic materials, Au and Ag, compared with Al. (b) Calculated spectra for a 35-nm thick, 50 nm diameter Al nanodisk: (i) a pure, isolated Al nanodisk (black); (ii) an isolated Al nanodisk with a 3 nm surface oxide (green); and (iii) the same Al nanodisk on an infinite SiO<sub>2</sub> substrate (orange). Reproduced with permission from reference 256. Copyright 2014 American Chemical Society.**

Notably, Ag, Cu, and Al nanoparticles are not as stable as Au nanoparticles in the air or under light illumination, but Au-Ag, Au-Cu, and Au-Al bimetallic nanoparticles are more stable than monometallic nanoparticles. In 2017, Kang et al. reported that by using successive thermal sputtering of thin Au and Ag films and thermal dewetting, bimetallic Au-Ag nanoparticles can be obtained on quartz substrates, as shown in Figure 5.2.<sup>259</sup> Because of the complete miscibility of Au and Ag, a programmable plasmon resonance wavelength in a broadband visible range can be

achieved. We can use this method to prepare various bimetallic nanoparticles for the plasmonic stamp fabrication; thus the application of the plasmon-driven surface functionalization can be extended, owing to the extraordinary broadband SPR wavelength.

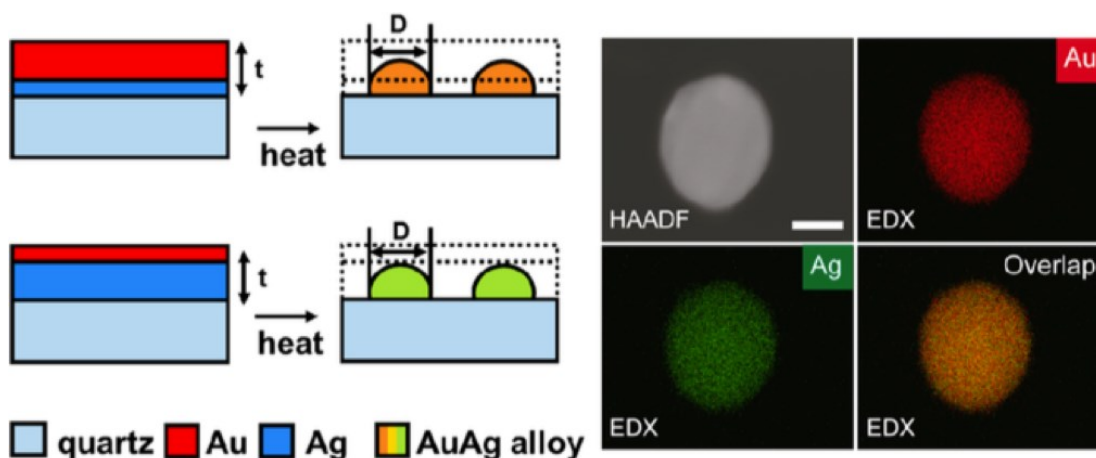
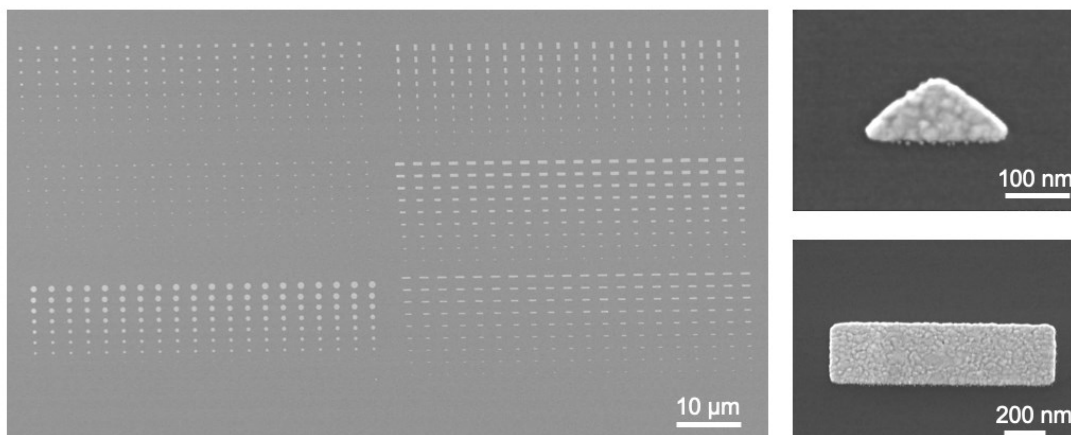


Figure 5.2 Scheme of nanofabrication for Au-Ag nanoparticles by using successive thin film deposition and thermal dewetting. The individual and total film thicknesses of Au and Ag determine the Au/Ag fractions and the average diameter of nanoparticles. High-angle annular dark-field (HAADF) and energy-dispersive X-ray (EDX) mapping of Au and Ag elements. Reproduced with permission from reference 259. Copyright 2017 American Chemical Society.

### 5.2.2 Variation of Shapes for Plasmonic Nanoparticles on PDMS

Although metal dewetting on PDMS is a facile and reproducible way for the fabrication of plasmonic stamps, the shape of the as-prepared nanoparticles on PDMS is usually spheres/hemispheres. To better investigate the mechanism of plasmon-driven mechanisms and extend the application of plasmonic stamps, fabricating plasmonic nanostructures with variable shapes are of great interest. Plasmonic nanoparticles and nanostructures often are fabricated by top-down techniques, including electron beam lithography (EBL), which develops well-designed morphologies and orientations.<sup>260,261</sup> As shown in Figure 5.3, nanoparticles with different sizes and shapes, including rods, triangles and cubes, are prepared by EBL. Next, if all these nanoparticles can be transferred effectively to the PDMS, a series of plasmonic stamps can be obtained. For

example, as the hot spots of Au nanotriangles are at the three corners, the molecules may tend to form in these regions via plasmon-driven reactions.<sup>262, 263</sup>



**Figure 5.3** Left: SEM images of gold nanoparticles with different sizes and shapes (sphere, rod, square, and triangle) fabricated by EBL. Right: zoom in SEM of gold nanotriangles and nanorods.

As the metal is evaporated onto the Si surface, it may hard to be peeled off the metal nanoparticles by PDMS without using an anti-sticking layer and/or capture molecules.<sup>264–266</sup> For example, Lee et al. reported two procedures to embed metallic structures in an elastomeric polymer substrate by maintaining adhesion between PDMS and embedded metallic structures, as shown in Figure 5.4, which refer to Method I and Method II.<sup>267</sup> The depositions of both the 3-mercaptopropyl trimethoxysilane (MPT) adhesion and the silane release layers occur in a different order for each method. Once the metallic structures and SAMs are patterned, the procedure followed to embed them in PDMS is identical. Additionally, the time and cost to prepare nanoparticles with wide areas on the Si surface by EBL is another problem.

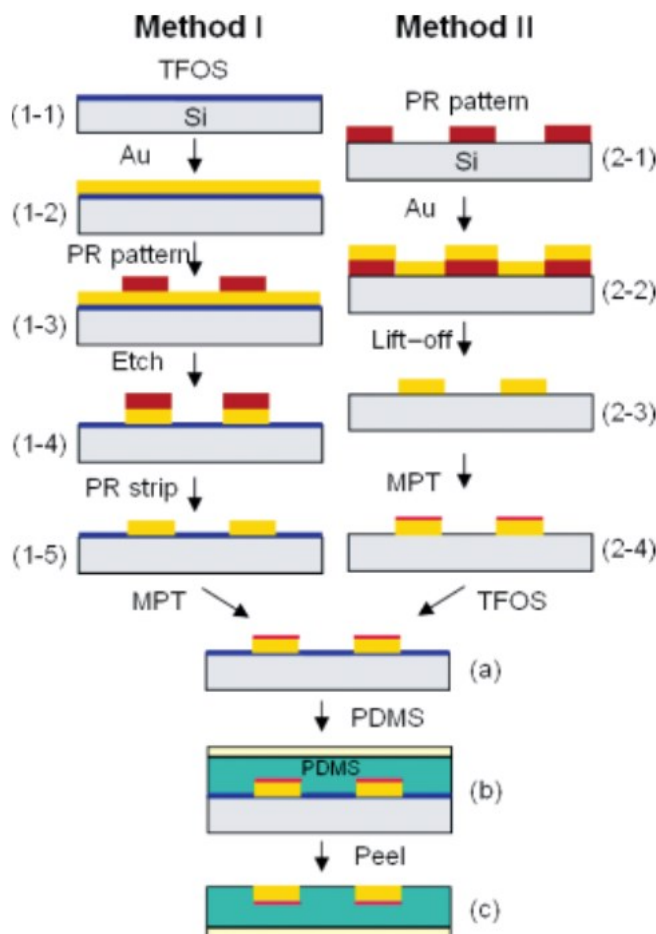
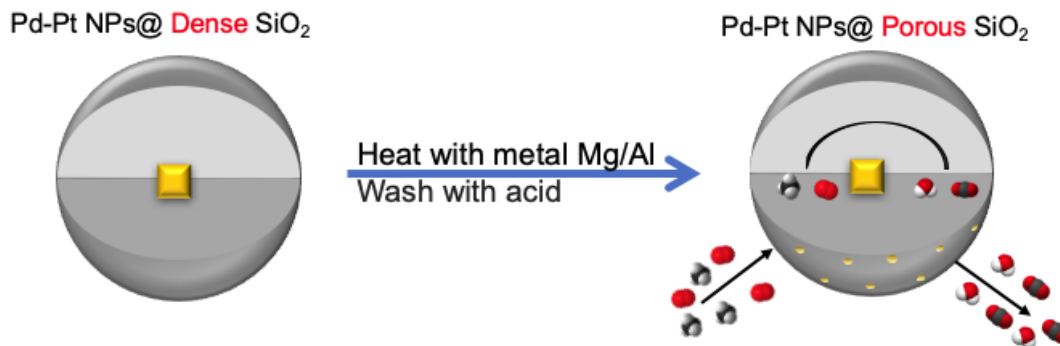


Figure 5.4 Scheme of two different fabrication ways used to embed metallic patterns into soft PDMS. TFOS: tridecafluoro-1,1,2,2-tetrahydro-octyl-1-trichlorosilane; PR: photoresist; MPT: 3-mercaptopropyl trimethoxysilane. Reproduced with permission from reference 267. Copyright 2005 Wiley-VCH.

### 5.2.3 Synthesis Pd-Pt@SiO<sub>2</sub> Nanoparticles via Magnesiothermic Reduction

The Pd-Pt nanoparticles can be encapsulated by SiO<sub>2</sub> shells by the Stober method. However, this Pd-Pt@SiO<sub>2</sub> structure is not sufficiently porous to permit the satisfactory mass transfer of reactants to the Pd-Pt metal sites. The existing practices to make porous SiO<sub>2</sub> shells are mainly by a template-based method<sup>268, 269</sup> and an etching-based method.<sup>201, 204</sup> The magnesiothermic reduction is also an effective method to produce porous Si.<sup>270-272</sup> As illustrated in Figure 5.5, Pd-Pt@ porous SiO<sub>2</sub> can be synthesized

by reacting with Mg/Al at 650 °C, followed by an acid wash to remove the remaining Mg and MgO. Therefore, the porosity of the SiO<sub>2</sub> shells is enhanced significantly; this will be a new method to prepare catalysts for methane combustion with a long lifetime.



**Figure 5.5** Schematic representation of synthesizes Pd-Pt@porous SiO<sub>2</sub> via magnesiothermic reduction.

## References

- (1) Zhou, L.; Swearer, D. F.; Zhang, C.; Robotjazi, H.; Zhao, H.; Henderson, L.; Dong, L.; Christopher, P.; Carter, E. A.; Nordlander, P.; Halas, N. J. Quantifying Hot Carrier and Thermal Contributions in Plasmonic Photocatalysis. *Science* **2018**, *362* (6410), 69–72. <https://doi.org/10.1126/science.aat6967>.
- (2) Halas, N. J. Plasmonics: An Emerging Field Fostered by Nano Letters. *Nano letters* **2010**, *10* (10), 3816–3822.
- (3) Hartland, G. V.; Besteiro, L. V.; Johns, P.; Govorov, A. O. What's so Hot about Electrons in Metal Nanoparticles? *ACS Energy Lett.* **2017**, *2* (7), 1641–1653. <https://doi.org/10.1021/acsenergylett.7b00333>.
- (4) Christopher, P.; Xin, H.; Linic, S. Visible-Light-Enhanced Catalytic Oxidation Reactions on Plasmonic Silver Nanostructures. *Nature Chem* **2011**, *3* (6), 467–472. <https://doi.org/10.1038/nchem.1032>.
- (5) Swearer, D. F.; Zhao, H.; Zhou, L.; Zhang, C.; Robotjazi, H.; Martirez, J. M. P.; Krauter, C. M.; Yazdi, S.; McClain, M. J.; Ringe, E.; Carter, E. A.; Nordlander, P.; Halas, N. J. Heterometallic Antenna–reactor Complexes for Photocatalysis. *PNAS* **2016**, *113* (32), 8916–8920. <https://doi.org/10.1073/pnas.1609769113>.
- (6) Yu, S.; Wilson, A. J.; Heo, J.; Jain, P. K. Plasmonic Control of Multi-Electron Transfer and C–C Coupling in Visible-Light-Driven CO<sub>2</sub> Reduction on Au Nanoparticles. *Nano Lett.* **2018**, *18* (4), 2189–2194. <https://doi.org/10.1021/acs.nanolett.7b05410>.
- (7) Choi, C. H.; Chung, K.; Nguyen, T.-T. H.; Kim, D. H. Plasmon-Mediated Electrocatalysis for Sustainable Energy: From Electrochemical Conversion of Different Feedstocks to Fuel Cell Reactions. *ACS Energy Lett.* **2018**, *3* (6), 1415–1433. <https://doi.org/10.1021/acsenergylett.8b00461>.
- (8) Shaik, F.; Peer, I.; Jain, P. K.; Amirav, L. Plasmon-Enhanced Multicarrier Photocatalysis. *Nano Lett.* **2018**, *18* (7), 4370–4376. <https://doi.org/10.1021/acs.nanolett.8b01392>.
- (9) Wu, N. Plasmonic Metal–Semiconductor Photocatalysts and Photoelectrochemical Cells: A Review. *Nanoscale* **2018**, *10* (6), 2679–2696. <https://doi.org/10.1039/C7NR08487K>.

- (10) Hou, W.; Cronin, S. B. A Review of Surface Plasmon Resonance-Enhanced Photocatalysis. *Advanced Functional Materials* **2013**, *23* (13), 1612–1619. <https://doi.org/10.1002/adfm.201202148>.
- (11) Pendry, J. B.; Martín-Moreno, L.; Garcia-Vidal, F. J. Mimicking Surface Plasmons with Structured Surfaces. *Science* **2004**, *305* (5685), 847–848. <https://doi.org/10.1126/science.1098999>.
- (12) Polini, M.; Asgari, R.; Borghi, G.; Barlas, Y.; Pereg-Barnea, T.; MacDonald, A. H. Plasmons and the Spectral Function of Graphene. *Phys. Rev. B* **2008**, *77* (8), 081411. <https://doi.org/10.1103/PhysRevB.77.081411>.
- (13) Ghaemi, H. F.; Thio, T.; Grupp, D. E.; Ebbesen, T. W.; Lezec, H. J. Surface Plasmons Enhance Optical Transmission through Subwavelength Holes. *Phys. Rev. B* **1998**, *58* (11), 6779–6782. <https://doi.org/10.1103/PhysRevB.58.6779>.
- (14) Pitarke, J. M.; Silkin, V. M.; Chulkov, E. V.; Echenique, P. M. Theory of Surface Plasmons and Surface-Plasmon Polaritons. *Rep. Prog. Phys.* **2006**, *70* (1), 1–87. <https://doi.org/10.1088/0034-4885/70/1/R01>.
- (15) Shelton, C. K.; Epps, T. H. Mapping Substrate Surface Field Propagation in Block Polymer Thin Films. *Macromolecules* **2016**, *49* (2), 574–580. <https://doi.org/10.1021/acs.macromol.5b02141>.
- (16) Economou, E. N. Surface Plasmons in Thin Films. *Phys. Rev.* **1969**, *182* (2), 539–554. <https://doi.org/10.1103/PhysRev.182.539>.
- (17) Mayer, K. M.; Hafner, J. H. Localized Surface Plasmon Resonance Sensors. *Chem. Rev.* **2011**, *111* (6), 3828–3857. <https://doi.org/10.1021/cr100313v>.
- (18) Zayats, A. V.; Smolyaninov, I. I. Near-Field Photonics: Surface Plasmon Polaritons and Localized Surface Plasmons. *J. Opt. A: Pure Appl. Opt.* **2003**, *5* (4), S16–S50. <https://doi.org/10.1088/1464-4258/5/4/353>.
- (19) Rycenga, M.; Cobley, C. M.; Zeng, J.; Li, W.; Moran, C. H.; Zhang, Q.; Qin, D.; Xia, Y. Controlling the Synthesis and Assembly of Silver Nanostructures for Plasmonic Applications. *Chem. Rev.* **2011**, *111* (6), 3669–3712. <https://doi.org/10.1021/cr100275d>.

- (20) Faraday, M. The Bakerian Lecture: Experimental Relations of Gold (and Other Metals) to Light. *Philosophical Transactions of the Royal Society of London* **1857**, *147*, 145–181.
- (21) Mie, G. Beiträge Zur Optik Trüber Medien, Speziell Kolloidaler Metallösungen. *Annalen der Physik* **1908**, *330* (3), 377–445. <https://doi.org/10.1002/andp.19083300302>.
- (22) Odom, T. W.; Schatz, G. C. Introduction to Plasmonics. *Chem. Rev.* **2011**, *111* (6), 3667–3668. <https://doi.org/10.1021/cr2001349>.
- (23) Yang, P.; Zheng, J.; Xu, Y.; Zhang, Q.; Jiang, L. Colloidal Synthesis and Applications of Plasmonic Metal Nanoparticles. *Advanced Materials* **2016**, *28* (47), 10508–10517. <https://doi.org/10.1002/adma.201601739>.
- (24) Linic, S.; Aslam, U.; Boerigter, C.; Morabito, M. Photochemical Transformations on Plasmonic Metal Nanoparticles. *Nature Mater* **2015**, *14* (6), 567–576. <https://doi.org/10.1038/nmat4281>.
- (25) Hedayati, M. K.; Faupel, F.; Elbahri, M. Review of Plasmonic Nanocomposite Metamaterial Absorber. *Materials* **2014**, *7* (2), 1221–1248. <https://doi.org/10.3390/ma7021221>.
- (26) Kravets, V. G.; Kabashin, A. V.; Barnes, W. L.; Grigorenko, A. N. Plasmonic Surface Lattice Resonances: A Review of Properties and Applications. *Chem. Rev.* **2018**, *118* (12), 5912–5951. <https://doi.org/10.1021/acs.chemrev.8b00243>.
- (27) Motl, N. E.; Smith, A. F.; DeSantis, C. J.; Skrabalak, S. E. Engineering Plasmonic Metal Colloids through Composition and Structural Design. *Chem. Soc. Rev.* **2014**, *43* (11), 3823–3834. <https://doi.org/10.1039/C3CS60347D>.
- (28) Zhang, Z.; Wang, H.; Chen, Z.; Wang, X.; Choo, J.; Chen, L. Plasmonic Colorimetric Sensors Based on Etching and Growth of Noble Metal Nanoparticles: Strategies and Applications. *Biosensors and Bioelectronics* **2018**, *114*, 52–65. <https://doi.org/10.1016/j.bios.2018.05.015>.
- (29) Keshavarz Hedayati, M.; Elbahri, M. Review of Metasurface Plasmonic Structural Color. *Plasmonics* **2017**, *12* (5), 1463–1479. <https://doi.org/10.1007/s11468-016-0407-y>.

- (30) Wang, P.; Huang, B.; Dai, Y.; Whangbo, M.-H. Plasmonic Photocatalysts: Harvesting Visible Light with Noble Metal Nanoparticles. *Phys. Chem. Chem. Phys.* **2012**, *14* (28), 9813. <https://doi.org/10.1039/c2cp40823f>.
- (31) Dai, Z.; Xiao, X.; Wu, W.; Zhang, Y.; Liao, L.; Guo, S.; Ying, J.; Shan, C.; Sun, M.; Jiang, C. Plasmon-Driven Reaction Controlled by the Number of Graphene Layers and Localized Surface Plasmon Distribution during Optical Excitation. *Light: Science & Applications* **2015**, *4* (10), e342–e342. <https://doi.org/10.1038/lssa.2015.115>.
- (32) Sun, M.; Xu, H. A Novel Application of Plasmonics: Plasmon-Driven Surface-Catalyzed Reactions. *Small* **2012**, *8* (18), 2777–2786. <https://doi.org/10.1002/sml.201200572>.
- (33) Zhang, Y.; He, S.; Guo, W.; Hu, Y.; Huang, J.; Mulcahy, J. R.; Wei, W. D. Surface-Plasmon-Driven Hot Electron Photochemistry. *Chem. Rev.* **2018**, *118* (6), 2927–2954. <https://doi.org/10.1021/acs.chemrev.7b00430>.
- (34) Fang, Z.; Zhen, Y.-R.; Neumann, O.; Polman, A.; García de Abajo, F. J.; Nordlander, P.; Halas, N. J. Evolution of Light-Induced Vapor Generation at a Liquid-Immersed Metallic Nanoparticle. *Nano Lett.* **2013**, *13* (4), 1736–1742. <https://doi.org/10.1021/nl4003238>.
- (35) Brongersma, M. L.; Halas, N. J.; Nordlander, P. Plasmon-Induced Hot Carrier Science and Technology. *Nature Nanotech* **2015**, *10* (1), 25–34. <https://doi.org/10.1038/nnano.2014.311>.
- (36) Zhang, Z.; Zhang, C.; Zheng, H.; Xu, H. Plasmon-Driven Catalysis on Molecules and Nanomaterials. *Acc. Chem. Res.* **2019**, *52* (9), 2506–2515. <https://doi.org/10.1021/acs.accounts.9b00224>.
- (37) Aslam, U.; Chavez, S.; Linic, S. Controlling Energy Flow in Multimetallic Nanostructures for Plasmonic Catalysis. *Nature Nanotech* **2017**, *12* (10), 1000–1005. <https://doi.org/10.1038/nnano.2017.131>.
- (38) Aslam, U.; Rao, V. G.; Chavez, S.; Linic, S. Catalytic Conversion of Solar to Chemical Energy on Plasmonic Metal Nanostructures. *Nat Catal* **2018**, *1* (9), 656–665. <https://doi.org/10.1038/s41929-018-0138-x>.

- (39) Linic, S.; Aslam, U.; Boerigter, C.; Morabito, M. Photochemical Transformations on Plasmonic Metal Nanoparticles. *Nature Materials* **2015**, *14* (6), 567–576. <https://doi.org/10.1038/nmat4281>.
- (40) Awazu, K.; Fujimaki, M.; Rockstuhl, C.; Tominaga, J.; Murakami, H.; Ohki, Y.; Yoshida, N.; Watanabe, T. A Plasmonic Photocatalyst Consisting of Silver Nanoparticles Embedded in Titanium Dioxide. *J. Am. Chem. Soc.* **2008**, *130* (5), 1676–1680. <https://doi.org/10.1021/ja076503n>.
- (41) Sun, M.; Zhang, Z.; Zheng, H.; Xu, H. In-Situ Plasmon-Driven Chemical Reactions Revealed by High Vacuum Tip-Enhanced Raman Spectroscopy. *Sci Rep* **2012**, *2* (1), 647. <https://doi.org/10.1038/srep00647>.
- (42) Zhang, X.; Li, X.; Reish, M. E.; Zhang, D.; Su, N. Q.; Gutiérrez, Y.; Moreno, F.; Yang, W.; Everitt, H. O.; Liu, J. Plasmon-Enhanced Catalysis: Distinguishing Thermal and Nonthermal Effects. *Nano Lett.* **2018**, *18* (3), 1714–1723. <https://doi.org/10.1021/acs.nanolett.7b04776>.
- (43) Kamarudheen, R.; Castellanos, G. W.; Kamp, L. P. J.; Clercx, H. J. H.; Baldi, A. Quantifying Photothermal and Hot Charge Carrier Effects in Plasmon-Driven Nanoparticle Syntheses. *ACS Nano* **2018**, *12* (8), 8447–8455. <https://doi.org/10.1021/acsnano.8b03929>.
- (44) Keller, E. L.; Frontiera, R. R. Ultrafast Nanoscale Raman Thermometry Proves Heating Is Not a Primary Mechanism for Plasmon-Driven Photocatalysis. *ACS Nano* **2018**, *12* (6), 5848–5855. <https://doi.org/10.1021/acsnano.8b01809>.
- (45) Baffou, G.; Bordacchini, I.; Baldi, A.; Quidant, R. Simple Experimental Procedures to Distinguish Photothermal from Hot-Carrier Processes in Plasmonics. *Light: Science & Applications* **2020**, *9* (1), 1–16. <https://doi.org/10.1038/s41377-020-00345-0>.
- (46) Jamtveit, B.; Meakin, P. Growth, Dissolution and Pattern Formation in Geosystems. In *Growth, Dissolution and Pattern Formation in Geosystems*; Jamtveit, B., Meakin, P., Eds.; Springer Netherlands: Dordrecht, 1999; pp 1–19. [https://doi.org/10.1007/978-94-015-9179-9\\_1](https://doi.org/10.1007/978-94-015-9179-9_1).

- (47) Salaita, K.; Wang, Y.; Mirkin, C. A. Applications of Dip-Pen Nanolithography. *Nature Nanotechnology* **2007**, *2* (3), 145–155. <https://doi.org/10.1038/nnano.2007.39>.
- (48) Liu, G.; Hirtz, M.; Fuchs, H.; Zheng, Z. Development of Dip-Pen Nanolithography (DPN) and Its Derivatives. *Small* **2019**, *15* (21), 1900564. <https://doi.org/10.1002/sml.201900564>.
- (49) Wu, C.-C.; Reinhoudt, D. N.; Otto, C.; Subramaniam, V.; Velders, A. H. Strategies for Patterning Biomolecules with Dip-Pen Nanolithography. *Small* **2011**, *7* (8), 989–1002. <https://doi.org/10.1002/sml.201001749>.
- (50) Salim, A.; Lim, S. Review of Recent Inkjet-Printed Capacitive Tactile Sensors. *Sensors* **2017**, *17* (11), 2593. <https://doi.org/10.3390/s17112593>.
- (51) Kholghi Eshkalak, S.; Chinnappan, A.; Jayathilaka, W. A. D. M.; Khatibzadeh, M.; Kowsari, E.; Ramakrishna, S. A Review on Inkjet Printing of CNT Composites for Smart Applications. *Applied Materials Today* **2017**, *9*, 372–386. <https://doi.org/10.1016/j.apmt.2017.09.003>.
- (52) Ursan, I. D.; Chiu, L.; Pierce, A. Three-Dimensional Drug Printing: A Structured Review. *Journal of the American Pharmacists Association* **2013**, *53* (2), 136–144. <https://doi.org/10.1331/JAPhA.2013.12217>.
- (53) Sugioka, K.; Cheng, Y. Ultrafast Lasers—Reliable Tools for Advanced Materials Processing. *Light: Science & Applications* **2014**, *3* (4), e149–e149. <https://doi.org/10.1038/lssa.2014.30>.
- (54) Komatsu, T.; Honma, T. Laser Patterning and Growth Mechanism of Orientation Designed Crystals in Oxide Glasses: A Review. *Journal of Solid State Chemistry* **2019**, *275*, 210–222. <https://doi.org/10.1016/j.jssc.2019.04.020>.
- (55) Phillips, K. C.; Gandhi, H. H.; Mazur, E.; Sundaram, S. K. Ultrafast Laser Processing of Materials: A Review. *Adv. Opt. Photon., AOP* **2015**, *7* (4), 684–712. <https://doi.org/10.1364/AOP.7.000684>.
- (56) Cortés, E.; Xie, W.; Cambiasso, J.; Jermyn, A. S.; Sundararaman, R.; Narang, P.; Schlücker, S.; Maier, S. A. Plasmonic Hot Electron Transport Drives Nano-Localized Chemistry. *Nat Commun* **2017**, *8* (1), 14880. <https://doi.org/10.1038/ncomms14880>.

- (57) Lee, Y. K.; Jung, C. H.; Park, J.; Seo, H.; Somorjai, G. A.; Park, J. Y. Surface Plasmon-Driven Hot Electron Flow Probed with Metal-Semiconductor Nanodiodes. *Nano Lett.* **2011**, *11* (10), 4251–4255. <https://doi.org/10.1021/nl2022459>.
- (58) Dai, Z.; Xiao, X.; Wu, W.; Zhang, Y.; Liao, L.; Guo, S.; Ying, J.; Shan, C.; Sun, M.; Jiang, C. Plasmon-Driven Reaction Controlled by the Number of Graphene Layers and Localized Surface Plasmon Distribution during Optical Excitation. *Light: Science & Applications* **2015**, *4* (10), e342–e342. <https://doi.org/10.1038/lssa.2015.115>.
- (59) Kherbouche, I.; Luo, Y.; Félidj, N.; Mangeney, C. Plasmon-Mediated Surface Functionalization: New Horizons for the Control of Surface Chemistry on the Nanoscale. *Chem. Mater.* **2020**, [acs.chemmater.0c00921](https://doi.org/10.1021/acs.chemmater.0c00921). <https://doi.org/10.1021/acs.chemmater.0c00921>.
- (60) Nguyen, M.; Lamouri, A.; Salameh, C.; Lévi, G.; Grand, J.; Boubekeur-Lecaque, L.; Mangeney, C.; Félidj, N. Plasmon-Mediated Chemical Surface Functionalization at the Nanoscale. *Nanoscale* **2016**, *8* (16), 8633–8640. <https://doi.org/10.1039/C6NR00744A>.
- (61) Nguyen, V.-Q.; Ai, Y.; Martin, P.; Lacroix, J.-C. Plasmon-Induced Nanolocalized Reduction of Diazonium Salts. *ACS Omega* **2017**, *2* (5), 1947–1955. <https://doi.org/10.1021/acsomega.7b00394>.
- (62) Kim, M.; Lee, J.-H.; Nam, J.-M. Plasmonic Photothermal Nanoparticles for Biomedical Applications. *Advanced Science* **2019**, *6* (17), 1900471. <https://doi.org/10.1002/advs.201900471>.
- (63) Mejía-Salazar, J. R.; Oliveira, O. N. Plasmonic Biosensing. *Chem. Rev.* **2018**, *118* (20), 10617–10625. <https://doi.org/10.1021/acs.chemrev.8b00359>.
- (64) Guselnikova, O.; Marque, S. R. A.; Tretyakov, E. V.; Mares, D.; Jerabek, V.; Audran, G.; Joly, J.-P.; Trusova, M.; Svorcik, V.; Lyutakov, O.; Postnikov, P. Unprecedented Plasmon-Induced Nitroxide-Mediated Polymerization (PI-NMP): A Method for Preparation of Functional Surfaces. *J. Mater. Chem. A* **2019**, *7* (20), 12414–12419. <https://doi.org/10.1039/C9TA01630A>.

- (65) Dostert, K.-H.; Álvarez, M.; Koynov, K.; del Campo, A.; Butt, H.-J.; Kreiter, M. Near Field Guided Chemical Nanopatterning. *Langmuir* **2012**, *28* (8), 3699–3703. <https://doi.org/10.1021/la300009a>.
- (66) Zhou, X.; Wenger, J.; Viscomi, F. N.; Le Cunff, L.; Béal, J.; Kochtcheev, S.; Yang, X.; Wiederrecht, G. P.; Colas des Francs, G.; Bisht, A. S.; Jradi, S.; Caputo, R.; Demir, H. V.; Schaller, R. D.; Plain, J.; Vial, A.; Sun, X. W.; Bachelot, R. Two-Color Single Hybrid Plasmonic Nanoemitters with Real Time Switchable Dominant Emission Wavelength. *Nano Lett.* **2015**, *15* (11), 7458–7466. <https://doi.org/10.1021/acs.nanolett.5b02962>.
- (67) Buriak, J. M. Organometallic Chemistry on Silicon and Germanium Surfaces. *Chem. Rev.* **2002**, *102* (5), 1271–1308. <https://doi.org/10.1021/cr000064s>.
- (68) Ciampi, S.; Harper, J. B.; Gooding, J. J. Wet Chemical Routes to the Assembly of Organic Monolayers on Silicon Surfaces via the Formation of Si–C Bonds: Surface Preparation, Passivation and Functionalization. *Chem. Soc. Rev.* **2010**, *39* (6), 2158. <https://doi.org/10.1039/b923890p>.
- (69) DeBenedetti, W. J. I.; Chabal, Y. J. Functionalization of Oxide-Free Silicon Surfaces. *Journal of Vacuum Science & Technology A: Vacuum, Surfaces, and Films* **2013**, *31* (5), 050826. <https://doi.org/10.1116/1.4819406>.
- (70) Fabre, B. Functionalization of Oxide-Free Silicon Surfaces with Redox-Active Assemblies. *Chem. Rev.* **2016**, *116* (8), 4808–4849. <https://doi.org/10.1021/acs.chemrev.5b00595>.
- (71) Buriak, J. M. Illuminating Silicon Surface Hydrosilylation: An Unexpected Plurality of Mechanisms. *Chem. Mater.* **2014**, *26* (1), 763–772. <https://doi.org/10.1021/cm402120f>.
- (72) Linford, M. R.; Chidsey, C. E. D. Alkyl Monolayers Covalently Bonded to Silicon Surfaces. *J. Am. Chem. Soc.* **1993**, *115* (26), 12631–12632. <https://doi.org/10.1021/ja00079a071>.
- (73) Linford, M. R.; Fenter, P.; Eisenberger, P. M.; Chidsey, C. E. D. Alkyl Monolayers on Silicon Prepared from 1-Alkenes and Hydrogen-Terminated Silicon. *J. Am. Chem. Soc.* **1995**, *117* (11), 3145–3155. <https://doi.org/10.1021/ja00116a019>.

- (74) Stewart, M. P.; Buriak, J. M. Photopatterned Hydrosilylation on Porous Silicon. *Angew. Chem. Int. Ed.* **1998**, *37* (23), 3257–3260. [https://doi.org/10.1002/\(SICI\)1521-3773\(19981217\)37:23<3257::AID-ANIE3257>3.0.CO;2-1](https://doi.org/10.1002/(SICI)1521-3773(19981217)37:23<3257::AID-ANIE3257>3.0.CO;2-1).
- (75) Shaikh, N. S.; Enthaler, S.; Junge, K.; Beller, M. Iron-Catalyzed Enantioselective Hydrosilylation of Ketones. *Angewandte Chemie International Edition* **2008**, *47* (13), 2497–2501. <https://doi.org/10.1002/anie.200705624>.
- (76) Buriak, J. M.; Stewart, M. P.; Geders, T. W.; Allen, M. J.; Choi, H. C.; Smith, J.; Raftery, D.; Canham, L. T. Lewis Acid Mediated Hydrosilylation on Porous Silicon Surfaces. *J. Am. Chem. Soc.* **1999**, *121* (49), 11491–11502. <https://doi.org/10.1021/ja992188w>.
- (77) Stewart, M. P.; Buriak, J. M. Exciton-Mediated Hydrosilylation on Photoluminescent Nanocrystalline Silicon. *J. Am. Chem. Soc.* **2001**, *123* (32), 7821–7830. <https://doi.org/10.1021/ja011116d>.
- (78) Mizuno, H.; Buriak, J. M. Nanoscale Patterning of Organic Monolayers by Catalytic Stamp Lithography: Scope and Limitations. *ACS Appl. Mater. Interfaces* **2009**, *1* (12), 2711–2720. <https://doi.org/10.1021/am900602m>.
- (79) Chai, J.; Wang, D.; Fan, X.; Buriak, J. M. Assembly of Aligned Linear Metallic Patterns on Silicon. *Nat Nano* **2007**, *2* (8), 500–506. <https://doi.org/10.1038/nnano.2007.227>.
- (80) Chai, J.; Buriak, J. M. Using Cylindrical Domains of Block Copolymers To Self-Assemble and Align Metallic Nanowires. *ACS Nano* **2008**, *2* (3), 489–501. <https://doi.org/10.1021/nm700341s>.
- (81) Aizawa, M.; Buriak, J. M. Block Copolymer Templated Chemistry for the Formation of Metallic Nanoparticle Arrays on Semiconductor Surfaces. *Chem. Mater.* **2007**, *19* (21), 5090–5101. <https://doi.org/10.1021/cm071382b>.
- (82) Mizuno, H.; Buriak, J. M. Catalytic Stamp Lithography for Sub-100 Nm Patterning of Organic Monolayers. *J. Am. Chem. Soc.* **2008**, *130* (52), 17656–17657. <https://doi.org/10.1021/ja807708r>.

- (83) Mizuno, H.; Buriak, J. M. Building Upon Patterned Organic Monolayers Produced via Catalytic Stamp Lithography. *ACS Appl. Mater. Interfaces* **2010**, *2* (8), 2301–2307. <https://doi.org/10.1021/am100348f>.
- (84) Sugimura, H.; Mo, S.; Yamashiro, K.; Ichii, T.; Murase, K. Photochemical Assembly of Gold Nanoparticle Arrays Covalently Attached to Silicon Surface Assisted by Localized Plasmon in the Nanoparticles. *J. Phys. Chem. C* **2013**, *117* (6), 2480–2485. <https://doi.org/10.1021/jp306290w>.
- (85) Liu, F.; Lubber, E. J.; Huck, L. A.; Olsen, B. C.; Buriak, J. M. Nanoscale Plasmonic Stamp Lithography on Silicon. *ACS Nano* **2015**, *9* (2), 2184–2193. <https://doi.org/10.1021/acsnano.5b00312>.
- (86) Liu, F.; Hauger, T. C.; Olsen, B. C.; Lubber, E. J.; Buriak, J. M. Polymers, Plasmons, and Patterns: Mechanism of Plasmon-Induced Hydrosilylation on Silicon. *Chem. Mater.* **2016**, *28* (24), 9158–9168. <https://doi.org/10.1021/acs.chemmater.6b04504>.
- (87) Neumann, O.; Urban, A. S.; Day, J.; Lal, S.; Nordlander, P.; Halas, N. J. Solar Vapor Generation Enabled by Nanoparticles. *ACS Nano* **2013**, *7* (1), 42–49. <https://doi.org/10.1021/nn304948h>.
- (88) Neumann, O.; Feronti, C.; Neumann, A. D.; Dong, A.; Schell, K.; Lu, B.; Kim, E.; Quinn, M.; Thompson, S.; Grady, N.; Nordlander, P.; Oden, M.; Halas, N. J. Compact Solar Autoclave Based on Steam Generation Using Broadband Light-Harvesting Nanoparticles. *PNAS* **2013**, *110* (29), 11677–11681. <https://doi.org/10.1073/pnas.1310131110>.
- (89) Halas, N. J. Hot Electron Science and Microscopic Processes in Plasmonics and Catalysis. *Faraday Discuss.* **2019**. <https://doi.org/10.1039/C9FD00001A>.
- (90) Marimuthu, A.; Zhang, J.; Linic, S. Tuning Selectivity in Propylene Epoxidation by Plasmon Mediated Photo-Switching of Cu Oxidation State. *Science* **2013**, *339* (6127), 1590–1593. <https://doi.org/10.1126/science.1231631>.
- (91) Kumari, G.; Zhang, X.; Devasia, D.; Heo, J.; Jain, P. K. Watching Visible Light-Driven CO<sub>2</sub> Reduction on a Plasmonic Nanoparticle Catalyst. *ACS Nano* **2018**, *12* (8), 8330–8340. <https://doi.org/10.1021/acsnano.8b03617>.

- (92) Choi, J.-H.; Ha, C.-W.; Choi, H.-Y.; Seong, J.-W.; Park, C.-M.; Lee, S.-M. Porous Carbon-Free SnSb Anodes for High-Performance Na-Ion Batteries. *Journal of Power Sources* **2018**, *386*, 34–39. <https://doi.org/10.1016/j.jpowsour.2018.03.032>.
- (93) Liu, Z.; Wang, X.; Qi, D.; Xu, C.; Yu, J.; Liu, Y.; Jiang, Y.; Liedberg, B.; Chen, X. High-Adhesion Stretchable Electrodes Based on Nanopile Interlocking. *Advanced Materials* **2017**, *29* (2), 1603382. <https://doi.org/10.1002/adma.201603382>.
- (94) Qi, D.; Liu, Z.; Yu, M.; Liu, Y.; Tang, Y.; Lv, J.; Li, Y.; Wei, J.; Liedberg, B.; Yu, Z.; Chen, X. Highly Stretchable Gold Nanobelts with Sinusoidal Structures for Recording Electrocardiograms. *Advanced Materials* **2015**, *27* (20), 3145–3151. <https://doi.org/10.1002/adma.201405807>.
- (95) Zhou, C.; Bette, S.; Schnakenberg, U. Flexible and Stretchable Gold Microstructures on Extra Soft Poly(Dimethylsiloxane) Substrates. *Advanced Materials* **2015**, *27* (42), 6664–6669. <https://doi.org/10.1002/adma.201502630>.
- (96) Li, Y.; Zhang, W.; Hu, J.; Wang, Y.; Feng, X.; Du, W.; Guo, M.; Liu, B.-F. Rapid Assembly of Large Scale Transparent Circuit Arrays Using PDMS Nanofilm Shaped Coffee Ring. *Advanced Functional Materials* **2017**, *27* (11), 1606045. <https://doi.org/10.1002/adfm.201606045>.
- (97) Osmani, B.; Deyhle, H.; Töpfer, T.; Pfohl, T.; Müller, B. Gold Layers on Elastomers near the Critical Stress Regime. *Advanced Materials Technologies* **2017**, *2* (10), 1700105. <https://doi.org/10.1002/admt.201700105>.
- (98) Chen, H.; Bai, L.; Li, T.; Zhao, C.; Zhang, J.; Zhang, N.; Song, G.; Gan, Q.; Xu, Y. Wearable and Robust Triboelectric Nanogenerator Based on Crumpled Gold Films. *Nano Energy* **2018**, *46*, 73–80. <https://doi.org/10.1016/j.nanoen.2018.01.032>.
- (99) Yu, C.; O'Brien, K.; Zhang, Y.-H.; Yu, H.; Jiang, H. Tunable Optical Gratings Based on Buckled Nanoscale Thin Films on Transparent Elastomeric Substrates. *Appl. Phys. Lett.* **2010**, *96* (4), 041111. <https://doi.org/10.1063/1.3298744>.
- (100) Menard, E.; Meitl, M. A.; Sun, Y.; Park, J.-U.; Shir, D. J.-L.; Nam, Y.-S.; Jeon, S.; Rogers, J. A. Micro- and Nanopatterning Techniques for Organic Electronic

- and Optoelectronic Systems. *Chem. Rev.* **2007**, *107* (4), 1117–1160. <https://doi.org/10.1021/cr050139y>.
- (101) Hung, T.-Y.; Liu, J. A.-C.; Lee, W.-H.; Li, J.-R. Hierarchical Nanoparticle Assemblies Formed via One-Step Catalytic Stamp Pattern Transfer. *ACS Appl. Mater. Interfaces* **2019**, *11* (4), 4667–4677. <https://doi.org/10.1021/acsami.8b19807>.
- (102) Rogers, J. A.; Someya, T.; Huang, Y. Materials and Mechanics for Stretchable Electronics. *Science* **2010**, *327* (5973), 1603–1607. <https://doi.org/10.1126/science.1182383>.
- (103) Ray, T. R.; Choi, J.; Bandodkar, A. J.; Krishnan, S.; Gutruf, P.; Tian, L.; Ghaffari, R.; Rogers, J. A. Bio-Integrated Wearable Systems: A Comprehensive Review. *Chem. Rev.* **2019**. <https://doi.org/10.1021/acs.chemrev.8b00573>.
- (104) Szunerits, S.; Praig, V. G.; Manesse, M.; Boukherroub, R. Gold Island Films on Indium Tin Oxide for Localized Surface Plasmon Sensing. *Nanotechnology* **2008**, *19* (19), 195712. <https://doi.org/10.1088/0957-4484/19/19/195712>.
- (105) Doron-Mor, I.; Barkay, Z.; Filip-Granit, N.; Vaskevich, A.; Rubinstein, I. Ultrathin Gold Island Films on Silanized Glass. Morphology and Optical Properties. *Chemistry of Materials* **2004**, *16* (18), 3476–3483. <https://doi.org/10.1021/cm049605a>.
- (106) Karakouz, T.; Holder, D.; Goomanovsky, M.; Vaskevich, A.; Rubinstein, I. Morphology and Refractive Index Sensitivity of Gold Island Films. *Chemistry of Materials* **2009**, *21* (24), 5875–5885. <https://doi.org/10.1021/cm902676d>.
- (107) Kedem, O.; Tesler, A. B.; Vaskevich, A.; Rubinstein, I. Sensitivity and Optimization of Localized Surface Plasmon Resonance Transducers. *ACS Nano* **2011**, *5* (2), 748–760. <https://doi.org/10.1021/nn102617d>.
- (108) Seguini, G.; Llamaja Curi, J.; Spiga, S.; Tallarida, G.; Wiemer, C.; Perego, M. Solid-State Dewetting of Ultra-Thin Au Films on SiO<sub>2</sub> and HfO<sub>2</sub>. *Nanotechnology* **2014**, *25* (49), 495603. <https://doi.org/10.1088/0957-4484/25/49/495603>.
- (109) Kunwar, S.; Sui, M.; Pandey, P.; Zhang, Q.; Li, M.-Y.; Bhandari, H.; Lee, J. Determination of Growth Regimes of Pd Nanostructures on C-Plane Sapphire by the Control of Deposition Amount at Different Annealing Temperatures. *Physical*

- Chemistry Chemical Physics* **2017**, *19* (23), 15084–15097.  
<https://doi.org/10.1039/C7CP01410D>.
- (110) Tesler, A. B.; Chuntunov, L.; Karakouz, T.; Bendikov, T. A.; Haran, G.; Vaskevich, A.; Rubinstein, I. Tunable Localized Plasmon Transducers Prepared by Thermal Dewetting of Percolated Evaporated Gold Films. *The Journal of Physical Chemistry C* **2011**, *115* (50), 24642–24652.  
<https://doi.org/10.1021/jp209114j>.
- (111) Sun, H.; Yu, M.; Wang, G.; Sun, X.; Lian, J. Temperature-Dependent Morphology Evolution and Surface Plasmon Absorption of Ultrathin Gold Island Films. *The Journal of Physical Chemistry C* **2012**, *116* (16), 9000–9008.  
<https://doi.org/10.1021/jp300260h>.
- (112) Kang, M.; Park, S.-G.; Jeong, K.-H. Repeated Solid-State Dewetting of Thin Gold Films for Nanogap-Rich Plasmonic Nanoislands. *Scientific Reports* **2015**, *5*, 14790. <https://doi.org/10.1038/srep14790>.
- (113) Tesler, A. B.; Maoz, B. M.; Feldman, Y.; Vaskevich, A.; Rubinstein, I. Solid-State Thermal Dewetting of Just-Percolated Gold Films Evaporated on Glass: Development of the Morphology and Optical Properties. *The Journal of Physical Chemistry C* **2013**, *117* (21), 11337–11346. <https://doi.org/10.1021/jp400895z>.
- (114) Graudejus, O.; Görrn, P.; Wagner, S. Controlling the Morphology of Gold Films on Poly(Dimethylsiloxane). *ACS Appl. Mater. Interfaces* **2010**, *2* (7), 1927–1933. <https://doi.org/10.1021/am1002537>.
- (115) Schedl, A. E.; Neuber, C.; Fery, A.; Schmidt, H.-W. Controlled Wrinkling of Gradient Metal Films. *Langmuir* **2018**, *34* (47), 14249–14253.  
<https://doi.org/10.1021/acs.langmuir.8b03123>.
- (116) Yu, S.; Sun, Y.; Ni, Y.; Zhang, X.; Zhou, H. Controlled Formation of Surface Patterns in Metal Films Deposited on Elasticity-Gradient PDMS Substrates. *ACS Applied Materials & Interfaces* **2016**, *8* (8), 5706–5714.  
<https://doi.org/10.1021/acsami.5b12369>.
- (117) Das, A.; Banerji, A.; Mukherjee, R. Programming Feature Size in the Thermal Wrinkling of Metal Polymer Bilayer by Modulating Substrate Viscoelasticity.

- ACS Appl. Mater. Interfaces* **2017**, *9* (27), 23255–23262.  
<https://doi.org/10.1021/acsami.7b08333>.
- (118) Li, S. J.; Wu, K.; Yuan, H. Z.; Zhang, J. Y.; Liu, G.; Sun, J. Formation of Wrinkled Patterns in Metal Films Deposited on Elastic Substrates: Tunability and Wettability. *Surf. Coat. Technol.* **2019**, *362*, 35–43.  
<https://doi.org/10.1016/j.surfcoat.2019.01.088>.
- (119) Bowden, N.; Brittain, S.; Evans, A. G.; Hutchinson, J. W.; Whitesides, G. M. Spontaneous Formation of Ordered Structures in Thin Films of Metals Supported on an Elastomeric Polymer. *Nature* **1998**, *393*, 4.
- (120) Genzer, J.; Groenewold, J. Soft Matter with Hard Skin: From Skin Wrinkles to Templating and Material Characterization. *Soft Matter* **2006**, *2* (4), 310.  
<https://doi.org/10.1039/b516741h>.
- (121) Lee, W.-K.; Jung, W.-B.; Nagel, S. R.; Odom, T. W. Stretchable Superhydrophobicity from Monolithic, Three-Dimensional Hierarchical Wrinkles. *Nano Letters* **2016**, *16* (6), 3774–3779.  
<https://doi.org/10.1021/acs.nanolett.6b01169>.
- (122) Kim, P.; Hu, Y.; Alvarenga, J.; Kolle, M.; Suo, Z.; Aizenberg, J. Rational Design of Mechano-Responsive Optical Materials by Fine Tuning the Evolution of Strain-Dependent Wrinkling Patterns. *Advanced Optical Materials* **2013**, *1* (5), 381–388. <https://doi.org/10.1002/adom.201300034>.
- (123) Cheng, X.; Meng, B.; Chen, X.; Han, M.; Chen, H.; Su, Z.; Shi, M.; Zhang, H. Single-Step Fluorocarbon Plasma Treatment-Induced Wrinkle Structure for High-Performance Triboelectric Nanogenerator. *Small* **2016**, *12* (2), 229–236.  
<https://doi.org/10.1002/sml.201502720>.
- (124) Link, S.; El-Sayed, M. A. Size and Temperature Dependence of the Plasmon Absorption of Colloidal Gold Nanoparticles. *J. Phys. Chem. B* **1999**, *103* (21), 4212–4217. <https://doi.org/10.1021/jp984796o>.
- (125) Orendorff, C. J.; Sau, T. K.; Murphy, C. J. Shape-Dependent Plasmon-Resonant Gold Nanoparticles. *Small* **2006**, *2* (5), 636–639.  
<https://doi.org/10.1002/sml.200500299>.

- (126) Porter, L. A.; Buriak, J. M. Harnessing Synthetic Versatility Toward Intelligent Interfacial Design: Organic Functionalization of Nanostructured Silicon Surfaces. In *Chemistry of Nanostructured Materials*; Yang, P., Ed.; World Scientific, 2004.
- (127) Sayed, S. Y.; Wang, F.; Malac, M.; Meldrum, A.; Egerton, R. F.; Buriak, J. M. Heteroepitaxial Growth of Gold Nanostructures on Silicon by Galvanic Displacement. *ACS Nano* **2009**, *3* (9), 2809–2817. <https://doi.org/10.1021/nn900685a>.
- (128) Jalali, H.; Gates, B. D. Monitoring and Mapping Imperfections in Silane-Based Self-Assembled Monolayers by Chemical Amplification. *Langmuir* **2009**, *25* (16), 9078–9084. <https://doi.org/10.1021/la900443c>.
- (129) Chockalingam, M.; Darwish, N.; Le Saux, G.; Gooding, J. J. Importance of the Indium Tin Oxide Substrate on the Quality of Self-Assembled Monolayers Formed from Organophosphonic Acids. *Langmuir* **2011**, *27* (6), 2545–2552. <https://doi.org/10.1021/la104464w>.
- (130) Ueno, K.; Misawa, H. Surface Plasmon-Enhanced Photochemical Reactions. *Journal of Photochemistry and Photobiology C: Photochemistry Reviews* **2013**, *15*, 31–52. <https://doi.org/10.1016/j.jphotochemrev.2013.04.001>.
- (131) Atwater, H. A.; Polman, A. Plasmonics for Improved Photovoltaic Devices. *Nature Materials* **2010**, *9* (3), 205–213. <https://doi.org/10.1038/nmat2629>.
- (132) Willets, K. A.; Wilson, A. J.; Sundaresan, V.; Joshi, P. B. Super-Resolution Imaging and Plasmonics. *Chem. Rev.* **2017**, *117* (11), 7538–7582. <https://doi.org/10.1021/acs.chemrev.6b00547>.
- (133) Juan, M. L.; Righini, M.; Quidant, R. Plasmon Nano-Optical Tweezers. *Nature Photonics* **2011**, *5* (6), 349–356. <https://doi.org/10.1038/nphoton.2011.56>.
- (134) Jeong, M.; Doris, B.; Kedzierski, J.; Rim, K.; Yang, M. Silicon Device Scaling to the Sub-10-Nm Regime. *Science* **2004**, *306* (5704), 2057–2060. <https://doi.org/10.1126/science.1100731>.
- (135) Wang, J.; Zhou, Y.; Watkinson, M.; Gautrot, J.; Krause, S. High-Sensitivity Light-Addressable Potentiometric Sensors Using Silicon on Sapphire Functionalized with Self-Assembled Organic Monolayers. *Sensors and Actuators B: Chemical* **2015**, *209*, 230–236. <https://doi.org/10.1016/j.snb.2014.11.071>.

- (136) Kanyong, P.; Sun, G.; Rösicke, F.; Syritski, V.; Panne, U.; Hinrichs, K.; Rappich, J. Maleimide Functionalized Silicon Surfaces for Biosensing Investigated by In-Situ IRSE and EQCM. *Electrochemistry Communications* **2015**, *51*, 103–107. <https://doi.org/10.1016/j.elecom.2014.12.015>.
- (137) Bruce, J. P.; Oliver, D. R.; Lewis, N. S.; Freund, M. S. Electrical Characteristics of the Junction between PEDOT:PSS and Thiophene-Functionalized Silicon Microwires. *ACS Appl. Mater. Interfaces* **2015**, *7* (49), 27160–27166. <https://doi.org/10.1021/acsami.5b07725>.
- (138) Kang, O. S.; Bruce, J. P.; Herbert, D. E.; Freund, M. S. Covalent Attachment of Ferrocene to Silicon Microwire Arrays. *ACS Appl. Mater. Interfaces* **2015**, *7* (48), 26959–26967. <https://doi.org/10.1021/acsami.5b07814>.
- (139) Vilan, A.; Yaffe, O.; Biller, A.; Salomon, A.; Kahn, A.; Cahen, D. Molecules on Si: Electronics with Chemistry. *Advanced Materials* **2010**, *22* (2), 140–159. <https://doi.org/10.1002/adma.200901834>.
- (140) Dasog, M.; Bader, K.; Veinot, J. G. C. Influence of Halides on the Optical Properties of Silicon Quantum Dots. *Chem. Mater.* **2015**, *27* (4), 1153–1156. <https://doi.org/10.1021/acs.chemmater.5b00115>.
- (141) Fermi, A.; Locritani, M.; Carlo, G. D.; Pizzotti, M.; Caramori, S.; Yu, Y.; Korgel, B. A.; Bergamini, G.; Ceroni, P. Light-Harvesting Antennae Based on Photoactive Silicon Nanocrystals Functionalized with Porphyrin Chromophores. *Faraday Discuss.* **2015**, *185* (0), 481–495. <https://doi.org/10.1039/C5FD00098J>.
- (142) Rao, C.; Lubber, E. J.; Olsen, B. C.; Buriak, J. M. Plasmonic Stamps Fabricated by Gold Dewetting on PDMS for Catalyzing Hydrosilylation on Silicon Surfaces. *ACS Appl. Nano Mater.* **2019**, *2* (5), 3238–3245. <https://doi.org/10.1021/acsanm.9b00538>.
- (143) Joseph, V.; Engelbrekt, C.; Zhang, J.; Gernert, U.; Ulstrup, J.; Kneipp, J. Characterizing the Kinetics of Nanoparticle-Catalyzed Reactions by Surface-Enhanced Raman Scattering. *Angewandte Chemie International Edition* **2012**, *51* (30), 7592–7596. <https://doi.org/10.1002/anie.201203526>.
- (144) Cui, Q.; Yashchenok, A.; Li, L.; Möhwald, H.; Bargheer, M. Mechanistic Study on Reduction Reaction of Nitro Compounds Catalyzed by Gold Nanoparticles

- Using in Situ SERS Monitoring. *Colloids and Surfaces A: Physicochemical and Engineering Aspects* **2015**, *470*, 108–113. <https://doi.org/10.1016/j.colsurfa.2015.01.075>.
- (145) Heck, K. N.; Janesko, B. G.; Scuseria, G. E.; Halas, N. J.; Wong, M. S. Observing Metal-Catalyzed Chemical Reactions in Situ Using Surface-Enhanced Raman Spectroscopy on Pd–Au Nanoshells. *J. Am. Chem. Soc.* **2008**, *130* (49), 16592–16600. <https://doi.org/10.1021/ja803556k>.
- (146) Kumar, N.; Stephanidis, B.; Zenobi, R.; J. Wain, A.; Roy, D. Nanoscale Mapping of Catalytic Activity Using Tip-Enhanced Raman Spectroscopy. *Nanoscale* **2015**, *7* (16), 7133–7137. <https://doi.org/10.1039/C4NR07441F>.
- (147) Li, P.; Ma, B.; Yang, L.; Liu, J. Hybrid Single Nanoreactor for in Situ SERS Monitoring of Plasmon-Driven and Small Au Nanoparticles Catalyzed Reactions. *Chemical Communications* **2015**, *51* (57), 11394–11397. <https://doi.org/10.1039/C5CC03792A>.
- (148) Qiu, L.; Pang, G. A.; Zheng, G.; Bauer, D.; Wieland, K.; Haisch, C. Kinetic and Mechanistic Investigation of the Photocatalyzed Surface Reduction of 4-Nitrothiophenol Observed on a Silver Plasmonic Film via Surface-Enhanced Raman Scattering. *ACS Appl. Mater. Interfaces* **2020**, *12* (18), 21133–21142. <https://doi.org/10.1021/acsami.0c05977>.
- (149) Ren, X.; Tan, E.; Lang, X.; You, T.; Jiang, L.; Zhang, H.; Yin, P.; Guo, L. Observing Reduction of 4-Nitrobenzenthiole on Gold Nanoparticles in Situ Using Surface-Enhanced Raman Spectroscopy. *Physical Chemistry Chemical Physics* **2013**, *15* (34), 14196–14201. <https://doi.org/10.1039/C3CP51385H>.
- (150) Tang, X.; Cai, W.; Yang, L.; Liu, J. Monitoring Plasmon-Driven Surface Catalyzed Reactions in Situ Using Time-Dependent Surface-Enhanced Raman Spectroscopy on Single Particles of Hierarchical Peony-like Silver Microflowers. *Nanoscale* **2014**, *6* (15), 8612–8616. <https://doi.org/10.1039/C4NR01939C>.
- (151) Sheng, S.; Ji, Y.; Yan, X.; Wei, H.; Luo, Y.; Xu, H. Azo-Dimerization Mechanisms of p-Aminothiophenol and p-Nitrothiophenol Molecules on Plasmonic Metal Surfaces Revealed by Tip-/Surface-Enhanced Raman

- Spectroscopy. *J. Phys. Chem. C* **2020**, *124* (21), 11586–11594. <https://doi.org/10.1021/acs.jpcc.0c01367>.
- (152) Shi, Z.; Zhang, Y.; Liu, M.; Hanaor, D. A. H.; Gan, Y. Dynamic Contact Angle Hysteresis in Liquid Bridges. *Colloids and Surfaces A: Physicochemical and Engineering Aspects* **2018**, *555*, 365–371. <https://doi.org/10.1016/j.colsurfa.2018.07.004>.
- (153) Yam, C. M.; Tong, S. S. Y.; Kakkar, A. K. Simple Acid–Base Hydrolytic Chemistry Approach to Molecular Self-Assembly: Thin Films of Long Chain Alcohols Terminated with Alkyl, Phenyl, and Acetylene Groups on Inorganic Oxides Surfaces. *Langmuir* **1998**, *14* (24), 6941–6947. <https://doi.org/10.1021/la9806909>.
- (154) Chibowski, E. J. Surface Free Energy and Wettability of Silyl Layers on Silicon Determined from Contact Angle Hysteresis. *Advances in Colloid and Interface Science* **2005**, *113* (2), 121–131. <https://doi.org/10.1016/j.cis.2005.01.005>.
- (155) Huck, L. A.; Buriak, J. M. UV-Initiated Hydrosilylation on Hydrogen-Terminated Silicon (111): Rate Coefficient Increase of Two Orders of Magnitude in the Presence of Aromatic Electron Acceptors. *Langmuir* **2012**, *28* (47), 16285–16293. <https://doi.org/10.1021/la3035819>.
- (156) Huck, L. A.; Buriak, J. M. Toward a Mechanistic Understanding of Exciton-Mediated Hydrosilylation on Nanocrystalline Silicon. *J. Am. Chem. Soc.* **2012**, *134* (1), 489–497. <https://doi.org/10.1021/ja208604r>.
- (157) Wu, N. L. Y.; Zhang, X.; Murphy, J. N.; Chai, J.; Harris, K. D.; Buriak, J. M. Density Doubling of Block Copolymer Templated Features. *Nano Lett.* **2012**, *12* (1), 264–268. <https://doi.org/10.1021/nl203488a>.
- (158) Gole, A.; Murphy, C. J. Seed-Mediated Synthesis of Gold Nanorods: Role of the Size and Nature of the Seed. *Chem. Mater.* **2004**, *16* (19), 3633–3640. <https://doi.org/10.1021/cm0492336>.
- (159) Rao, C.; Wang, Z.-G.; Li, N.; Zhang, W.; Xu, X.; Ding, B. Tunable Optical Activity of Plasmonic Dimers Assembled by DNA Origami. *Nanoscale* **2015**, *7* (20), 9147–9152. <https://doi.org/10.1039/C5NR01634G>.

- (160) Mahpeykar, S. M.; Xiong, Q.; Wei, J.; Meng, L.; Russell, B. K.; Hermansen, P.; Singhal, A. V.; Wang, X. Stretchable Hexagonal Diffraction Gratings as Optical Diffusers for In Situ Tunable Broadband Photon Management. *Advanced Optical Materials* **2016**, *4* (7), 1106–1114. <https://doi.org/10.1002/adom.201600122>.
- (161) Fetterly, C. R.; Olsen, B. C.; Luber, E. J.; Buriak, J. M. Vapor-Phase Nanopatterning of Aminosilanes with Electron Beam Lithography: Understanding and Minimizing Background Functionalization. *Langmuir* **2018**, *34* (16), 4780–4792. <https://doi.org/10.1021/acs.langmuir.8b00679>.
- (162) Riikonen, J.; Salomäki, M.; van Wonderen, J.; Kemell, M.; Xu, W.; Korhonen, O.; Ritala, M.; MacMillan, F.; Salonen, J.; Lehto, V.-P. Surface Chemistry, Reactivity, and Pore Structure of Porous Silicon Oxidized by Various Methods. *Langmuir* **2012**, *28* (28), 10573–10583. <https://doi.org/10.1021/la301642w>.
- (163) Kolasinski, K. W. The Mechanism of Photohydrosilylation on Silicon and Porous Silicon Surfaces. *J. Am. Chem. Soc.* **2013**, *135* (30), 11408–11412. <https://doi.org/10.1021/ja406063n>.
- (164) Sze, S. M.; Ng, K. K. *Physics of Semiconductor Devices*, 3 edition.; Wiley-Interscience: Hoboken, N.J, 2006.
- (165) World — The World Factbook - Central Intelligence Agency <https://www.cia.gov/library/publications/the-world-factbook/geos/xx.html> (accessed May 20, 2020).
- (166) Hammerschmidt, E. G. Formation of Gas Hydrates in Natural Gas Transmission Lines. *Ind. Eng. Chem.* **1934**, *26* (8), 851–855. <https://doi.org/10.1021/ie50296a010>.
- (167) Mokhatab, S.; Poe, W. A. *Handbook of Natural Gas Transmission and Processing*; Gulf Professional Publishing, 2012.
- (168) Steele, B. C. H. Running on Natural Gas. *Nature* **1999**, *400* (6745), 619–621. <https://doi.org/10.1038/23144>.
- (169) US EPA, O. Overview of Greenhouse Gases <https://www.epa.gov/ghgemissions/overview-greenhouse-gases> (accessed May 20, 2020).

- (170) Burnham, A.; Han, J.; Clark, C. E.; Wang, M.; Dunn, J. B.; Palou-Rivera, I. Life-Cycle Greenhouse Gas Emissions of Shale Gas, Natural Gas, Coal, and Petroleum. *Environ. Sci. Technol.* **2012**, *46* (2), 619–627. <https://doi.org/10.1021/es201942m>.
- (171) Brandt, A. R.; Heath, G. A.; Kort, E. A.; O’Sullivan, F.; Pétron, G.; Jordaan, S. M.; Tans, P.; Wilcox, J.; Gopstein, A. M.; Arent, D.; Wofsy, S.; Brown, N. J.; Bradley, R.; Stucky, G. D.; Eardley, D.; Harriss, R. Methane Leaks from North American Natural Gas Systems. *Science* **2014**, *343* (6172), 733–735. <https://doi.org/10.1126/science.1247045>.
- (172) Colborn, T.; Kwiatkowski, C.; Schultz, K.; Bachran, M. Natural Gas Operations from a Public Health Perspective. *Human and Ecological Risk Assessment: An International Journal* **2011**, *17* (5), 1039–1056. <https://doi.org/10.1080/10807039.2011.605662>.
- (173) Economides, M. J.; Wood, D. A. The State of Natural Gas. *Journal of Natural Gas Science and Engineering* **2009**, *1* (1), 1–13. <https://doi.org/10.1016/j.jngse.2009.03.005>.
- (174) Chen, J.; Arandiyan, H.; Gao, X.; Li, J. Recent Advances in Catalysts for Methane Combustion. *Catal Surv Asia* **2015**, *19* (3), 140–171. <https://doi.org/10.1007/s10563-015-9191-5>.
- (175) Gélin, P.; Primet, M. Complete Oxidation of Methane at Low Temperature over Noble Metal Based Catalysts: A Review. *Applied Catalysis B: Environmental* **2002**, *39* (1), 1–37. [https://doi.org/10.1016/S0926-3373\(02\)00076-0](https://doi.org/10.1016/S0926-3373(02)00076-0).
- (176) Ciuparu, D.; Lyubovsky, M. R.; Altman, E.; Pfefferle, L. D.; Datye, A. Catalytic Combustion of Methane Over Palladium-Based Catalysts. *Catalysis Reviews* **2002**, *44* (4), 593–649. <https://doi.org/10.1081/CR-120015482>.
- (177) Ross, J. R. H.; van Keulen, A. N. J.; Hegarty, M. E. S.; Seshan, K. The Catalytic Conversion of Natural Gas to Useful Products. *Catalysis Today* **1996**, *30* (1), 193–199. [https://doi.org/10.1016/0920-5861\(96\)00035-1](https://doi.org/10.1016/0920-5861(96)00035-1).
- (178) Hayhoe, K.; Kheshgi, H. S.; Jain, A. K.; Wuebbles, D. J. Substitution of Natural Gas for Coal: Climatic Effects of Utility Sector Emissions. *Climatic Change* **2002**, *54* (1), 107–139. <https://doi.org/10.1023/A:1015737505552>.

- (179) Choudhary, T. V.; Banerjee, S.; Choudhary, V. R. Catalysts for Combustion of Methane and Lower Alkanes. *Applied Catalysis A: General* **2002**, *234* (1), 1–23. [https://doi.org/10.1016/S0926-860X\(02\)00231-4](https://doi.org/10.1016/S0926-860X(02)00231-4).
- (180) Hayes, R. E.; Kolaczkowski, S. T. *Introduction to Catalytic Combustion*; CRC Press, 1998.
- (181) Vaillant, S. R.; Gastec, A. S. Catalytic Combustion in a Domestic Natural Gas Burner. *Catalysis Today* **1999**, *47* (1), 415–420. [https://doi.org/10.1016/S0920-5861\(98\)00324-1](https://doi.org/10.1016/S0920-5861(98)00324-1).
- (182) Neyestanaki, A. K.; Kumar, N.; Lindfors, L.-E. Catalytic Combustion of Propane and Natural Gas over Cu and Pd Modified ZSM Zeolite Catalysts. *Applied Catalysis B: Environmental* **1995**, *7* (1), 95–111. [https://doi.org/10.1016/0926-3373\(95\)00029-1](https://doi.org/10.1016/0926-3373(95)00029-1).
- (183) Cerri, I.; Saracco, G.; Specchia, V.; Trimis, D. Improved-Performance Knitted Fibre Mats as Supports for Pre-Mixed Natural Gas Catalytic Combustion. *Chemical Engineering Journal* **2001**, *82* (1), 73–85. [https://doi.org/10.1016/S1385-8947\(00\)00344-2](https://doi.org/10.1016/S1385-8947(00)00344-2).
- (184) Fujimoto, K.; Ribeiro, F. H.; Avalos-Borja, M.; Iglesia, E. Structure and Reactivity of PdOx/ZrO<sub>2</sub> Catalysts for Methane Oxidation at Low Temperatures. *Journal of Catalysis* **1998**, *179* (2), 431–442. <https://doi.org/10.1006/jcat.1998.2178>.
- (185) Escandón, L. S.; Niño, D.; Díaz, E.; Ordóñez, S.; Díez, F. V. Effect of Hydrothermal Ageing on the Performance of Ce-Promoted PdO/ZrO<sub>2</sub> for Methane Combustion. *Catalysis Communications* **2008**, *9* (13), 2291–2296. <https://doi.org/10.1016/j.catcom.2008.05.026>.
- (186) Xu, Q.; Kharas, K. C.; Croley, B. J.; Datye, A. K. The Sintering of Supported Pd Automotive Catalysts. *ChemCatChem* **2011**, *3* (6), 1004–1014. <https://doi.org/10.1002/cctc.201000392>.
- (187) Euzen, P.; Le Gal, J.-H.; Rebours, B.; Martin, G. Deactivation of Palladium Catalyst in Catalytic Combustion of Methane. *Catalysis Today* **1999**, *47* (1), 19–27. [https://doi.org/10.1016/S0920-5861\(98\)00280-6](https://doi.org/10.1016/S0920-5861(98)00280-6).

- (188) Sekizawa, K.; Eguchi, K.; Widjaja, H.; Machida, M.; Arai, H. Property of Pd-Supported Catalysts for Catalytic Combustion. *Catalysis Today* **1996**, *28* (3), 245–250. [https://doi.org/10.1016/0920-5861\(95\)00241-3](https://doi.org/10.1016/0920-5861(95)00241-3).
- (189) Brown, S. P. A.; Yucel, M. K. What Drives Natural Gas Prices? *EJ* **2008**, *29* (2). <https://doi.org/10.5547/ISSN0195-6574-EJ-Vol29-No2-3>.
- (190) Shen, J.; Hayes, R. E.; Wu, X.; Semagina, N. 100° Temperature Reduction of Wet Methane Combustion: Highly Active Pd–Ni/Al<sub>2</sub>O<sub>3</sub> Catalyst versus Pd/NiAl<sub>2</sub>O<sub>4</sub>. *ACS Catal.* **2015**, *5* (5), 2916–2920. <https://doi.org/10.1021/acscatal.5b00060>.
- (191) Védrine, J. C. Heterogeneous Catalysis on Metal Oxides. *Catalysts* **2017**, *7* (11), 341. <https://doi.org/10.3390/catal7110341>.
- (192) Weitkamp, J. Zeolites and Catalysis. *Solid State Ionics* **2000**, *131* (1), 175–188. [https://doi.org/10.1016/S0167-2738\(00\)00632-9](https://doi.org/10.1016/S0167-2738(00)00632-9).
- (193) Figueiredo, J. L.; Pereira, M. F. R.; Freitas, M. M. A.; Órfão, J. J. M. Characterization of Active Sites on Carbon Catalysts. *Ind. Eng. Chem. Res.* **2007**, *46* (12), 4110–4115. <https://doi.org/10.1021/ie061071v>.
- (194) A. Arnold, R.; M. Hill, J. Catalysts for Gasification: A Review. *Sustainable Energy & Fuels* **2019**, *3* (3), 656–672. <https://doi.org/10.1039/C8SE00614H>.
- (195) Aramouni, N. A. K.; Touma, J. G.; Tarboush, B. A.; Zeaiter, J.; Ahmad, M. N. Catalyst Design for Dry Reforming of Methane: Analysis Review. *Renewable and Sustainable Energy Reviews* **2018**, *82*, 2570–2585. <https://doi.org/10.1016/j.rser.2017.09.076>.
- (196) Ren, J.; Cao, J.-P.; Zhao, X.-Y.; Yang, F.-L.; Wei, X.-Y. Recent Advances in Syngas Production from Biomass Catalytic Gasification: A Critical Review on Reactors, Catalysts, Catalytic Mechanisms and Mathematical Models. *Renewable and Sustainable Energy Reviews* **2019**, *116*, 109426. <https://doi.org/10.1016/j.rser.2019.109426>.
- (197) Jung, N.; Chung, D. Y.; Ryu, J.; Yoo, S. J.; Sung, Y.-E. Pt-Based Nanoarchitecture and Catalyst Design for Fuel Cell Applications. *Nano Today* **2014**, *9* (4), 433–456. <https://doi.org/10.1016/j.nantod.2014.06.006>.

- (198) Fang, B.; Kim, J. H.; Kim, M.-S.; Yu, J.-S. Hierarchical Nanostructured Carbons with Meso–Macroporosity: Design, Characterization, and Applications. *Acc. Chem. Res.* **2013**, *46* (7), 1397–1406. <https://doi.org/10.1021/ar300253f>.
- (199) Tang, J.; Liu, J.; Torad, N. L.; Kimura, T.; Yamauchi, Y. Tailored Design of Functional Nanoporous Carbon Materials toward Fuel Cell Applications. *Nano Today* **2014**, *9* (3), 305–323. <https://doi.org/10.1016/j.nantod.2014.05.003>.
- (200) Lefevre, J.; Gysen, M.; Mullens, S.; Meynen, V.; Van Noyen, J. The Benefit of Design of Support Architectures for Zeolite Coated Structured Catalysts for Methanol-to-Olefin Conversion. *Catalysis Today* **2013**, *216*, 18–23. <https://doi.org/10.1016/j.cattod.2013.05.020>.
- (201) Lee, I.; Zhang, Q.; Ge, J.; Yin, Y.; Zaera, F. Encapsulation of Supported Pt Nanoparticles with Mesoporous Silica for Increased Catalyst Stability. *Nano Res.* **2011**, *4* (1), 115–123. <https://doi.org/10.1007/s12274-010-0059-8>.
- (202) Joo, S. H.; Park, J. Y.; Tsung, C.-K.; Yamada, Y.; Yang, P.; Somorjai, G. A. Thermally Stable Pt/Mesoporous Silica Core–Shell Nanocatalysts for High-Temperature Reactions. *Nature Mater* **2009**, *8* (2), 126–131. <https://doi.org/10.1038/nmat2329>.
- (203) Ge, J.; Zhang, Q.; Zhang, T.; Yin, Y. Core–Satellite Nanocomposite Catalysts Protected by a Porous Silica Shell: Controllable Reactivity, High Stability, and Magnetic Recyclability. *Angewandte Chemie International Edition* **2008**, *47* (46), 8924–8928. <https://doi.org/10.1002/anie.200803968>.
- (204) Zhang, Q.; Lee, I.; Ge, J.; Zaera, F.; Yin, Y. Surface-Protected Etching of Mesoporous Oxide Shells for the Stabilization of Metal Nanocatalysts. *Advanced Functional Materials* **2010**, *20* (14), 2201–2214. <https://doi.org/10.1002/adfm.201000428>.
- (205) Cargnello, M.; Jaén, J. J. D.; Garrido, J. C. H.; Bakhmutsky, K.; Montini, T.; Gámez, J. J. C.; Gorte, R. J.; Fornasiero, P. Exceptional Activity for Methane Combustion over Modular Pd@CeO<sub>2</sub> Subunits on Functionalized Al<sub>2</sub>O<sub>3</sub>. *Science* **2012**, *337* (6095), 713–717. <https://doi.org/10.1126/science.1222887>.
- (206) Prieto, G.; Zečević, J.; Friedrich, H.; Jong, K. P. de; Jongh, P. E. de. Towards Stable Catalysts by Controlling Collective Properties of Supported Metal

- Nanoparticles. *Nature Mater* **2013**, *12* (1), 34–39.  
<https://doi.org/10.1038/nmat3471>.
- (207) Habibi, A. H.; Hayes, R. E.; Semagina, N. Bringing Attention to Metal (Un)Availability in Encapsulated Catalysts. *Catal. Sci. Technol.* **2018**, *8* (3), 798–805. <https://doi.org/10.1039/C7CY01919J>.
- (208) Habibi, A. H.; Hayes, R. E.; Semagina, N. Evaluation of Hydrothermal Stability of Encapsulated PdPt@SiO<sub>2</sub> Catalyst for Lean CH<sub>4</sub> Combustion. *Applied Catalysis A: General* **2018**, *556*, 129–136.  
<https://doi.org/10.1016/j.apcata.2018.02.034>.
- (209) Habibi, A. H.; Semagina, N.; Hayes, R. E. Kinetics of Low-Temperature Methane Oxidation over SiO<sub>2</sub>-Encapsulated Bimetallic Pd–Pt Nanoparticles. *Ind. Eng. Chem. Res.* **2018**, *57* (24), 8160–8171.  
<https://doi.org/10.1021/acs.iecr.8b01338>.
- (210) Feng, X.; Li, W.; Liu, D.; Zhang, Z.; Duan, Y.; Zhang, Y. Self-Assembled Pd@CeO<sub>2</sub>/γ-Al<sub>2</sub>O<sub>3</sub> Catalysts with Enhanced Activity for Catalytic Methane Combustion. *Small* **2017**, *13* (31), 1700941.  
<https://doi.org/10.1002/sml.201700941>.
- (211) Guo, T.; Nie, X.; Du, J.; Li, J. Enhanced Properties of Pd/CeO<sub>2</sub>-Nanorods Modified with Alkaline-Earth Metals for Catalytic Oxidation of Low-Concentration Methane. *RSC Advances* **2018**, *8* (67), 38641–38647.  
<https://doi.org/10.1039/C8RA07797E>.
- (212) Ali, S.; Al-Marri, M. J.; Al-Jaber, A. S.; Abdelmoneim, A. G.; Khader, M. M. Synthesis, Characterization and Performance of Pd-Based Core-Shell Methane Oxidation Nano-Catalysts. *Journal of Natural Gas Science and Engineering* **2018**, *55*, 625–633. <https://doi.org/10.1016/j.jngse.2018.01.023>.
- (213) Chen, C.; Yeh, Y.-H.; Cargnello, M.; Murray, C. B.; Fornasiero, P.; Gorte, R. J. Methane Oxidation on Pd@ZrO<sub>2</sub>/Si–Al<sub>2</sub>O<sub>3</sub> Is Enhanced by Surface Reduction of ZrO<sub>2</sub>. *ACS Catalysis* **2014**, *4* (11), 3902–3909.  
<https://doi.org/10.1021/cs501146u>.

- (214) Li, Y.; Shi, J. Hollow-Structured Mesoporous Materials: Chemical Synthesis, Functionalization and Applications. *Advanced Materials* **2014**, *26* (20), 3176–3205. <https://doi.org/10.1002/adma.201305319>.
- (215) Lin, L.-S.; Song, J.; Yang, H.-H.; Chen, X. Yolk–Shell Nanostructures: Design, Synthesis, and Biomedical Applications. *Advanced Materials* **2018**, *30* (6), 1704639. <https://doi.org/10.1002/adma.201704639>.
- (216) Prieto, G.; Tüysüz, H.; Duyckaerts, N.; Knossalla, J.; Wang, G.-H.; Schüth, F. Hollow Nano- and Microstructures as Catalysts. *Chemical Reviews* **2016**, *116* (22), 14056–14119. <https://doi.org/10.1021/acs.chemrev.6b00374>.
- (217) Knossalla, J.; Jalalpoor, D.; Schüth, F. Hands-on Guide to the Synthesis of Mesoporous Hollow Graphitic Spheres and Core–Shell Materials. *Chemistry of Materials* **2017**, *29* (17), 7062–7072. <https://doi.org/10.1021/acs.chemmater.7b02645>.
- (218) Yu, L.; Yu, X. Y.; Lou, X. W. (David). The Design and Synthesis of Hollow Micro-/Nanostructures: Present and Future Trends. *Advanced Materials* **2018**, *30* (38). <https://doi.org/10.1002/adma.201800939>.
- (219) Arnal, P. M.; Comotti, M.; Schüth, F. High-Temperature-Stable Catalysts by Hollow Sphere Encapsulation. *Angewandte Chemie International Edition* **2006**, *45* (48), 8224–8227. <https://doi.org/10.1002/anie.200603507>.
- (220) Liu, J.; Yang, H. Q.; Kleitz, F.; Chen, Z. G.; Yang, T.; Strounina, E.; Lu, G. Q. (Max); Qiao, S. Z. Yolk–Shell Hybrid Materials with a Periodic Mesoporous Organosilica Shell: Ideal Nanoreactors for Selective Alcohol Oxidation. *Advanced Functional Materials* **2012**, *22* (3), 591–599. <https://doi.org/10.1002/adfm.201101900>.
- (221) Lee, J.; Park, J. C.; Song, H. A Nanoreactor Framework of a Au@SiO<sub>2</sub> Yolk/Shell Structure for Catalytic Reduction of p-Nitrophenol. *Advanced Materials* **2008**, *20* (8), 1523–1528. <https://doi.org/10.1002/adma.200702338>.
- (222) Lee, J.; Park, J. C.; Bang, J. U.; Song, H. Precise Tuning of Porosity and Surface Functionality in Au@SiO<sub>2</sub> Nanoreactors for High Catalytic Efficiency. *Chem. Mater.* **2008**, *20* (18), 5839–5844. <https://doi.org/10.1021/cm801149w>.

- (223) Guan, B.; Wang, X.; Xiao, Y.; Liu, Y.; Huo, Q. A Versatile Cooperative Template-Directed Coating Method to Construct Uniform Microporous Carbon Shells for Multifunctional Core–Shell Nanocomposites. *Nanoscale* **2013**, *5* (6), 2469. <https://doi.org/10.1039/c3nr34041d>.
- (224) Evangelista, V.; Acosta, B.; Miridonov, S.; Smolentseva, E.; Fuentes, S.; Simakov, A. Highly Active Au-CeO<sub>2</sub>@ZrO<sub>2</sub> Yolk–Shell Nanoreactors for the Reduction of 4-Nitrophenol to 4-Aminophenol. *Applied Catalysis B: Environmental* **2015**, *166–167*, 518–528. <https://doi.org/10.1016/j.apcatb.2014.12.006>.
- (225) Mei, L.-P.; Wang, R.; Song, P.; Feng, J.-J.; Wang, Z.-G.; Chen, J.-R.; Wang, A.-J. One-Pot Solvothermal Synthesis of Bimetallic Yolk–Shell Ni@PtNi Nanocrystals Supported on Reduced Graphene Oxide and Their Excellent Catalytic Properties for p -Nitrophenol Reduction. *New Journal of Chemistry* **2016**, *40* (3), 2315–2320. <https://doi.org/10.1039/C5NJ02923F>.
- (226) Yang, Y.; Liu, J.; Li, X.; Liu, X.; Yang, Q. Organosilane-Assisted Transformation from Core–Shell to Yolk–Shell Nanocomposites. *Chem. Mater.* **2011**, *23* (16), 3676–3684. <https://doi.org/10.1021/cm201182d>.
- (227) Liu, J.; Zhang Qiao, S.; Song Chen, J.; Lou, X. W. (David); Xing, X.; Lu, G. Q. (Max). Yolk/Shell Nanoparticles: New Platforms for Nanoreactors, Drug Delivery and Lithium-Ion Batteries. *Chemical Communications* **2011**, *47* (47), 12578–12591. <https://doi.org/10.1039/C1CC13658E>.
- (228) Wu, S.; Dzubiella, J.; Kaiser, J.; Drechsler, M.; Guo, X.; Ballauff, M.; Lu, Y. Thermosensitive Au-PNIPA Yolk–Shell Nanoparticles with Tunable Selectivity for Catalysis. *Angewandte Chemie International Edition* **2012**, *51* (9), 2229–2233. <https://doi.org/10.1002/anie.201106515>.
- (229) Hu, Y.; Tao, K.; Wu, C.; Zhou, C.; Yin, H.; Zhou, S. Size-Controlled Synthesis of Highly Stable and Active Pd@SiO<sub>2</sub> Core–Shell Nanocatalysts for Hydrogenation of Nitrobenzene. *J. Phys. Chem. C* **2013**, *117* (17), 8974–8982. <https://doi.org/10.1021/jp3110375>.

- (230) Abbasi, R.; Wu, L.; Wanke, S. E.; Hayes, R. E. Kinetics of Methane Combustion over Pt and Pt–Pd Catalysts. *Chemical Engineering Research and Design* **2012**, *90* (11), 1930–1942. <https://doi.org/10.1016/j.cherd.2012.03.003>.
- (231) Park, J.-H.; Cho, J. H.; Kim, Y. J.; Kim, E. S.; Han, H. S.; Shin, C.-H. Hydrothermal Stability of Pd/ZrO<sub>2</sub> Catalysts for High Temperature Methane Combustion. *Applied Catalysis B: Environmental* **2014**, *160–161*, 135–143. <https://doi.org/10.1016/j.apcatb.2014.05.013>.
- (232) Li, W.; Lin, Y.; Zhang, Y. Promoting Effect of Water Vapor on Catalytic Oxidation of Methane over Cobalt/Manganese Mixed Oxides. *Catalysis Today* **2003**, *83* (1), 239–245. [https://doi.org/10.1016/S0920-5861\(03\)00244-X](https://doi.org/10.1016/S0920-5861(03)00244-X).
- (233) Ciuparu, D.; Pfefferle, L. Support and Water Effects on Palladium Based Methane Combustion Catalysts. *Applied Catalysis A: General* **2001**, *209* (1), 415–428. [https://doi.org/10.1016/S0926-860X\(00\)00783-3](https://doi.org/10.1016/S0926-860X(00)00783-3).
- (234) Araya, P.; Guerrero, S.; Robertson, J.; Gracia, F. J. Methane Combustion over Pd/SiO<sub>2</sub> Catalysts with Different Degrees of Hydrophobicity. *Applied Catalysis A: General* **2005**, *283* (1), 225–233. <https://doi.org/10.1016/j.apcata.2005.01.009>.
- (235) Arnal, P. M.; Weidenthaler, C.; Schüth, F. Highly Monodisperse Zirconia-Coated Silica Spheres and Zirconia/Silica Hollow Spheres with Remarkable Textural Properties. *Chem. Mater.* **2006**, *18* (11), 2733–2739. <https://doi.org/10.1021/cm052580a>.
- (236) Seo, M.; Kim, S.; Jeong, H. E.; Lee, D.-W.; Lee, K.-Y. A Yolk–Shell Structured Pd@void@ZrO<sub>2</sub> Catalyst for Direct Synthesis of Hydrogen Peroxide from Hydrogen and Oxygen. *Journal of Molecular Catalysis A: Chemical* **2016**, *413*, 1–6. <https://doi.org/10.1016/j.molcata.2015.12.004>.
- (237) Ozawa, Y.; Tochihara, Y.; Watanabe, A.; Nagai, M.; Omi, S. Deactivation of Pt–PdO/Al<sub>2</sub>O<sub>3</sub> in Catalytic Combustion of Methane. *Applied Catalysis A: General* **2004**, *259* (1), 1–7. <https://doi.org/10.1016/j.apcata.2003.09.029>.
- (238) Persson, K.; Ersson, A.; Colussi, S.; Trovarelli, A.; Järås, S. G. Catalytic Combustion of Methane over Bimetallic Pd–Pt Catalysts: The Influence of Support Materials. *Applied Catalysis B: Environmental* **2006**, *66* (3), 175–185. <https://doi.org/10.1016/j.apcatb.2006.03.010>.

- (239) Narui, K.; Yata, H.; Furuta, K.; Nishida, A.; Kohtoku, Y.; Matsuzaki, T. Effects of Addition of Pt to PdO/Al<sub>2</sub>O<sub>3</sub> Catalyst on Catalytic Activity for Methane Combustion and TEM Observations of Supported Particles. *Applied Catalysis A: General* **1999**, *179* (1), 165–173. [https://doi.org/10.1016/S0926-860X\(98\)00306-8](https://doi.org/10.1016/S0926-860X(98)00306-8).
- (240) Nassiri, H.; Hayes, R. E.; Semagina, N. Stability of Pd-Pt Catalysts in Low-Temperature Wet Methane Combustion: Metal Ratio and Particle Reconstruction. *Chemical Engineering Science* **2018**, *186*, 44–51. <https://doi.org/10.1016/j.ces.2018.04.028>.
- (241) Coq, B.; Figueras, F. Bimetallic Palladium Catalysts: Influence of the Co-Metal on the Catalyst Performance. *Journal of Molecular Catalysis A: Chemical* **2001**, *173* (1), 117–134. [https://doi.org/10.1016/S1381-1169\(01\)00148-0](https://doi.org/10.1016/S1381-1169(01)00148-0).
- (242) Persson, K.; Ersson, A.; Jansson, K.; Iverlund, N.; Järås, S. Influence of Co-Metals on Bimetallic Palladium Catalysts for Methane Combustion. *Journal of Catalysis* **2005**, *231* (1), 139–150. <https://doi.org/10.1016/j.jcat.2005.01.001>.
- (243) Huang, X.; Li, Y.; Li, Y.; Zhou, H.; Duan, X.; Huang, Y. Synthesis of PtPd Bimetal Nanocrystals with Controllable Shape, Composition, and Their Tunable Catalytic Properties. *Nano Lett.* **2012**, *12* (8), 4265–4270. <https://doi.org/10.1021/nl301931m>.
- (244) Stöber, W.; Fink, A.; Bohn, E. Controlled Growth of Monodisperse Silica Spheres in the Micron Size Range. *Journal of colloid and interface science* **1968**, *26* (1), 62–69.
- (245) Nann, T.; Mulvaney, P. Single Quantum Dots in Spherical Silica Particles. *Angew Chem Int Ed Engl* **2004**, *43* (40), 5393–5396. <https://doi.org/10.1002/anie.200460752>.
- (246) Bedilo, A. F.; Klabunde, K. J. Synthesis of High Surface Area Zirconia Aerogels Using High Temperature Supercritical Drying. *Nanostructured Materials* **1997**, *8* (2), 119–135. [https://doi.org/10.1016/S0965-9773\(97\)00011-1](https://doi.org/10.1016/S0965-9773(97)00011-1).
- (247) Yoldas, B. E. Zirconium Oxides Formed by Hydrolytic Condensation of Alkoxides and Parameters That Affect Their Morphology. *J Mater Sci* **1986**, *21* (3), 1080–1086. <https://doi.org/10.1007/BF01117398>.

- (248) Stöcker, C.; Schneider, M.; Baiker, A. Zirconia Aerogels and Xerogels: Influence of Solvent and Acid on Structural Properties. *J Porous Mater* **1995**, *2* (2), 171–183. <https://doi.org/10.1007/BF00489726>.
- (249) Mahara, Y.; Ohyama, J.; Tojo, T.; Murata, K.; Ishikawa, H.; Satsuma, A. Enhanced Activity for Methane Combustion over a Pd/Co/Al<sub>2</sub>O<sub>3</sub> Catalyst Prepared by a Galvanic Deposition Method. *Catal. Sci. Technol.* **2016**, *6* (13), 4773–4776. <https://doi.org/10.1039/C6CY00650G>.
- (250) Duan, H.; You, R.; Xu, S.; Li, Z.; Qian, K.; Cao, T.; Huang, W.; Bao, X. Pentacoordinated Al<sup>3+</sup>-Stabilized Active Pd Structures on Al<sub>2</sub>O<sub>3</sub>-Coated Palladium Catalysts for Methane Combustion. *Angewandte Chemie International Edition* **2019**, *58* (35), 12043–12048. <https://doi.org/10.1002/anie.201904883>.
- (251) Torkashvand, B.; Gremminger, A.; Valchera, S.; Casapu, M.; Grunwaldt, J.-D.; Deutschmann, O. *The Impact of Pre-Turbine Catalyst Placement on Methane Oxidation in Lean-Burn Gas Engines: An Experimental and Numerical Study*; SAE Technical Paper 2017-01–1019; SAE Technical Paper: Warrendale, PA, 2017. <https://doi.org/10.4271/2017-01-1019>.
- (252) Zhang, Y.; Glarborg, P.; Johansen, K.; Andersson, M. P.; Torp, T. K.; Jensen, A. D.; Christensen, J. M. A Rhodium-Based Methane Oxidation Catalyst with High Tolerance to H<sub>2</sub>O and SO<sub>2</sub>. *ACS Catal.* **2020**, *10* (3), 1821–1827. <https://doi.org/10.1021/acscatal.9b04464>.
- (253) Thürmer, K.; Williams, E. D.; Reutt-Robey, J. E. Dewetting Dynamics of Ultrathin Silver Films on Si(111). *Phys. Rev. B* **2003**, *68* (15), 155423. <https://doi.org/10.1103/PhysRevB.68.155423>.
- (254) Kwon, S.-H.; Han, D.-H.; Choe, H. J.; Lee, J.-J. Synthesis of Copper Nanoparticles by Solid-State Plasma-Induced Dewetting. *Nanotechnology* **2011**, *22* (24), 245608. <https://doi.org/10.1088/0957-4484/22/24/245608>.
- (255) Ikeda, H.; Iwai, M.; Nakajima, D.; Kikuchi, T.; Natsui, S.; Sakaguchi, N.; Suzuki, R. O. Nanostructural Characterization of Ordered Gold Particle Arrays Fabricated via Aluminum Anodizing, Sputter Coating, and Dewetting. *Applied Surface Science* **2019**, *465*, 747–753. <https://doi.org/10.1016/j.apsusc.2018.09.229>.

- (256) Knight, M. W.; King, N. S.; Liu, L.; Everitt, H. O.; Nordlander, P.; Halas, N. J. Aluminum for Plasmonics. *ACS Nano* **2014**, *8* (1), 834–840. <https://doi.org/10.1021/nn405495q>.
- (257) Olson, J.; Manjavacas, A.; Liu, L.; Chang, W.-S.; Foerster, B.; King, N. S.; Knight, M. W.; Nordlander, P.; Halas, N. J.; Link, S. Vivid, Full-Color Aluminum Plasmonic Pixels. *PNAS* **2014**, *111* (40), 14348–14353. <https://doi.org/10.1073/pnas.1415970111>.
- (258) McClain, M. J.; Schlather, A. E.; Ringe, E.; King, N. S.; Liu, L.; Manjavacas, A.; Knight, M. W.; Kumar, I.; Whitmire, K. H.; Everitt, H. O.; Nordlander, P.; Halas, N. J. Aluminum Nanocrystals. *Nano Lett.* **2015**, *15* (4), 2751–2755. <https://doi.org/10.1021/acs.nanolett.5b00614>.
- (259) Kang, M.; Ahn, M.-S.; Lee, Y.; Jeong, K.-H. Bioplasmonic Alloyed Nanoislands Using Dewetting of Bilayer Thin Films. *ACS Appl. Mater. Interfaces* **2017**, *9* (42), 37154–37159. <https://doi.org/10.1021/acsami.7b10715>.
- (260) Arnob, M. M. P.; Zhao, F.; Li, J.; Shih, W.-C. EBL-Based Fabrication and Different Modeling Approaches for Nanoporous Gold Nanodisks. *ACS Photonics* **2017**, *4* (8), 1870–1878. <https://doi.org/10.1021/acsphotonics.7b00239>.
- (261) Tabor, C.; Van Haute, D.; El-Sayed, M. A. Effect of Orientation on Plasmonic Coupling between Gold Nanorods. *ACS Nano* **2009**, *3* (11), 3670–3678. <https://doi.org/10.1021/nn900779f>.
- (262) Zhan, P.; Wen, T.; Wang, Z.; He, Y.; Shi, J.; Wang, T.; Liu, X.; Lu, G.; Ding, B. DNA Origami Directed Assembly of Gold Bowtie Nanoantennas for Single-Molecule Surface-Enhanced Raman Scattering. *Angewandte Chemie International Edition* **2018**, *57* (11), 2846–2850. <https://doi.org/10.1002/anie.201712749>.
- (263) Fayyaz, S.; Tabatabaei, M.; Hou, R.; Lagugné-Labarthe, F. Surface-Enhanced Fluorescence: Mapping Individual Hot Spots in Silica-Protected 2D Gold Nanotriangle Arrays. *J. Phys. Chem. C* **2012**, *116* (21), 11665–11670. <https://doi.org/10.1021/jp302191z>.

- (264) Byun, I.; Coleman, A. W.; Kim, B. SAM Meets MEMS: Reliable Fabrication of Stable Au-Patterns Embedded in PDMS Using Dry Peel-off Process. *Microsyst Technol* **2014**, *20* (10), 1783–1789. <https://doi.org/10.1007/s00542-013-1923-8>.
- (265) Du, K.; Wathuthanthri, I.; Liu, Y.; Xu, W.; Choi, C.-H. Wafer-Scale Pattern Transfer of Metal Nanostructures on Polydimethylsiloxane (PDMS) Substrates via Holographic Nanopatterns. *ACS Appl. Mater. Interfaces* **2012**, *4* (10), 5505–5514. <https://doi.org/10.1021/am301423s>.
- (266) Ouellet, E.; Yang, C. W. T.; Lin, T.; Yang, L. L.; Lagally, E. T. Novel Carboxyl-Amine Bonding Methods for Poly(Dimethylsiloxane)-Based Devices. *Langmuir* **2010**, *26* (14), 11609–11614. <https://doi.org/10.1021/la1012582>.
- (267) Lee, K. J.; Fossier, K. A.; Nuzzo, R. G. Fabrication of Stable Metallic Patterns Embedded in Poly(Dimethylsiloxane) and Model Applications in Non-Planar Electronic and Lab-on-a-Chip Device Patterning. *Advanced Functional Materials* **2005**, *15* (4), 557–566. <https://doi.org/10.1002/adfm.200400189>.
- (268) Krier, J. M.; Michalak, W. D.; Cai, X.; Carl, L.; Komvopoulos, K.; Somorjai, G. A. Sum Frequency Generation Vibrational Spectroscopy of 1,3-Butadiene Hydrogenation on 4 Nm Pt@SiO<sub>2</sub>, Pd@SiO<sub>2</sub>, and Rh@SiO<sub>2</sub> Core–Shell Catalysts. *Nano Lett.* **2015**, *15* (1), 39–44. <https://doi.org/10.1021/nl502566b>.
- (269) Seo, M.; Kim, S.; Lee, D.-W.; Jeong, H. E.; Lee, K.-Y. Core–Shell Structured, Nano-Pd-Embedded SiO<sub>2</sub>–Al<sub>2</sub>O<sub>3</sub> Catalyst (Pd@SiO<sub>2</sub>–Al<sub>2</sub>O<sub>3</sub>) for Direct Hydrogen Peroxide Synthesis from Hydrogen and Oxygen. *Applied Catalysis A: General* **2016**, *511*, 87–94. <https://doi.org/10.1016/j.apcata.2015.11.040>.
- (270) Bao, Z.; Weatherspoon, M. R.; Shian, S.; Cai, Y.; Graham, P. D.; Allan, S. M.; Ahmad, G.; Dickerson, M. B.; Church, B. C.; Kang, Z.; Abernathy Iii, H. W.; Summers, C. J.; Liu, M.; Sandhage, K. H. Chemical Reduction of Three-Dimensional Silica Micro-Assemblies into Microporous Silicon Replicas. *Nature* **2007**, *446* (7132), 172–175. <https://doi.org/10.1038/nature05570>.
- (271) Lai, Y.; Thompson, J. R.; Dasog, M. Metallothermic Reduction of Silica Nanoparticles to Porous Silicon for Drug Delivery Using New and Existing Reductants. *Chemistry – A European Journal* **2018**, *24* (31), 7913–7920. <https://doi.org/10.1002/chem.201705818>.

(272) Martell, S. A.; Lai, Y.; Traver, E.; MacInnis, J.; Richards, D. D.; MacQuarrie, S.; Dasog, M. High Surface Area Mesoporous Silicon Nanoparticles Prepared via Two-Step Magnesiothermic Reduction for Stoichiometric CO<sub>2</sub> to CH<sub>3</sub>OH Conversion. *ACS Appl. Nano Mater.* **2019**, *2* (9), 5713–5719. <https://doi.org/10.1021/acsanm.9b01207>.